



TECHNISCHE
UNIVERSITÄT
WIEN



DIPLOMARBEIT

Microwave assisted synthesis of MOCHAs and their application in (photo)electrocatalytic syngas production

Ausgeführt am
Institut für Materialchemie
Forschungsbereich Molekulare Materialchemie
der Technischen Universität Wien

Unter der Anleitung von
Univ. Prof. Mag.rer.nat Dr.rer.nat. Dominik Eder
Univ. Ass. Dr.rer.nat Doğukan Hazar Apaydin

durch
Hannah Rabl, BSc.

11707311

Wien, im September 2022

Unterschrift

STATUTORY DECLARATION

I hereby declare that the thesis submitted is my own unaided work, that I have not used other than the sources indicated, and that all direct and indirect sources are acknowledged as references. This printed thesis is identical with the electronic version submitted.

.....

Signature

.....

Place, Date

2 Table of contents

2	Table of contents.....	3
3	Abstract	5
4	Kurzfassung	6
5	Introduction.....	7
6	Theoretical Background	9
6.1	Syngas.....	9
6.1.1	Syngas applications	9
6.1.2	Industrial Syngas Production.....	10
6.1.3	Alternative ways to get Syngas	10
6.2	Electrochemical CO ₂ reduction reaction (CO ₂ RR).....	13
6.2.1	Noble metal catalysts	15
6.2.2	Metal oxides	16
6.2.3	Metal chalcogenides.....	17
6.3	MOCHAs	18
6.3.1	Synthesis routes of MOCHAs.....	18
6.3.2	Properties of MOCHAs	21
7	Motivation and Aims	23
8	Experimental	24
8.1	List of used chemicals and instruments	24
8.2	MOCHA Synthesis.....	26
8.2.1	Biphasic synthesis of MOCHAs	27
8.2.2	Tarnishing synthesis of MOCHAs.....	27
8.2.3	Microwave synthesis of MOCHAs	27
8.2.4	Hydrothermal synthesis of MOCHAs.....	28
8.3	Electrode preparation	28
8.3.1	Ink preparation.....	28
8.3.2	Deposition methods	28
8.3.3	Deposition of silver nanoparticles.....	29
8.4	Characterization methods of electrodes and MOCHAs	29
8.4.1	Attenuated total reflection Fourier transformed infrared spectroscopy (ATR-FTIR)	29
8.4.2	Diffuse reflectance spectroscopy (DRS)	29
8.4.3	Electrochemical methods.....	29
8.4.3.1	Linear sweep voltammetry (LSV).....	30
8.4.3.2	Photocurrent measurement.....	30
8.4.4	Scanning electron microscopy/Energy dispersive X-ray spectrometry (SEM/EDX) ..	31

8.4.5	Total X-ray fluorescence spectroscopy (TXRF)	31
8.4.6	X-ray photoelectron spectroscopy (XPS).....	31
8.4.7	X-ray diffraction (XRD).....	31
8.5	Catalytic testing of MOCHAs	31
8.5.1	(Photo) electrochemical CO ₂ RR.....	32
8.5.2	Gas chromatography (GC)	32
8.5.3	Faraday Efficiency (FE) and Rate calculation	33
8.6	Stability testing on MOCHAs	33
9	Results and Discussion	34
9.1	Synthesis and Characterization of electrodes	34
9.1.1	Synthesis methods	34
9.1.2	Electrode preparation	35
9.1.3	Silver nanoparticle deposition.....	36
9.1.4	Characterization of electrodes	37
9.2	(Photo)electrochemical Syngas production	42
9.2.1	Potential and electrode dependence.....	42
9.2.2	Effect of light	45
9.2.3	Effect of silver nanoparticles.....	47
9.3	Stability of MOCHAs	48
9.3.1	Organic solvent, pH and temperature.....	48
9.3.2	Illumination	49
9.3.3	After electrolysis.....	51
9.4	New MOCHAs	52
10	Conclusion and Outlook	56
11	Acknowledgement.....	58
12	References.....	59
13	Appendix.....	68
13.1	List of Abbreviations.....	68
13.2	List of Figures.....	69
13.3	List of Tables.....	71
13.4	List of all tested microwave synthesis conditions	72
13.5	pH, temperature and illumination stability, TXRF and EDX spectra.....	73
13.6	List of all tested microwave synthesis conditions	77

3 Abstract

Syngas (the mixture of H₂ and CO) is nowadays still mainly produced from fossil fuels. The use of fossil fuels, however, is problematic for several reasons. On one hand fossil fuels cannot be regarded as renewable energy sources and are therefore not endlessly available. Another difficulty related to fossil fuels is their abundance on earth, which causes a high dependence from other countries. This leads to socioeconomic pressures as it can be observed recently in Europe due to the dependence on Russian gas. Combustion of fossil fuels (oil, gas and coal) does also result in higher carbon dioxide (CO₂) emissions. CO₂ being a greenhouse gas does accelerate global warming and thus exhibits a high impact on our environment and life on earth. A possible alternative to fossil fuels for syngas production is the (photo)electrochemical synthesis of syngas from carbon dioxide and water. This would not only decrease the dependence on coal and gas but also lead to a reduction of carbon dioxide levels in the atmosphere. One of the biggest challenges of electrochemical CO₂ reduction is the search for suitable catalysts. Metal organic chalcogenolate assemblies (MOCHAs) are a highly interesting class of semiconducting inorganic–organic hybrid coordination polymers, which show outstanding optoelectronic properties. In this work an alternative synthesis route for MOCHA production is presented. It involves an “in-bulk” synthesis, enabling higher yields and facile product isolation. Different deposition methods of MOCHA on carbon paper are discussed and compared to each other. The so obtained electrodes are characterized by ATR-FTIR SEM / EDX, DRS, TXRF, XPS and XRD. The two MOCHA types “mithrene” and “thiorene” are investigated on their potential to act as (photo)electrocatalysts for syngas production. The influence of silver nanoparticles onto MOCHAs on their CO₂ reduction capability is addressed. The structural stability of [AgSePh]_n upon various conditions is examined. New, iron-, copper-, and nickel-containing MOCHA materials are presented and analysed by means of imaging, spectroscopic and diffractive methods.

4 Kurzfassung

Syngas ($H_2:CO$) wird heutzutage nach wie vor zum größten Teil aus fossilen Brennstoffen gewonnen. Die Verwendung von fossilen Brennstoffen ist jedoch aus mehreren Gründen problematisch. Zum einen gelten fossile Brennstoffe nicht als erneuerbar und sind somit nicht unbegrenzt verfügbar. Die Verfügbarkeit ist eng verbunden mit den Vorkommnissen der fossilen Brennstoffe, die eine große Abhängigkeit von anderen Ländern darstellt. Dies hat weitreichende sozioökonomische Auswirkungen, wie anhand der Abhängigkeit Europas von Russischem Erdgas im Moment deutlich wird. Die Verbrennung kohlenstoffhaltiger Verbindungen (Gas, Öl, Kohle) führt ebenfalls zu erhöhten CO_2 Emissionen. Einem Treibhausgas, das nachweislich zur globalen Erderwärmung beiträgt, welche weitreichende und langwierige Folgen auf unsere Umwelt und das Leben auf der Erde haben wird. Eine mögliche Alternative zu fossilen Brennstoffen für die Syngas Erstellung ist die (photo)elektrochemische Gewinnung von Syngas aus Kohlenstoffdioxid und Wasser. Dies würde nicht nur die Abhängigkeit von Gas und Kohle minimieren, sondern auch zu einer Reduktion des CO_2 Gehalts in der Atmosphäre führen. Eine der größten Herausforderungen der elektrochemischen CO_2 Reduktion, ist jedoch die Suche nach einem geeigneten Katalysator. Metal organic chalcogenolate assemblies (MOCHAs) sind eine hochinteressante Klasse an hybriden, halbleitenden Koordinationspolymeren, welche herausragende, optoelektronische Eigenschaften besitzen. In dieser Arbeit wird eine alternative Synthesemethode für MOCHA Herstellung präsentiert, welche eine In-Bulk Synthese ermöglicht und somit höhere Ausbeuten erlaubt. Außerdem werden verschiedene Abscheidungsmethoden von MOCHA auf Carbon Paper miteinander verglichen und die so erhaltenen Elektroden charakterisiert. Die zwei MOCHAs „mithrene“ und „thiorene“ werden auf ihr Potenzial (photo)elektrochemisch Syngas zu produzieren untersucht. Die Auswirkungen von photochemischer Silber-Nanopartikel Abscheidung auf die Performance der MOCHA / CP Elektroden bezüglich photoelektrochemischer CO_2 -Reduktion wurde untersucht. Die strukturelle Stabilität von $[AgSePh]_\infty$ unter verschiedensten Bedingungen wird betrachtet. Im Anschluss werden neue, Eisen-, Kupfer- und Nickel-enthaltende MOCHAs präsentiert und mittels verschiedenster bildgebender, spektroskopischer und beugender Methoden analysiert.

5 Introduction

Climate change and global warming are amongst the major and most serious challenges and threats to life on earth. While a certain non-anthropogenic climate change is usual and normal on earth to occur, the excessive release of greenhouse gases causes a dramatic acceleration and intensification of climate change¹. Greenhouse gases including CO₂, H₂O_{gaseous}, N₂O, O₃ and CH₄ to name only the most important ones, are naturally abundant in our atmosphere. They are crucial for making life on earth possible as they are able to absorb infrared radiation emitted by our planet earth and thus stabilize the average temperature in our atmosphere at 17 °C². Industrialization and globalization, especially the combustion of fossil fuels caused an anthropogenic increase of the greenhouse gas carbon dioxide³⁻⁵. Cut down of the rainforest, the lung of our earth and even worse burning down the rainforest does not only increase CO₂ emissions but also decreases the amount of CO₂ converted into life essential oxygen. The excess of carbon dioxide in the atmosphere causes global warming, consequently elevating the average temperature on earth². This will result in a melting of glaciers and polar ice, leading the mean sea level to rise³. The likelihood of weather extremes such as thunderstorms, flooding and droughts will increase drastically in the next centuries³. According to the IPCC annual report, even a zero net CO₂ emission could not prevent the sea level rise from happening anymore³. Droughts and flooding will cause a high number of people sliding into poverty and hunger. Diseases and loss of biodiversity are inevitable so.

Moving away from fossil fuels has been the goal since many years. Renewable energy sources such as water, wind, sunlight, geothermal and tide to name only a few, were often not enforced due to cheap availability of natural gas, oil and coal. The EU enforced its member states to stop the burning of coal as it does not only cause the release of carbon dioxide but also health threatening PM₁₀ and PM_{2.5}⁶. The Russian attack on Ukraine in February 2022 and the following sanctions by the EU towards Russia caused a limited gas supply from Russia towards many countries in the European Union⁷. Beside the fear of having too little gas for the next winter also industries in Austria and other European countries highly depend on gas. The prices for gas, oil and fuel have exploded ever since⁸. The dependence and utilization of gas has not only become an environmental issue but also a socioeconomic concern. Alternatives to natural gas are searched. Especially industries might be able to adapt their processes, in order to work with other feedstocks than gas and oil.

Besides the simple things anyone of us can contribute to the reduction of CO₂, the “big fish” so to say, it is essential to establish a method for reducing carbon dioxide from atmosphere and turning it into valuable chemicals. These chemicals could serve as a feedstock for adapted industrial processes. Therefore, carbon dioxide has to be captured first. The two processes CCS (carbon capture and storage) and CCU (carbon capture and utilization) are of great research interest^{9,10}. Captured CO₂ can be converted electrochemically into carbon monoxide and hydrogen. The mixture is referred to as syngas and is used for the production of many essential chemicals including methanol and ammonia. Both play significant roles in pharmaceutical and food industry. As syngas is mainly received from natural gas up to this date, the reduction of CO₂ to syngas would be beneficial in two ways. Reduction of the greenhouse gas CO₂ could be achieved, leading to a deceleration of climate change and

global warming and the dependence on natural gas for the production of syngas would be lifted^{11,12}.

6 Theoretical Background

In the following chapter a brief theoretical background on important topics of this thesis should be given. In the first section an overview of the needs for syngas, the industrial processes to get syngas and alternative synthesis routes are presented. The following section draws its focus to the electrochemical carbon dioxide reduction. The challenges and limitations of this process are discussed and a summary on the best available metal, metal oxide and metal chalcogenide catalysts is given. The last section should be an introduction to the materials class “MOCHA”. Already published and known properties and synthesis processes for these materials are summarized.

6.1 Syngas

Commonly referred to as “syngas” also called “synthesis gas” a gaseous mixture of either nitrogen and hydrogen or carbon monoxide and hydrogen is described¹³. If not stated otherwise, in this work syngas refers to the mixture of H₂ and CO. The H₂:CO ratio varies with the chosen synthesis route and is dependent on the application of interest. While steam reforming results in a high syngas ratio (H₂:CO approx.~3) and is mainly used for ammonia production, the dry reforming of methane process results in a low syngas ratio (H₂:CO approx.~1) which is useful for the production of oxygenates^{11,14}.

6.1.1 Syngas applications

The production of syngas is not only essential when a mixture of CO and H₂ is needed but also when either one of these compounds is of interest. In this case, the desired compound (either H₂ or CO) will be purified from the other compound and additional contaminations involving CO₂ or H₂S.

Hydrogen is needed and used for various types of applications. Its properties including the strong H–H bond with an energy of 436 kJ mol⁻¹ and the high density of H₂ at low temperatures make it a promising material for power generation and fuel applications^{13,15}. A merit is also the tripled energy content of hydrogen compared to gasoline on a mass basis¹⁶. Hydrogen can even be regarded as the fuel with the highest energy content per unit mass (142 kJ g⁻¹)¹⁷. The fact that hydrogen is a clean energy carrier with only water as a combustion product enforce industries to focus and invest in hydrogen technologies¹⁵. One of the most important applications of hydrogen is its use in the Haber Bosch process for the production of ammonia¹³. Ammonia is used to produce fertilizers, increasing grain, vegetable and fruit harvest and thus securing the world’s food supply¹⁸. Other applications involve hydrogen as a reducing agent, for the saturation of double bonds and the desulfurization of hydrocarbons producing H₂S¹³.

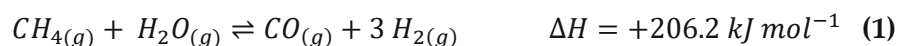
Syngas (H₂:CO) is an important feedstock for numerous reactions. It is mainly utilized to produce chemicals including methanol and dimethyl ether. Methanol is abundantly used in chemical industry as a solvent and a C1 building block, being further converted into synthetic hydrocarbons, polymers and single-cell proteins^{17,19}. Thanks to the Fischer-Tropsch process, hydrocarbons from syngas are potential candidates for synfuels or synthetic petroleum²⁰⁻²². Synfuels have the merit of “being renewable”. Fossil fuels, including gas, oil, gasoline and diesel are limited and their high carbon content leads to high

CO₂ emissions upon combustion. Syngas with a high H₂:CO ratio will have decreased CO₂ emissions and provides a higher energy content compared to common fossil fuels¹⁶.

6.1.2 Industrial Syngas Production

The three main routes for industrial syngas production are: steam reforming, partial oxidation and thermal decomposition^{13,23}. Depending on the available feedstock and its aggregate state one of these approaches is chosen.

Steam reforming involves natural hydrocarbons in gaseous state, mostly methane which is converted into syngas by addition of steam and heat.



This process is highly endothermic, requiring high pressures and temperatures and the use of catalysts^{11,13}. At these conditions the likelihood for unwanted coke formation is rather high^{11,24-26}. Noble metal catalysts would show a high activity and stability against this coke formation, but due to their high costs, nickel based catalysts are often used as an alternative^{11,27,28}. Steam reforming is often followed by the exothermic water gas shift reaction, converting the carbon monoxide into carbon dioxide¹³.

Partial oxidation to syngas is usually performed by flowing oxygen over a bed filled with coal.



A certain bed height and limited availability of oxygen force the Boudouard equilibrium to work, converting the formed carbon dioxide into CO¹³.



Thermal decomposition can be done on liquid or gaseous hydrocarbons e.g. methanol at elevated temperatures¹⁷.



All three of the presented production routes are based on highly endothermic processes and depend on fossil fuels as feedstock for syngas production. High energy demand and utilization of expensive metal catalysts are necessary for these processes to occur. As already stated in the introduction section of this work, the dependence and use of fossil fuels does not only cause environmental problems but leads also to socioeconomic difficulties. Further we must be aware, that fossil fuels are limited and thus renewable, less harmful alternatives for syngas production are of great need.

6.1.3 Alternative ways to get Syngas

This chapter introduces four alternative processes to the previously presented syntheses routes. Those four approaches are: the use of biomass, thermochemical cycles, photocatalytic syngas production and electrolysis of water and carbon dioxide^{29,30}.

Syngas production from **biomass** has a big merit. Biomass, compared to fossil fuels, is sustainable and renewable. Its availability and accessibility are facilitated and thus

inexpensive. Biomass was mainly used as an energy / heat source^{31,32}. Combustion of biomass comes along with emission of NO_x, polycyclic aromatic hydrocarbons (PAHs), CO, soot and particulate matter all being pollutants and potential health and environmental threats. Biomass gasification to syngas and consequent methanation of syngas would be a valuable technique to reuse biomass waste and convert it into useful chemicals, simultaneously reducing the dependence on natural gas³¹. Besides the high energy conversion efficiency for methane, the already available infrastructure for methane would enable a smooth link / passage from fossil fuels to synthetic energy^{31,33}. The success of biomass gasification depends on various parameters including the biomass type, reactor and catalyst choice, process temperature and pressure, bed-type and many more³¹. Various large scale industrial biomass gasification and syngas methanation plants already exist around the world already including the first power to gas plant at Volkswagen Audi Company in Germany³¹.

Thermochemical cycles are based on the principle to achieve thermally induced splitting of water and carbon dioxide. Therefore, nuclear reactor heat or concentrated solar power is used to achieve high temperatures (>2500 K) in order to dissociate reactants and separate hydrogen and oxygen. Two step cycles opposite to direct thermolysis function at lower temperatures and use metal oxide redox pair-based cycles. The two steps involve endothermic thermal dissociation of the metal oxide to a metal or lower valence oxide followed by exothermic oxidation of the metal / metal oxide with the help of water / carbon dioxide. The products hydrogen and CO can then be combined to syngas and the metal oxide has to be regenerated. The two step thermochemical cycles are divided into volatile and non-volatile cycles referring to the present state of the metal containing species^{29,34-37}. A merit of this technique is their favourable thermodynamics but the solar-to-fuel energy conversion is still rather low (up to 10 %). So far La-Sr-Mn perovskites have been proven to be suitable materials in the two-step solar thermochemical reaction but still research on elevating the solar-to-fuel efficiencies has to be made in order to enable a large scale application of this syngas production technique^{29,38}.

The breakthrough in **photocatalytic water splitting** was achieved by Fujishima and Honda in 1972^{29,39}. Photocatalytic syngas production requires the presence of photocatalysts. Often semiconducting materials are used as such. Semiconductors are materials in which a band gap between the highest occupied band (valence band, VB) and the lowest unoccupied band (conduction band, CB) exists. In order to exhibit semiconducting properties, this band should be in the range of 1.5 eV-4 eV. When light hits the semiconductor surface, electrons from its valence band are elevated to the conduction band. This process leads to the production of electron / hole pairs, also referred to as excitons (e⁻/h⁺ pair). Electrons in the conduction band are now able to move and thus can provide the energy necessary for the conversion of water to hydrogen and oxygen and carbon dioxide to methane or methanol. The major challenge in the field of photocatalytic CO₂ reduction is the research and development of more efficient/selective photocatalytic materials^{29,40}. Photochemical syngas production is often combined with electrolysis leading us to the last of the four alternative approaches: Electrochemical syngas production.

Different type of **electrolysis processes** are known to convert water and carbon dioxide into syngas electrochemically. These processes include alkaline electrolysis with liquid electrolyte, proton exchange membrane (PEM) electrolysis and the use of solid oxide electrolysis cells (SOEC).

Alkaline electrolysis is based on bringing an aqueous alkaline electrolyte (often 20-40 %KOH) on the cathodic side which is separated via a diaphragm from the anodic compartment. It is usually conducted at medium temperatures of 80 °C. Water is then reduced at the cathode to hydrogen and hydroxide ions, latter can migrate through the diaphragm to the anode where they are oxidized to oxygen²⁹ and water. Alkaline electrolysis cells are having the merit of cheap, easy available Raney nickel electrodes and are already commercialized^{29,41-43}.

In **PEM electrolysis** the working principle / mechanism is a little different from alkaline electrolysis. Water is fed to the anode first, where it is oxidized to oxygen and protons. Protons are then able to diffuse through the membrane and get reduced at the cathode to the desired hydrogen. PEM electrolysis compared to alkaline electrolysis has the challenge of requiring platinum-group metals as catalysts. On the other hand, alkaline electrolysis current densities are reported to be lower by a factor of five compared to PEM electrolysis. Another advantage of PEM electrolysis is their better gas quality²⁹. All the presented electrochemical methods so far, were focussed on hydrogen production.

In **solid oxide electrolysis cells** (SOECs) water and / or carbon dioxide is passed through the fuel electrode and an oxygen / air stream is running through the oxygen electrode channel. This leads not only to a conversion of water to hydrogen and carbon dioxide to carbon monoxide but also enables a storing of energy. At the cathode, the following reactions occur:



At the oxygen electrode the oxygen ions (O^{2-}) are oxidized to oxygen as follows:



One of the most common electrode materials for SOECs is YSZ (yttrium stabilized zirconia). It enables O_2 ion conduction at elevated temperatures. Their high working / operating temperature leads to a reduced electricity consumption which is a huge merit of these cells^{29,44}. On a large scale application SOECs compared to other presented methods would offer the lowest capital and operating costs^{29,45}.

Low temperature electrolysis cells with noble metal catalysts and a buffered layer of electrolyte enable syngas production as well, however long-term research is needed still to make this method market proof. In the following section a closer look is taken on low temperature electrochemical carbon dioxide reduction. Its challenges, potential catalysts and best performances are presented.

6.2 Electrochemical CO₂ reduction reaction (CO₂RR)

Carbon dioxide (CO₂) is a linear, chemically stable molecule. The energy required for the dissociation of the C=O double bond is 750 kJ mol⁻¹ ⁴⁶. Direct one electron CO₂ reduction could be done via the formation of a CO₂^{•-} anion radical. This step however is highly unfavourable, requiring high energy inputs. Proton assisted multiple-electron transfer is a more suitable way to lead to carbon dioxide reduction. Sixteen different products for CO₂ reduction have been reported involving up to eighteen electrons. A few possible reactions and their thermodynamic formal potentials @ pH 7 *vs.* SHE (standard hydrogen electrode) are shown below⁴⁶.

Table 1. Possible reaction products of electrochemical CO₂RR and HER (last line) and their corresponding formal redox potential *vs.* SHE.

Reaction equation	Formal redox potential <i>vs.</i> SHE E ⁰ (V)
CO ₂ + 2H ⁺ + 2e ⁻ ⇌ HCOOH	-0.610
CO ₂ + 2H ⁺ + 2e ⁻ ⇌ CO + H ₂ O	-0.530
2CO ₂ + 2H ⁺ + 2e ⁻ ⇌ H ₂ C ₂ O ₄	-0.913
CO ₂ + 6H ⁺ + 6e ⁻ ⇌ CH ₃ OH + H ₂ O	-0.380
CO ₂ + 8H ⁺ + 8e ⁻ ⇌ CH ₄ + 2H ₂ O	-0.240
2CO ₂ + 12H ⁺ + 12e ⁻ ⇌ C ₂ H ₅ OH + 3H ₂ O	-0.329
2H ⁺ + 2e ⁻ ⇌ H ₂	-0.420

The last equation in **Table 1** shows the competing process to CO₂ reduction which is unavoidable in aqueous electrolytes using a proton assisted reduction approach: proton reduction to hydrogen at the cathode, often also called hydrogen evolution reaction (HER). Consequently, in aqueous electrolytes CO₂ reduction products and hydrogen appear simultaneously. Taking a closer look at the formal redox potentials above reveal that the formation of hydrocarbons and alcohols should be thermodynamically favoured over CO or formic acid formation according to the equation:

$$\Delta G = -zFE^0 \quad (8)$$

with

ΔG...Gibbs free energy

z....number of transferred electrons

F....Faraday constant (96485 C mol⁻¹)

E⁰....standard redox potential

Practical measurements however show that the maximum Faraday efficiency for C₂ products is reported to be 60 %, for C₃ products only FE's up to 30 % could be reached⁴⁶⁻⁴⁹. It must be taken into account, that CO₂ reduction is not only dependent on thermodynamics but also kinetics play an important role. Available proton concentration, catalytic side preference and kinetically easier hydrogenation than C–C formation cause a favoured C₁ product formation including CO, methanol and formic acid despite their thermodynamic unfavourable position⁴⁶.

The chosen electrolyte is playing a major role in product selectivity and catalyst activity. Possible electrolytes for CO₂ reduction are aqueous and organic electrolytes but also ionic liquids. As both organic electrolytes and ionic liquids inhibit hydrogen formation, they are not suitable for syngas production. Aqueous electrolytes in combination with the right catalyst lead to a well-defined hydrogen to carbon monoxide ratio. It was shown that large cationic species on a silver electrode led to mainly CO formation^{46,50}. Anionic species with buffer capability on the other hand affect the pH at the electrode and influence thus product selectivity. Consequently a higher pH will suppress hydrogen formation due to lack of protons^{46,51}. The use of HCO₃⁻ is further useful in overcoming the problem of the low solubility of carbon dioxide in water providing an intrinsic carbon dioxide source.

Mechanism for CO₂ reduction vary depending on the desired product formation. At this point only a closer look is taken onto the CO formation reaction pathway.

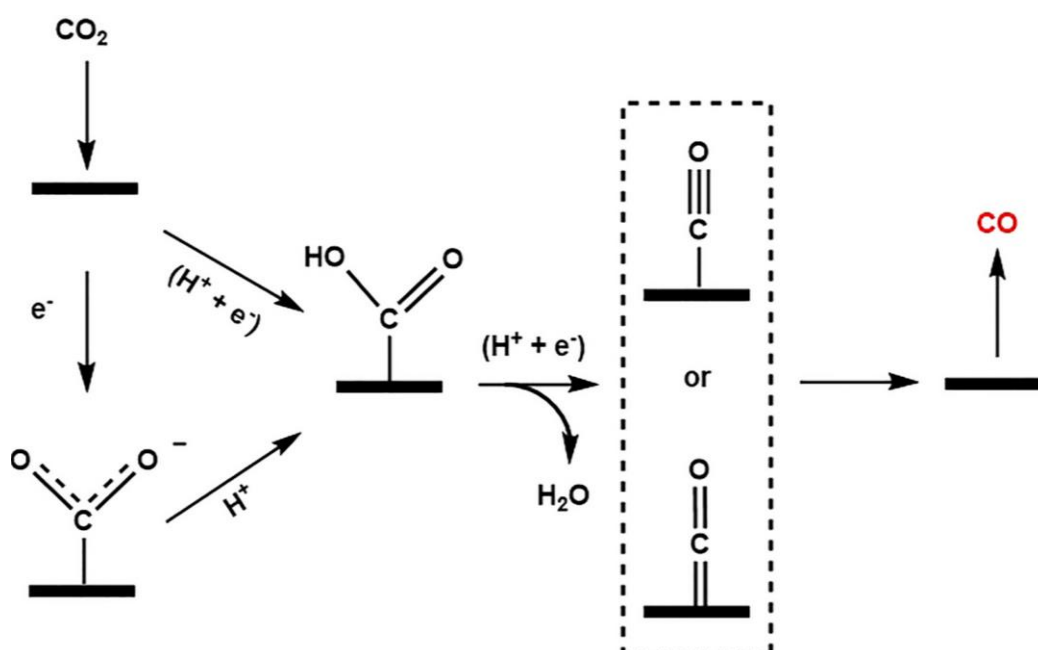


Figure 1. Reaction pathway of CO₂ reduction to carbon monoxide via coupled proton / electron *COOH formation (up) and decoupled *COOH formation (down) Reproduced with permission from^{46,52}. Copyright 2017 Elsevier Inc.

In **Figure 1** above the reaction pathway for electrochemical CO formation is demonstrated. This two-electron process involves carboxyl intermediate formation (*COOH) at first. Consequently, an H⁺/e⁻ pair attacks this *COOH intermediate leading to the formation of water and an adsorbed *CO species. The binding strength of the *CO adsorbate is weak on metal catalyst surfaces and thus CO is desorbed^{46,52,53}. Calculations revealed two rate limiting steps in the CO formation pathway. First the very weak *COOH binding, second the strong *CO binding^{46,54}. Another pathway suggests a proton-electron decoupled formation of *COOH. To do so a CO₂ radical had to be formed previous to hydrogenation.

As already mentioned, electrochemical CO₂RR requires the presence of catalysts at the cathode. Various materials have been tested and reported as potential CO₂ reduction catalysts^{12,53,55–57}. In the following section a closer look should be taken on noble metal catalysts, metal oxides and metal chalcogenide catalysts. The latter are often semiconductors. Semiconductors opposed to metals do not have a continuum of energy

states and thus high electrical mobility. They exhibit a band gap between the valence band (VB) and conduction band (CB). An intrinsic (undoped) semiconductor has equal numbers of electrons and holes in its VB but no electrons in its CB. In order to cause conducting properties an extrinsic semiconductor has to be created via doping. Thus, an excess of electrons and holes is present. The Fermi level (E_{Fermi}) is defined as the energy between valence and conduction band in an intrinsic semiconductor. The Fermi energy is moved closer to the conduction band in case of n-type semiconductors and closer to the valence band in case of p-type semiconductors. In electrochemistry the semiconductor electrode is in a constant interaction with the electrolyte. The electrolyte solution itself has a certain redox potential (E_{redox}) and electrons at the semiconductor-electrolyte interface will try to compensate the difference in E_{Fermi} and E_{redox} . While the redox potential of the electrolyte will rather stay the same due to the excess of charge carriers in the electrolyte the Fermi level will adjust to this in equilibrium. Thus a depletion zone is created in the semiconductor near the junction. Further due to the difference in the occupied energy levels between the depletion zone and the bulk, band bending occurs. This causes electrons and holes to move into different directions: to the bulk and towards the interface⁵⁸⁻⁶¹. **Figure 2** below demonstrates the explained principle of band bending when extrinsic semiconductors are in equilibrium with an electrolyte.

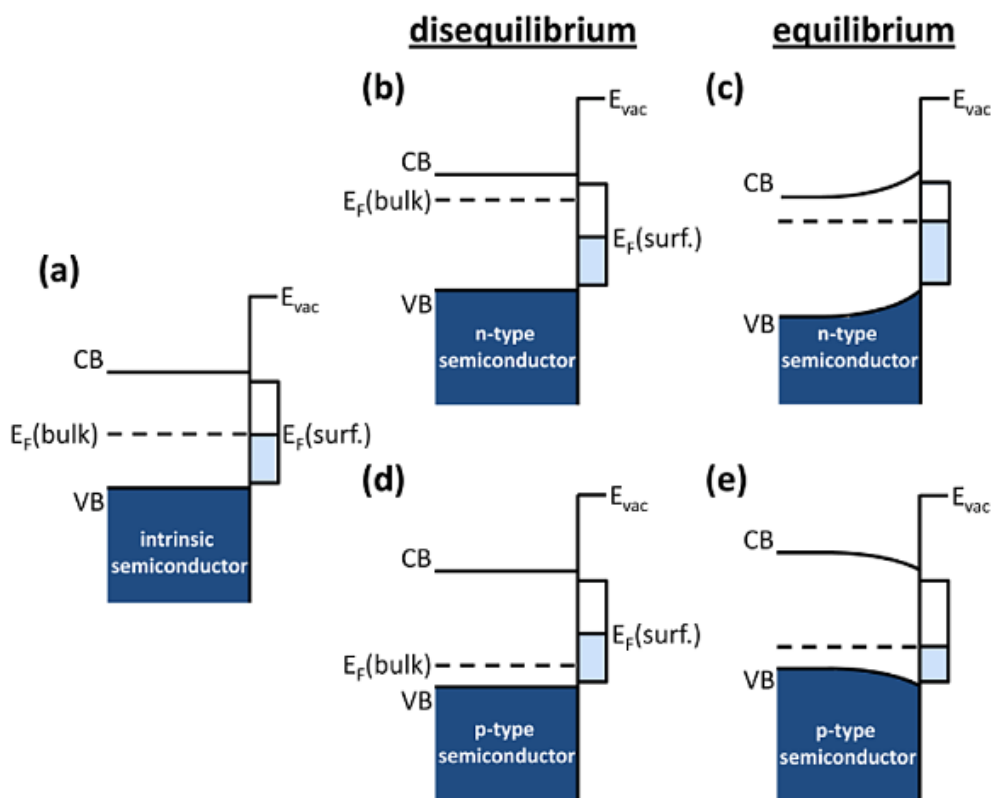


Figure 2. Schematic of energy band behaviour of an **a.** intrinsic semiconductor, **b.** n-type extrinsic semiconductor and **d.** p-type extrinsic semiconductor in disequilibrium and **c** and **e.** in equilibrium due to band bending. Reproduced with permission from⁵⁸. Copyright 2012 American Chemical Society.

6.2.1 Noble metal catalysts

Silver and gold are probably the most studied noble metals in terms of syngas production. As theoretical calculations and measurements performed 37 years ago by Hori *et al.*⁵⁷

revealed are these noble metals especially suitable for CO₂RR due to their lower binding strength towards CO. Further reduction to hydrocarbons is thus inhibited. While gold is the preferred choice as model catalyst, silver is rather suitable for applications due to its lower costs. On Au model catalysts it was shown that the H₂:CO ratio is highly dependent on nanoparticle size and grain boundaries. Gold nanoparticles of 8 nm led to a 1:9 hydrogen to carbon monoxide ratio, whereas 10 nm particles resulted in a 1:3 H₂:CO ratio. DFT calculations revealed that CO is favourably produced at the edges while hydrogen formation is favoured at corners^{12,62}. Similar to Au-NP, gold nanowire lengths could also influence the hydrogen to carbon monoxide ratio^{12,63}. Grain boundary surface area density was reported to show a linear relationship with the normalized surface area toward CO₂RR activity and selectivity^{12,64}. Silver catalysts shown a high selectivity towards CO as well. Depending on their corner to edge ratio and the dominating crystal plane the CO selectivity could be influenced. Triangular shaped silver catalysts shown a FE of 96.8 % at 0.746 *vs.* RHE whereas Ag-NP only reached a FE of 65.4 % at even higher overpotentials. Bulk silver catalysts lead to the lowest CO Faraday efficiency of 57.2 % at an overpotential of -0.946 V *vs.* RHE^{12,65}. A further noble metal palladium was believed to be not suitable for electrochemical syngas production due to the poisoning of Pd metal with CO. A study published in 2017 used *in-situ* techniques to reveal that Pd is converted to β-PdH, which showed weakened theoretical binding strengths for CO and H₂ thus accelerating syngas formation^{12,66}.

Despite their good performance, noble metals are scarcely available and expensive, making them not very promising for industrial large-scale application as catalysts in electrochemical syngas production.

6.2.2 Metal oxides

Metal oxides are not only cheaper and abundantly available compared to metal catalysts but also show a non-toxic, highly catalytic alternative towards syngas production^{12,67}. Especially their capability of forming oxygen vacancies ($v_{\text{O}}^{\bullet\bullet}$) creates possible adsorption sites for CO₂ enhancing the CO₂RR activity. Further an electron rich surface is promoted by oxygen vacancies leading to an enhanced CO₂ adsorption and activation^{67,68}. This was shown on ZnO nanosheets, in which high number of $v_{\text{O}}^{\bullet\bullet}$ caused an increasing CO selectivity whereas poor $v_{\text{O}}^{\bullet\bullet}$ number resulted in a low carbon monoxide to hydrogen ratio^{12,69}. It was shown that metal oxides such as In₂O₃ or SnO₂ which are both not able to reduce carbon dioxide to CO nor bind the CO₂⁻ intermediate show good catalytic activity towards syngas production when doped with copper metal^{12,70,71}. Metal oxides are often present as 2D materials which is another merit compared to 0D or 1D noble metal catalysts as it was shown that 2D materials have a better contact with conductive substrates leading to an improved electron transfer^{67,72}. Further studies on Co₃O₄ and SnO₂ reveal that ultrathin nanosheets provide a higher charge density and thus higher electrical conductivity, leading to increased Faraday efficiencies for the formate intermediate^{67,73,74}. Tin dioxide nanosheets compared to Sn-metallic foil lead to an increase in formate formation and FE's up to 85 % were reached. Tin dioxide however showed rather poor results in CO production and is thus not recommendable as catalyst for syngas production. Electrochemical syngas production was

reported also with MnO_2 and TiO_2 , the latter is however mainly used as photocatalyst for HER^{67,75–77}.

6.2.3 Metal chalcogenides

Metal chalcogenide catalysts often involve non-noble metals such as indium, molybdenum or tungsten and are often present as 2D materials. A prominent example amongst them are transition metal dichalcogenides (TMDCs) including MoS_2 which is known for its high selectivity toward HER. Asadi *et al.* shown an increased CO_2RR selectivity towards CO at edge positions on MoS_2 ^{12,67,78}. They explained their favoured CO selectivity with a high d-electron density and almost metallic like behaviour at the edges. An increase in CO was noted upon doping MoS_2 with niobium. Studies on In_2Se_3 nanosheets explained the favoured CO production due to electronegative selenium atoms, stabilizing the $^*\text{COOH}$ intermediate^{12,79}. Xie and Li *et al.* noted that creation of an In_2O_3 or SnO_2 -Cu composite material lead to an enhanced performance in syngas production^{12,70,71}. It was noted by various groups that the H_2 :CO ratio could be adjusted by tuning the applied potential, with higher overpotentials increasing CO selectivity^{12,78,79}. Further TMDCs including WSe_2 , WS_2 , MoSe_2 , do as also MoS_2 show satisfactory CO_2RR results. Nanoflakes of these TMDCs favour $^*\text{CO}$ formation and enhance thus the CO_2RR activity towards CO at low overpotentials⁶⁷. A further improvement on CO production was achieved by creating a MoSeS monolayer. CO Faraday efficiencies of 45.2 % were achieved at a potential of -1.15 V *vs.* RHE^{67,80}. Silver chalcogenides as e.g. Ag_2S and Ag_2Se are of great interest for electrochemical measurements due to their high conductivity, low price and non-poisoning characteristics^{55,81–83}. Shen *et al.* reported successful CO_2 reduction to CO using an $\text{Ag}_2\text{S}/\text{Ag}$ electrode in an organic electrolyte using a flow cell. Constant FE_{CO} of about 92 % was reached after 65 min electrolysis time. The FE remained high for a duration of 4 h showing a long term stability of Ag_2S ⁵⁵. Ye *et al.* recently reported their results on electrochemical CO_2RR on $\text{Ag}_2\text{S}/\text{Ag}$ interfaces. They achieved FE_{CO} values of up to 99 % at rather low overpotentials between -0.3 to -0.8 V *vs.* RHE. Hydrogen generation was suppressed by using a highly alkaline electrolyte⁸⁴. Studies which focussed on electrochemical carbon dioxide reduction to CO using Ag_2S and Ag_2Se on carbon based supports in an 0.5 M KHCO_3 electrolyte were published recently^{56,85}. Chen *et al.* reached their highest FE_{CO} value of 95.4 % at -0.8 V *vs.* RHE with an Ag_2S -Au heterogeneous nanocomposite catalyst. At -1.0 V a FE_{CO} of approximately 70 % was obtained with Ag_2S . These results are clearly lower compared to reported values from Ye and Shen *et al.* however hydrogen evolution was expected at carbonaceous catalyst substrates and aqueous bicarbonate electrolyte^{55,84,85}. Comparison of monoclinic (*m*) and orthorhombic (*o*) Ag_2Se electrodes revealed a higher CO selectivity for monoclinic Ag_2Se . At an overpotential of -0.9 V *vs.* RHE a FE_{CO} of 98 % was reached with *m*- Ag_2Se , whereas *o*- Ag_2Se only lead to ~40 % FE_{CO} ⁵⁶. From this results it can be concluded that crystal phase composition plays a major role in CO_2RR selectivity⁵⁶. Both silver chalcogenides show high long term stability and constant CO_2RR performance: *m*- Ag_2Se constantly displayed an average FE_{CO} of above 82 % for over 50 h, the Ag_2S -Au showed a reported stability over 30 h^{56,85}.

6.3 MOCHAs

In 2002 the silver benzeneselenolate, a semiconducting hybrid nanomaterial was first published and characterized by Cuthbert *et al*⁸⁶. Sixteen years later the group of Hohman picked up on this silver benzeneselenolate ($[\text{AgSePh}]_\infty$) topic and extended their research on a whole class of materials consisting of a well-defined nanostructured array of inorganic coordination polymer with a supramolecular lattice of organic ligands⁸⁷. They named this material class “metal organic chalcogenolate assemblies” short “MOCHAs”⁸⁸. The previously mentioned silver benzeneselenolate MOCHA received its own name “mithrene” after the terms “mithril” being a fictional silvered steel and “ene” for its 2D inorganic layered structure⁸⁷. Since 2018 studies on synthesis of MOCHAs and their properties as well as on the development of novel MOCHAs containing different metals, chalcogenides and organic ligands were made. In the following sections, an overview of the so far published synthesis routes and most important properties of MOCHAs especially mithrene will be given. Typical structures of MOCHAs are shown below in **Figure 3**. **A.** shows the polymeric structure of the well-studied MOCHA mithrene, **B.** represents the structure of thiorene, its sulphur containing version. In blue brackets the repeating unit of MOCHA is given.

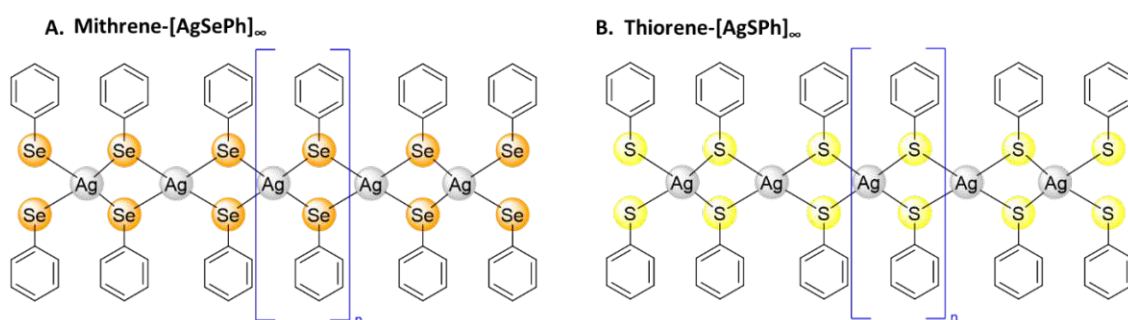


Figure 3. Structures of the **A.** silver benzeneselenolate MOCHA mithrene and the **B.** silver benzenesulphonolate MOCHA thiorene.

6.3.1 Synthesis routes of MOCHAs

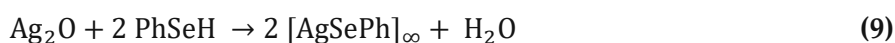
$[\text{AgSePh}]_\infty$ can be obtained *via* a reaction of silver chloride and triphenyl phosphine with PhSeLi in THF and consecutive addition of diethyl ether⁸⁶. The formation of yellow mithrene platelets was observed within a few days⁸⁶. The crystals of silver benzeneselenolate mainly occurred twinned and were not soluble in common solvents⁸⁶.

Another possible synthesis way is the so called “**biphasic synthesis**”. Therefore equal amounts of 1-10 mM aqueous silver nitrate solution and diphenyl dichalcogenide in toluene solution were placed in a vial and kept for an elongated time of 3-10 days⁸⁷. The MOCHA formed on the interface between the aqueous and organic phase. While biphasic synthesis is a very facile and straight forward approach and well suitable for thin films as crystal growth is limited to two dimensions, it comes along with some difficulties and disadvantages as well^{87,89}. Product isolation can be tricky and the yield, limited by the interface is rather low ($\sim 0.1 \text{ mg-1 mg}$)⁸⁷. Further the system of a three-phase chemical reaction environment is complex and sensitive to minor changes to the system. It was found, for example, that small changes in silver concentration can have a huge impact on the morphology and product composition⁸⁷. It was shown that the biphasic approach resulted in a product mixture consisting of crystalline, semiconducting MOCHA and a fibrous,

amorphous metal organic chalcogenolate polymer (MOCP)⁸⁷. As the MOCP was not a desired byproduct, modifications on the biphasic method were made, in order to increase the MOCHA to MOCP ratio. The biphasic synthesis was performed at higher temperatures (80-180 °C) in an autoclave. It was shown that the MOCP byproduct could be eliminated at higher temperatures. Increasing either temperature or duration lead to the formation of uniform crystals whereas an excess of temperature and duration increase caused the formation silver agglomerates with an organic chalcogenide rest⁸⁹. Successful MOCHA synthesis was carried out at 80 °C forming largely aggregated crystals⁸⁹. At higher temperatures a larger nucleation density was present due to the increased rate of collisions of reagent with the immiscible interface⁸⁹. It was shown that surfactant addition, lead to a preferred growth in the {001} basal plane, acting most likely as a capping agent⁸⁷. Cold biphasic synthesis at 77 K revealed that mithrene crystals are considered to be the thermodynamic product whereas the amorphous MOCP was primarily formed at low temperatures being the kinetic product⁹⁰. Toluene as the organic phase was exchanged by DCM, DMSO, cyclohexane, ethyl acetate and methyl ethylketone and the influence of different solvents on product yield, morphology, nucleation and growth times was examined by Schriber *et al.*⁹⁰. DCM, an organic solvent with a higher density than water lead to low product yield, as only a thin layer of organic phase was above the aqueous phase. This leads to the assumption that inverting phases causes drastic loss of yield. DMSO on the other hand shows a slight miscibility with water thus no interface was visible. The product however, aggregated on the bottom of the vial, leading a high yield and little MOCP formation. In ethyl acetate the MOCP formation was clearly favoured over mithrene formation. Methyl ethylketone exhibited a very flat meniscus at the interface resulting in only very small and few mithrene crystallites. Cyclohexane on the other hand, has shown a very curved meniscus resulting in satisfying mithrene production. The so produced mithrene however shown a different morphology and the yield was still lower than in DMSO⁹⁰. It was found recently that amine addition to the aqueous phase in the biphasic condition lead to an increase in crystal size from <5 μm up to >1 mm. The same publication also stated a one phase synthesis over a period of 3-5 days of [AgSePh]_n in toluene by addition of PrNH₂⁹¹.

A completely different synthesis route was published in the 2020 by Trang *et al.*⁹². Their idea was the creation of MOCHAs by **tarnishing silver metal** as both tarnish and MOCHA are chalcogenide salts. "Tarnish" usually describes all chemical corrosion products, however often only the Ag₂S is associated with the term "tarnish" ⁹². Metallic silver films were exposed to diphenyl diselenide (DPDSe) at elevated temperatures of 80 °C for 72 h. The addition of water to the reaction vessel lead to an increase in product formation. A yellow/green/golden coloured film appeared. In absence of organic solvents, tarnishing does not lead to self-assembles monolayers (SAMs) but the layered hybrid chalcogenolates. Advantages of this synthesis route are the mild conditions (mild temperatures, no need of high pressures, no special atmospheres required) and its facile preparation. Two mechanistic pathways are discussed in literature: a redox mechanism and an acid base mechanism. It was found that oxygen from air was not crucial for a successful reaction however water was. Eventually it played not a primary role, but secondary in the oxidation

of silver metal. Reaction of silver metal with benzeneselenol lead to no MOCHA formation in oxygen free environment and to a mixture of products upon oxygen presence. It was found that the reaction with benzeneselenol is hardly controllable as all oxidation states are present. When performing a tarnishing reaction with reactants in their highest oxidation state such as Ag₂O with DPDSe no reaction occurred at room temperature. Performing the same reaction at elevated temperature of 80 °C yellow-blackish product was formed. Addition of IPA and stirring overnight lead to a completion of the reaction. These observations suggests an acid base mechanism with a reaction equation as follows:



A possible explanation would be that of a complex formation in the silver selenolate system. This surface bound complex could explain charge transfer from Ag to reduce the diselenide bond in a single adsorption step. MOCHA films of 5 to 100 nm could be obtained with the tarnishing approach. Short reaction times lead to incomplete reaction with remaining silver films whereas longer reaction times resulted in a full consumption of silver films. Placing silver metal into a solution of DPDSe lead to a slightly yellow appearance of the silver metal but a low yield with high amounts of amorphous MOCP⁹². Reaction of silver metal with diphenyl disulphide has not been successful, this might be due to the higher affinity and stronger interaction of n-alkylselenolates compared to thiolates⁹²⁻⁹⁸. Additionally metal-selenide interactions are stronger due to their more dynamic binding configuration and have a higher stability compared to sulphur^{92,93,96,99,100}. Yeung *et al.* used a slightly adapted synthesis route for the preparation of copper-, indium-, lead- and tin- selenide MOCHAs¹⁰¹. Prior to tarnishing, metal thin films were deposited on substrates *via* thermal evaporation. Thiophenol or benzeneselenol were added and reaction times were varied between 0.5-14 h depending on the metal thickness. Rather mild temperatures between 60 and 120 °C were chosen. Each metal+chalcogenide combination resulted in slightly different product. Copper and benzeneselenol lead to the formation of a 1D copper (I) benzeneselenolate coordination polymer. Lead benzenthioate showed a very distinct structure from [PbSePh]_∞ and other MOCHAs. The indium(III) benzeneselenolate exhibited a mixture of structural phases. Tin and benzeneselenol lead to the formation of irregular, non-uniform [SnSePh]_∞ crystals¹⁰¹. Studies in 2020 revealed that the morphology of the silver and silver oxide films play a major role on the characteristics of the final mithrene film¹⁰². A hypothesis by Maserati *et al.* states that silver oxide is a mixture of three different oxides (AgO, Ag₂O, Ag₂O₃) which undergo thermal decomposition to Ag₂O which then can react with the benzene-selenol to the desired mithrene MOCHA¹⁰²⁻¹⁰⁴. In the same year the effect of boron-selenide and boron-sulphide bonds as ligands on the formation of copper based MOCHAs was studied¹⁰⁵. In the biphasic approach metal complexes are formed at the interface between the organic chalcogenolates and the metal cations. These complexes propagate the growth of small crystallites which is strongly influenced by the steric environment of the organic chalcogenolates. Functionalized boron clusters were shown to form “defect-free” monolayers of copper based MOCHAs¹⁰⁵.

Above mentioned limitations and challenges of the currently available synthesis methods make the development of a universal synthesis route needed in the field. The desired

synthesis method should be facile, economic and quick, achieving the formation of uniform MOCHA particles with their characteristic properties.

6.3.2 Properties of MOCHAs

Mithrene ($[\text{AgSePh}]_{\infty}$) a sheet-like, direct semiconducting, homoleptic coordination polymer shows a 2D in plane coordination of metal (silver) and chalcogenide (selenium) atoms with organic ligand (phenyl) groups in between causing insulation and weak out of plane bonding through Van der Waals interactions^{86,89}. The planes consist of lamellar stacking of silver-selenium monolayers. The most intense planes of this unit cell can be observed in the XRD pattern of mithrene and other MOCHAs corresponding to the {002}, {004} and {006} crystallographic plane⁸⁷. The crystal structure was not influenced by the synthesis temperature⁸⁹. The intensity of those peaks however increased, with increasing thickness of MOCHA⁹². Cuthbert *et al.* showed the presence of mithrene in the monoclinic space group $C2/c$. Recently it was confirmed that $[\text{AgTePh}]_{\infty}$ (tethrene) was also present in the $C2/c$ space group¹⁰⁶. Thiorene $[\text{AgSPh}]_{\infty}$ on the other hand showed a C/c space group¹⁰⁶. The silver atoms in mithrene and tethrene formed a distorted tetrahedral coordination with a sheet consisting of compromised silver hexagons. In thiorene on the other hand, the argentophilic network is reported to be linear¹⁰⁶. Silver atoms are capped from both sides by μ_4 -SePh ligands resulting in the formation of Se “monolayers”⁸⁶. Silver-selenide-silver layers show a distance of roughly 1.2 nm, the Ag-Se distance is about 2.7 Å, Ag(I) Ag(I) d^{10} - d^{10} contacts are roughly 3 Å and average Se distances are larger 4.5 Å⁸⁶.

Tethrene as well as mithrene show a strong light-matter interaction. Thiorene does not emit light in the visible range¹⁰⁶. This difference in light emission could be explained by the non-supported 2D delocalization of excitations in thiorene due to its linear Ag-Ag chains. Mithrene and tethrene *en contraire*, due to their tetrahedral network enable exciton delocalization in two dimensions¹⁰⁶. Tethrene being an orange crystalline substance with an indirect bandgap, shows longer and broader emission lifetime (1 ns) compared to mithrene¹⁰⁶. Blue emissive behaviour of mithrene was noted at 467 nm. The emission is independent from crystal size, shape or morphology. Only a slight red shift was observed in highly distorted or defective crystals or due to large Ag particles in case of the tarnishing synthesis method^{87,92}. No correlation could be found between the emission intensity and the crystal aspect ratio and the photoluminescence intensity does not depend on the lateral size of MOCHAs. A correlation was noted however, between crystal thickness (No° of layers) and emission intensity⁸⁷. Crystalline and amorphous products (MOCHA and MOCP) have a different Ag:Se ratio. The crystalline phase has a reported 1:1 ratio whereas the amorphous phase has a 2:1 ratio. Light illumination could not influence this ratio⁸⁷. GIWAX measurements confirmed that mithrene dissociated *via* a redox mechanism in which silver ions are reduced to silver metal. TGA experiments showed a mass loss of 59.1 % close to 200 °C which is correlated with the loss of the benzeneselenolate ligand. Reversibility of this reaction was proven by the tarnishing approach⁸⁹. GIWAX experiments also made it possible to see the reaction progress of a tarnish reaction as with shorter reaction times silver metal Debye-Scherrer rings were present, meaning an incomplete or not finished reaction⁹². Beside mithrene also MOCHAs involving different metals as copper, indium, tin and lead have been reported¹⁰¹. XPS measurements confirmed that all tested metals were turned into the

chalcogenolate as energy loss features disappeared¹⁰¹. Further selenide shows its characteristic binding configuration independent from the metal involved. During tarnishing all metals undergo a certain surface oxidation which did not interfere with the tarnishing reaction^{92,107-111}. Copper based MOCHAs do, as also silver based MOCHAs, have promising optoelectronic properties. It is however hard to estimate if an electronic measurement is due to the intrinsic properties of the MOCHA material or only the results of defects¹⁰¹. [CuSePh]_∞ does show a red photoluminescence at 715 nm at room temperature¹⁰¹.

The above mentioned facile synthesis methods and diverse properties of MOCHAs make these structures an interesting and promising class of materials for applications in sensing, catalysis, mechanochemistry, photovoltaics or LEDs^{87,112}.

7 Motivation and Aims

The *Introduction* stated already briefly that the reduction of carbon dioxide to reach a zero net CO₂ emission value is one of our biggest chances in fighting climate change and global warming. As was already mentioned beforehand the independence from natural gas and fossil fuels would be a great step to achieve this goal. Syngas being an important feedstock for the production of many essential chemicals nowadays is mostly produced from natural gas. Combining the reduction of carbon dioxide with the production of syngas by means of (photo)electrocatalysis was a big motivation to this work. Further research on the relatively new materials class MOCHAs was further motivating.

The aims of this thesis therefore was/were:

- The **development of a facile synthesis route** for MOCHA production. To this date MOCHAs have been prepared via various strategies and their structural and optoelectronic properties have been studied. The here developed synthesis route should be preferably as simple and safe as possible and should increase the yield of MOCHAs and thus facilitate easier sample handling.
- The **testing of already known MOCHAs [AgSePh]_n and [AgSPh]_n as potential catalysts for (photo)electrochemical CO₂ reduction / Syngas production**. To this date, no application of MOCHAs in catalysis has been explored.
- The **stability testing of MOCHAs**. Stability testing, including stability over a wide pH and temperature range, in solvents and upon incident light should be useful information in the assessment of MOCHAs for potential applications.
- The **synthesis and characterization of “new” MOCHAs**. It should be investigated whether other metals in combination with diphenyl dichalcogenides do also form a polymeric metal organic chalcogenolate assembly. Structural confirmation of these new MOCHAs is essential and further characterization by means of ATR-FTIR, SEM, TXRF, XPS and powder XRD should be made.

8 Experimental

In this chapter used chemicals and instruments are summarized. A brief overview of the various synthesis routes for MOCHA production is given. The electrode preparation is described. Characterization techniques, (photo)electrocatalytic measurements and stability testing are explained.

8.1 List of used chemicals and instruments

Table 2 presents all the used chemicals in **Table 3** the utilised instruments are summarized.

Table 2. Names and abbreviations of used chemicals, their CAS-number, supplier and purities.

Chemical / Material	Abbreviation	CAS-No°	Supplier	Purity
Acetone	-	67-64-1	-	technical
Acetonitrile	MeCN	75-05-8	VWR	-
Argon	Ar	7440-37-1	-	-
Carbon black	C	1333-86-4	Cabot	-
Carbon dioxide	CO ₂	124-38-9	-	-
Carbon paper	CP	-	Thermo Scientific	-
Chloroform	CHCl ₃	67-66-3	Sigma Aldrich	99 %
Copper(II)nitrate trihydrate	Cu(II)(NO ₃) ₂ 3H ₂ O	10031-43-3	Merck	99.5 %
Copper sulfate	CuSO ₄	7758-98-7	-	99 %
Coronene	C ₂₄ H ₁₂	191-07-1	TCI	>83 %
Dichloro methane	DCM	75-09-2	Fluka	-
Diethyl ether	Et ₂ O	60-29-7	-	-
Dimethyl formamide	DMF	68-12-2	-	-
Dimethyl sulfoxide	DMSO	67-68-5	abcr	-
Diphenyl diselenide	DPDSe	1666-13-3	Fluka	95 %
Diphenyl disulfide	DPDS	882-33-7	Acros Organics	99 %
Diphenyl ditelluride	DPDTe	32294-60-3	Sigma Aldrich	98 %
Ethanol	EtOH	64-17-5	-	technical
Ethanol	EtOH	64-17-5	Chem-Lab	absolute
Ethylacetate	EtAc	141-78-6	-	-
Fluorine doped tin oxide	FTO	-	-	-
Glassy Carbon	GC	1333-86-4	-	-
Helium	He	7440-59-7	-	-
Iron (III)nitrate nonahydrate	Fe(III)(NO ₃) ₃ 9 H ₂ O	7782-61-8	abcr	98.7 %
Isopropanol	IPA	67-63-0	-	technical
Isopropanol	IPA	67-63-0	-	absolute
Magnesium sulfate	MgSO ₄	7487-88-9	Sigma Aldrich	>99.5 %
Methanol	MeOH	67-56-1	VWR	HPLC gradient grade

Chemical / Material	Abbreviation	CAS-No°	Supplier	Purity
MicroPolish Powder	-	-	CH Instruments	0.05 micron
MicroPolish Powder	-	-	CH Instruments	1.0 micron
Nafion™	-	31175-20-9	Sigma Aldrich	5 wt. % in lower aliphatic alcohols and water
Nickel(II)nitrate hexahydrate	Ni(II)(NO ₃) ₂ 6H ₂ O	13478-00-7	Sigma Aldrich	99.999 %
Nickel sulfate	-	10101-98-1	Riedel de Haen	p.a
Nitrogen	N ₂	7727-37-9	-	-
Poly methyl methacrylate	PMMA	9011-14-7	Bangs Laboratories	-
Potassium chloride	KCl	7447-40-7	Baker	99.7 %
Potassiumcyanide	KCN	151-50-8	Merck	99.5 %
Potassium hexacyano ferrate trihydrate	K ₃ (CN) ₆ 3H ₂ O	14459-95-1	Merck	99 %
Potassium hexacyano ferrate	K ₂ (CN) ₆	13746-66-2	Merck	99 %
Potassium hydrogen carbonate	KHCO ₃	298-14-6	Acros Organics	>99.5 %
Potassium hydroxide	KOH	1310-58-3	Merck	p.a.
Quinacridone	C ₂₀ H ₁₂ N ₂ O ₂	1047-16-1	TCI	>93 %
Silver nitrate	AgNO ₃	7761-88-8	Abcr	99.9 %
Silver oxide	Ag ₂ O	20667-12-3	Sigma Aldrich	99 %
Silver paste (Leitsilber)	-	-	-	Ag in EtAc
Silver sulfate	Ag ₂ SO ₄	10294-26-5	Merck	99.5 %
Sodium citrate dihydrate	Na ₃ C ₅ H ₅ O ₇ 2H ₂ O	6132-04-3	Baker	99.7 %
Titanium(IV)oxide	TiO ₂	1317-70-0	Sigma Aldrich	99.7 %
Toluene	-	108-88-3	Fluka	>99.7 %
Water	H ₂ O	7732-18-5	-	-

Table 3. Instruments and devices used to perform the here presented work.

Instrument	Name	Vendor	Settings
ATR-FTIR	Tensor 27	Bruker	-
Balance	-	Soehnle	-
Blue light lamp	PR160L-456 nm	Kessil	456 nm
Centrifuge	-	Sigma	-
GC-MS	Nexis GC-2030	Shimadzu	-
Hot / stirring plate	MR 3001 K	Heidolph	300 rpm
Membran filter	NYLON	Cole-Parmer	0.45 μm , 47 mm
Microwave oven	Monowave 300	Anton Parr	-
Muffle oven	-	Binder	-
Potentiostat / Galvanostat	-	Autolab	-
Potentiostat / Galvanostat	2450 Source Meter	Keithley	-
SEM / EDX	-	-	-
Solar simulator	-	-	-
Sonication bath	Ultrasonic cleaner	VWR	-
Sonication bath	Sonorex Digitec	Bandelin	-
Spectrophotometer	JASCO V-670	JASCO	DRS
Spin coater	G3P-12 Spincoat	Cockson Electronics	-
TXRF	Atomika 8030C	Atomika	MoK α 50 kV 47 mA
UV-lamp	-	Thorlabs	365 nm
Vacuum pump	-	Ilmvac	-
Ventilator	DS09225R12MC018	AVC	12 V, 0.2 A
XPS	-	SPECS	Al-K α SCIENTA RS4000 photoelectron analyzer
XRD	X'Pert Pro multi-purpose diffractometer (MPD)	PANalytical	Cu-anode 1.5406 Å Bragg Brentano

8.2 MOCHA Synthesis

The sections on MOCHA synthesis describe the biphasic and tarnishing approach which were used as mentioned in literature^{87,89,92}. Adapted synthesis methods of MOCHAs including microwave and hydrothermal synthesis were developed during this work and are presented as well. As to this date no information on potential hazards of MOCHAs are known, yet then handling should be performed with highest caution. Gloves should be worn at all times, contact must be limited to a minimum and release into the environment should be avoided at all costs.

8.2.1 Biphase synthesis of MOCHAs

Biphase synthesis was performed as described by Schriber *et al.*^{87,89}. 3 mL of a 3 mM aqueous solution of AgNO_3 were placed in a 20 mL glass vial. On top of it an equal amount of 3 mM DPDX ($X=\text{S, Se}$) in toluene solution was pipetted. The vials were capped and stored in darkness at room temperature for one week. Harvesting of crystals was performed by two different approaches. In the first approach the glass vial was tilted 45° and the MOCHA crystals were fished by a glass or FTO substrate. The second approach consisted of pipetting off the aqueous layer followed by careful decantation of the upper organic layer. The remaining crystals were suspended in IPA, centrifuged and decanted off.

8.2.2 Tarnishing synthesis of MOCHAs

Copper plates with and without displaced silver layer onto them and helical shaped silver wire were placed together with 100 μL water and 50 mg diphenyl dichalcogenide (DPDSe, DPDS, DPDTe) in a glass vessel. The glass jar was placed in an oven and kept there for 72 h at 80°C . After performed synthesis the glass jar was removed from the oven, cooled down and the electrodes were taken out.

8.2.3 Microwave synthesis of MOCHAs

MOCHA synthesis was carried out in an Anton Paar Monowave 300 microwave oven which can be seen in **Figure 4** below. Various reaction conditions using different precursors and reactant concentrations, reaction times as also reaction temperatures were explored. In **Table 6** in the appendix all tested conditions are summarized. **Table 6** also indicates which synthesis was successful in MOCHA production and which resulted in an uncomplete reaction. The following procedure was chosen as the standard microwave synthesis procedure for MOCHA synthesis after various testing: 0.5 mmol of metal nitrate (AgNO_3 , $\text{FeNO}_3 \cdot 9\text{H}_2\text{O}$, $\text{NiNO}_3 \cdot 6\text{H}_2\text{O}$, $\text{CuNO}_3 \cdot 3\text{H}_2\text{O}$) were dissolved in 2 mL of H_2O . 0.75 mmol of diphenyl dichalcogenide (DPDS, DPDSe, DPDTe) were suspended in 5 mL of MeOH and sonicated for about 30 min until all the powder was dissolved. The organic and aqueous solutions were combined in a microwave vial equipped with a stirring bar and capped. When combining the organic and aqueous precursor solutions, instantly a precipitate was formed. The vial was placed in the microwave oven and the programme was started. The standard programme was running for 5 h at a constant temperature of 110°C and 600 rpm and is shown in **Figure 4 B**.

After successful synthesis, the formed precipitate was filtered off *via* vacuum filtration, washed thoroughly with water and methanol to get rid of unreacted precursors. The MOCHA powder was then dried overnight in an oven at 40°C .

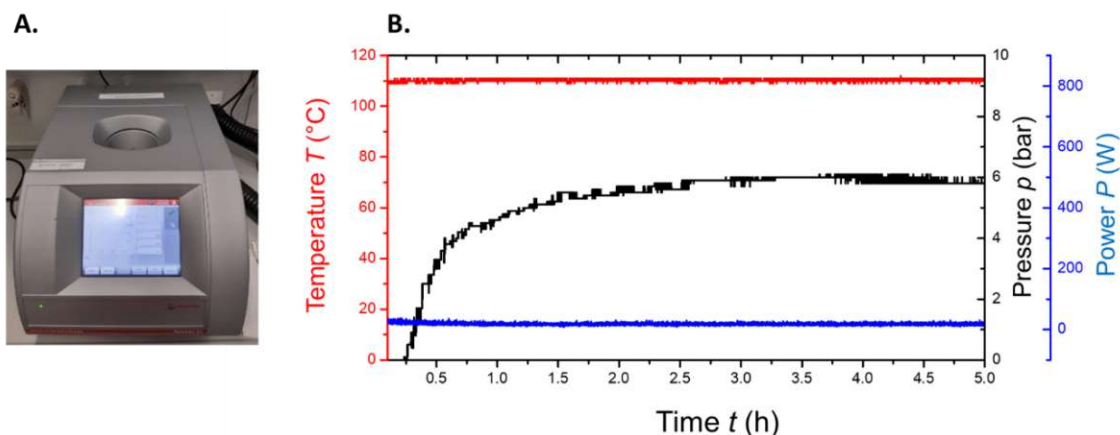


Figure 4. A. Microwave oven and B. temperature, pressure and power behaviour during 5h MOCHA synthesis.

8.2.4 Hydrothermal synthesis of MOCHAs

The reactor vial used in the microwave synthesis was limited to the solvent volume of 7 mL to ensure enough headspace for a safe reaction. In order to upscale the reaction, hydrothermal synthesis was used. Hydrothermal synthesis of MOCHAs is already described in literature, however the reported method is a biphasic synthesis, which leads to a very low yield of ~ 1 mg $[\text{AgSePh}]_{\infty}$ per synthesis⁸⁹. The reactant amount in the microwave synthesis was tripled leading to 1.5 mmol (175 mg) of AgNO_3 in 6 mL H_2O and 2.25 mmol (702 mg) of DPDSe in 15 mL MeOH . The two solutions were combined in an autoclave and placed in an oven at 150°C for 72 h (3 days) and 120 h (5 days). The resulting mithrene was treated in the same way as after microwave synthesis.

8.3 Electrode preparation

Microcrystalline MOCHA powder was obtained after microwave synthesis. For electrochemical investigation and experiments it was necessary to deposit the MOCHA onto an electrode substrate. The steps to fulfil this task are described in the following chapters:

8.3.1 Ink preparation

A so called “ink” from the MOCHAs mithrene ($[\text{AgSePh}]_{\infty}$) and thiorene ($[\text{AgSPh}]_{\infty}$) was prepared. Therefore 100 mg of each MOCHA powder were suspended respectively in 9.5 mL IPA and 500 μL NafionTM were added as a binding material. The ink was sonicated for 30 min and stored at room temperature in darkness.

8.3.2 Deposition methods

“Spincoating”, “dipcoating”, “dropcasting” and “painting” were investigated on their ability to deposit the ink on the electrode substrate carbon paper (CP). Toray carbon paper was used as received without pre-treatment and cut into 2x1 cm pieces. All electrochemical experiments were performed with carbon paper as a substrate, except chopped light chronoamperometry was done, using FTO electrodes.

“Spincoating” was performed with a *G3P-12 Spincoater*. The electrode substrate was placed in the middle of the plate and 100 μL ink were brought onto the CP. The ink was spincoated onto the substrate for 30 seconds at 3500 rpm.

100 μL ink were equally distributed over the CP surface and let dry in air for the “dropcasting” approach.

For the “painting” deposition a paint brush was dipped into the ink and brushed across the CP surface until all the visible surface area was covered with ink.

For the “dipcoating” method five electrode substrates were fixated with Kapton tape on the inner side of a glass vial. The vial was then filled with 5 mL of the previously prepared MOCHA ink. The electrodes were kept for 24 h in the suspension.

After deposition the electrodes were dried in air, dipped into IPA and gently blown dry with compressed nitrogen. For the photocurrent measurements, dipcoated FTO was prepared.

8.3.3 Deposition of silver nanoparticles

A 0.1 M aqueous solution of AgNO_3 was prepared and the dip coated MOCHA electrodes were immersed into the solution and irradiated for 30 min with a 456 nm *Kessil PR 160L* lamp.

8.4 Characterization methods of electrodes and MOCHAs

The following sections give an overview of the utilized characterization techniques. These techniques were used to investigate the powder MOCHA as well as their electrochemical behaviour on CP and FTO substrates.

8.4.1 Attenuated total reflection Fourier transformed infrared spectroscopy (ATR-FTIR)

A *Bruker Tensor 27* spectrometer was used for FTIR measurements. Beforehand a background spectrum of air without a sample was recorded. A few milligrams of powder were then placed on the diamond and pressed down. The ATR-FTIR spectra were recorded in the range of $600\text{-}4000\text{ cm}^{-1}$ and the previously taken background was directly subtracted.

8.4.2 Diffuse reflectance spectroscopy (DRS)

DRS measures reflectance of powdered samples. This is made possible by a special measurement arrangement consisting of a reflection sphere. Reflectance can be converted into absorbance by using the Kubelka-Munk equation. Some assumptions such as an infinitely thick sample and the perpendicular flux in opposing directions of incident and scattered light to the sample surface have to be made when using this approach¹¹³.

DRS experiments were done on a *JASCO V-670 spectrophotometer* within the wavelength range from 200-900 nm. For baseline measurements MgSO_4 powder was used. After the baseline measurement the sample holder was cleaned and microcrystalline MOCHA powder was placed inside the holder.

8.4.3 Electrochemical methods

Electrochemical measurements were performed in an H-cell using an *Autolab PGSTAT302N potentiostat/galvanostat*. The working electrode (WE) was the electrode of interest to investigate and the counter side was equipped with a Pt-counter electrode (CE). For all electrochemical measurements 0.5 M KHCO_3 was used as an electrolyte and the cell was purged prior to experiments for 30 min with N_2 or CO_2 depending on the experiment in order to provide an oxygen free environment and saturate the cell with CO_2 for syngas production. Oxygen would disturb the measurements as in the tested potential range oxygen reduction to hydrogen peroxide or water might occur. This would cause a side

reaction and thus lead to false Faradaic efficiencies. As handling in the laboratory proved to be easier when using reference electrodes for all measurements an Ag / AgCl / 3M KCl reference electrode was used. However, comparisons between different laboratories cannot be made with this electrode, which is why all graphs were plotted using potentials *vs.* the reversible hydrogen electrode (RHE).

By means of the Nernst equation:

$$E = E^0 + \frac{R \cdot T}{z \cdot F} \cdot \ln \frac{a_{Ox}}{a_{Red}} \quad (10)$$

with

$$\frac{R \cdot T}{z \cdot F} = 0.059 \text{ V} \quad (11)$$

R...ideal gas constant (=8.314 J mol K⁻¹)

T...standard temperature of 298 K

F...Faraday constant (96485 C mol⁻¹)

z...Number of transferred electrons (z=1)

and the pH of the electrolyte, the electrode potential *vs.* RHE could be calculated with the following equation:

$$E_{RHE} = E_{Ag / AgCl}^0 + (pH \cdot 0.059) + E_{Ag / AgCl} \quad (12)$$

with

E_{RHE}...potential *vs.* RHE (V)

E⁰_{Ag/AgCl}...standard potential of the Ag/AgCl / 3M KCl electrode at pH 7, 25 °C and 1 atm (V)

E_{Ag/AgCl}... potential *vs.* Ag / AgCl / 3M KCl (V)

The standard potential of the Ag/AgCl / 3M KCl electrode was taken from literature and reached a value of 0.210 V¹¹⁴. The pH of 0.5 M potassium bicarbonate was 8.5 under N₂ saturated atmosphere and 7.5 under CO₂ atmosphere.

8.4.3.1 Linear sweep voltammetry (LSV)

Linear sweep voltammetry was performed in darkness and upon light illumination in nitrogen and carbon dioxide saturated atmosphere. A scan rate of 50 mV s⁻¹ was used and the potential was swept from 600 mV to -1000 mV *vs.* RHE.

8.4.3.2 Photocurrent measurement

Light of different wavelengths (365 nm, 456 nm and VIS solar simulator light) was used for photocurrent determination. Photocurrent measurements were done at constant potential (chopped light chronoamperometry). A potential of -0.3 V *vs.* RHE was applied and kept for 15 min. After letting the current stabilize for 5 min, the light was chopped every two minutes resulting in an increase of current when light was “on” and a sudden jump to more negative currents when the light was “off”. The difference between the “on” and “off” current can be accounted as the photocurrent.

8.4.4 Scanning electron microscopy/Energy dispersive X-ray spectrometry (SEM/EDX)

SEM / EDX measurements were performed by Dr. Doğukan Hazar Apaydin, Stephen Myakala and Jakob Blaschke on a *FEI Quanta FEG 250*. The acceleration voltage was depending on the measurement 10 or 20 kV and the working distance was set between 9 - 10 mm. EDX measurements were performed at the same instrument using an *Octane Elite Super* detector. The used acceleration voltage for EDX measurements was 20 kV, a resolution of 125.2 eV, a take-off angle of 31.7 ° were applied.

8.4.5 Total X-ray fluorescence spectroscopy (TXRF)

TXRF measurements were done by Pablo Ayala. The measurements were conducted on an *Atomika 8030C X-ray fluorescence analyser*. The analyser was operated in total reflection geometry and an energy dispersive Si-detector was used. The excitation wavelength was $\text{MoK}\alpha$ with an acceleration voltage of 50 kV, the current was set to 47 mA and the measurement time was 100 s per sample. Prior to measurement all reflectors were washed thoroughly and measured to ensure true blanks. Roughly 1 mg of the MOCHA powder sample was placed on the reflectors and covered with 5 μL of a 1 % PVA solution to avoid contamination of the detector by flying powder particles. The reflectors were dried for 5 min on a hot plate, cooled down and where then loaded into the analyser.

8.4.6 X-ray photoelectron spectroscopy (XPS)

MOCHA powders were suspended in IPA and the suspension was drop casted onto a Si (711) single crystal surface. The samples were placed in the XPS instrument. XPS measurements were performed by Bernhard Fickl and Jakob Rath on a SPECS instrument, facilitated by the AIC, TU Wien. A monochromatic $\text{Al-K}\alpha$ source with a wavelength of 1486.6 eV was used. The device was equipped with a hemispheric SCIENTA RS4000 photoelectron energy analyzer.

8.4.7 X-ray diffraction (XRD)

Powder samples were placed on a Si (711) holder. When suspensions were measured, the sample was drop casted onto the Si holder and the solvent was evaporated in air. After sample preparation the Si holders were placed in an auto sampler and placed into the *PANalytical X'Pert Pro multi-purpose diffractometer (MPD)*. The diffractometer was configured in Bragg Brentano geometry and was equipped with a Cu anode. The primary beam had a wavelength of 1.5406 Å consisting of $\text{CuK}\alpha$ and $\text{CuK}\beta$ radiation in the ration 2:1. The chosen programme was running for 21 min, scanning the sample between 5-90 ° with a scan rate of 4° min⁻¹. The sample holder was rotated during measurement to ensure an as “ideal” powder as possible.

8.5 Catalytic testing of MOCHAs

As mentioned already in the chapter on motivation of this thesis, it was the major goal to test and investigate the capability of MOCHAs to reduce CO_2 and thus convert it into syngas which can then be further used in various applications mentioned before. Catalytic testing of MOCHAs was done via (photo) electrochemical CO_2RR . Products were analysed by means of gas chromatography. Faraday Efficiency and rate calculations are used to estimate the performance and enable comparison between measurements. A scheme of the experimental setup is shown in **Figure 5** below.

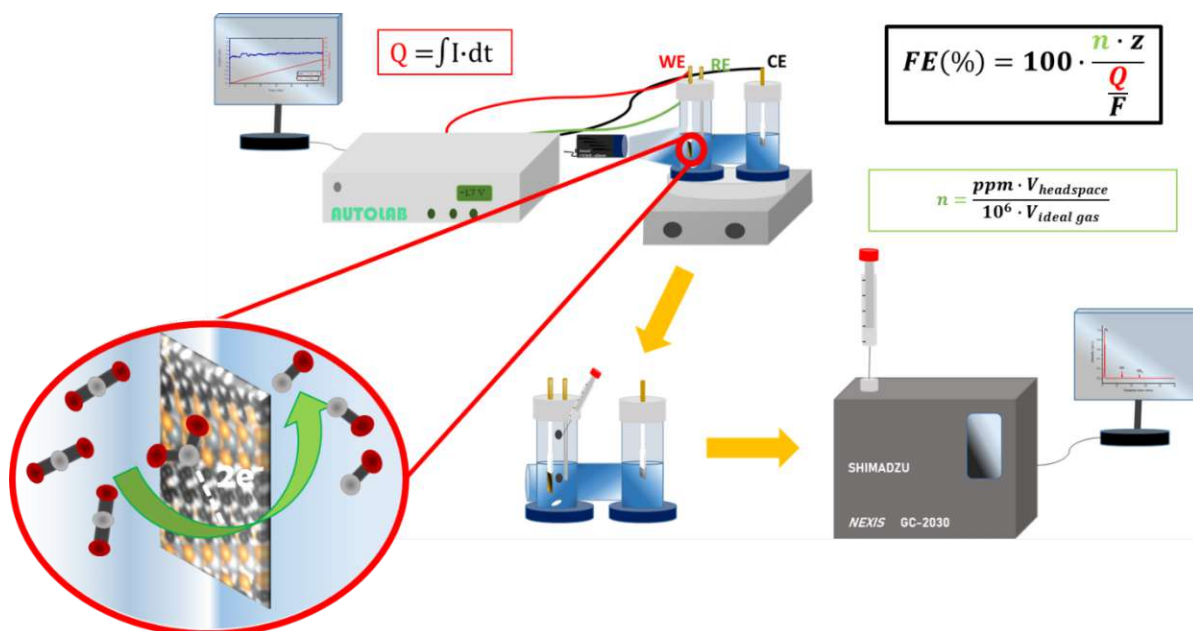


Figure 5. Schematic of the steps performed for electrocatalytic CO₂RR. Electrochemical cell, connected to a potentiostat displaying current and charge over electrolysis time (up), taking of sample from the headspace of the cell (down middle) and injecting to the GC for product determination and quantification (down left corner) by means of Faraday efficiency (equation upper right corner).

8.5.1 (Photo) electrochemical CO₂RR

The chosen electrolyte for CO₂RR was 0.5 M KHCO₃. Due to the low solubility of CO₂ in aqueous solution, potassium bicarbonate is used being an intrinsic source of carbon dioxide. Prior to use it was placed in a SodaStream causing saturation of CO₂ in the liquid. An H-cell was used, filled with 45 mL electrolyte on each side (anodic and cathodic). The cathodic side was equipped with a stirring bar and the corresponding working electrode (WE) and an Ag / AgCl / 3M KCl reference electrode (RE). Into the anodic compartment a Pt counter electrode (CE) was immersed. The cell was closed and purged for 30 min prior to usage with CO₂ in order to also get the headspace oxygen free and CO₂ rich.

The cell was then connected to an *Autolab potentiostat* and a constant potential (-1.0 V vs. RHE, -0.8 V vs. RHE or -0.6 V vs. RHE) was applied for 30 min. The cathodic compartment was stirred at 500 rpm during chronoamperometry. By integration of the recorded current over time the charge was obtained.

The procedure for photo electrochemical CO₂RR was equal to the described above but light was shone onto the working electrode surface with a 456 nm Kessil PR160L lamp during the electrolysis time.

8.5.2 Gas chromatography (GC)

After performed electrolysis, a sample was taken from the headspace of the cell and injected to the *Shimadzu Nexis GC 2030* at 40 °C. Two *Shimadzu Nexis GC*'s were utilized. One was equipped with a BID detector, the second one was operated with a TCD detector. The calibration for product quantification in the BID-GC required a sample volume of 200 μL. The TCD-GC was calibrated using 500 μL of sample. This temperature was held for 3 min and heated with a linear rate of 10 °C min⁻¹ until 250 °C. The dwell time was set to 5 min and the gas flow rate was 10 mL min⁻¹ with He as a carrier gas. By integration of the peaks in the

chromatogram and a previous calibration the peak area could be correlated to a certain concentration of product.

8.5.3 Faraday Efficiency (FE) and Rate calculation

Faraday efficiency is the ratio between the amounts of electrons used for product formation *vs.* the total amount of electrons used in the process. By integration of the recorded current over time the charge was obtained reflecting the total amount of electrons involved. Mathematically FE can be described as follows:

$$FE(\%) = 100 \cdot \frac{n \cdot z}{Q} \cdot \frac{1}{F} \quad (13)$$

n...amount of the products CO and H₂ (mol)

z...number of electrons involved in the reaction (z=2) for CO₂RR and HER

Q... charge (A· s) after 30 min of electrolysis

F... Faraday constant (F=96485.33 A· s mol⁻¹)

GC analysis reports the amount of products in ppm. Thus conversion into moles was necessary. It was presumed that CO and H₂ behave like ideal gases.

$$n = \frac{ppm \cdot V_{headspace}}{10^6 \cdot V_{ideal\ gas}} \quad (14)$$

ppm...parts per millions of CO or H₂

V_{headspace}... Volume of the headspace of the cell from which the sample was taken from (V=0.1 L)

V_{ideal gas}...Volume of an ideal gas at 296 K (V_{ideal gas}=24.62 L)

The rate (R) was calculated in μmol h⁻¹ as follows:

$$R = \frac{n \cdot 10^6}{t} \quad (15)$$

n...moles of products CO and H₂

t... electrolysis time (h)

8.6 Stability testing on MOCHAs

For testing the stability of MOCHAs approximately 10 mg of [AgSePh]_∞ powder were placed in 2 mL glass vials and sealed. The vial was then exposed to the condition of interest (temperature, light illumination) for a certain amount of time (10 min, 1 h, 24 h, 1 week). For stability tests carried out in liquid environment (pH, organic solvent), [AgSePh]_∞ ink was drop casted onto Si substrates and dried in air. The Si holder was then immersed into the corresponding liquid and kept there in darkness at room temperature for one week. The powders / films were then investigated by means of SEM and XRD.

9 Results and Discussion

In the following chapter, the results of the performed experiments are shown and discussed in detail. First, the different synthesis routes are compared and the electrode preparation techniques are shown. Next, the MOCHA materials, mithrene and thiorene, are characterized by means of ATR-FTIR, DRS, SEM, XPS, XRD techniques. The obtained results are compared with those published by Hohman. The characterization by LSV and photocurrent measurements was performed for the first time. Then the potential application of mithrene and thiorene as (photo)electrocatalysts for CO₂ reduction is shown and discussed. Results of stability tests performed on the MOCHAs, [AgSePh]_∞ and [AgSPh]_∞, are presented. At the end, new MOCHA materials involving different metals with diphenyl dichalcogenide ligands are synthesised and characterized.

9.1 Synthesis and Characterization of electrodes

The various performed synthesis methods for MOCHAs and the deposition methods for MOCHAs onto CP are compared. The appearance of a bare CP, MOCHA / CP and MOCHA / Ag-NP / CP electrode are shown. At the end of this section the synthesised MOCHA materials [AgSePh]_∞ and [AgSPh]_∞ are characterized thoroughly and compared with literature. Results of LSV and photocurrent measurements on these materials are presented for the first time as well.

9.1.1 Synthesis methods

As the biphasic and tarnishing approach come with severe drawbacks, these synthesis methods were not pursued further. The biphasic approach involves the formation of product on the interface between the dense aqueous and the lighter organic phase. The product yield is thus dependent on the concentration of the two phases but most importantly it is limited by the area of this interface. MOCHA formation in either the organic or aqueous phase is here not possible due to the absence of metal nitrate or diphenyl dichalcogenide precursor in either phase. It was reported that biphasic synthesis yielded in 0.1-1 mg of MOCHA product⁸⁷. Approximately ten to twenty-five biphasic syntheses had to be performed to gather enough substance for proper characterization⁸⁹. The use of MOCHA for electrochemical measurements requires the preparation of an ink, which then is brought onto an electrode substrate. Performing 25 syntheses to earn enough product for electrochemical and catalytic measurements is rather tedious and time consuming. The tarnishing approach would have been more suitable for this purpose, however it requires highly pure metal precursors⁹². As no possibility for metal evaporation onto glass substrates was available and the purchase of highly pure metal plates is rather costly it was performed with copper plates, silver wires and chemically displaced silver. Tarnishing copper metal, silver wires and silver displaced onto copper plates into mithrene was not successful in our lab. MOCHAs could not be detected, neither by SEM / EDX nor by XRD. Eventually this was due to lack of purity in the utilized metals. The tarnishing approach for application in electrochemical CO₂ reduction comes along with another condition. As stated before, it requires a metal substrate which will be turned into MOCHA on the surface and then can be used directly as the working electrode. The presence of silver or copper metal beneath MOCHA can however still have an impact on the formation of syngas and influence the

H₂:CO ratio. To overcome the limitation of an interface and the substrate dependence, a bulk synthesis method was searched. Hydrothermal biphasic synthesis of MOCHAs was reported before^{89,90}. Microwave synthesis using water and methanol as solvents for silver nitrate and diphenyl diselenide respectively eliminated both limitations (interface and substrate dependence) and the additional use of heat and microwave assistance enabled a high yield and fast synthesis of MOCHAs. Taking into account a molecular weight of 264 g mol⁻¹ for mithrene, reported by Schriber *et al.*⁸⁹, a yield of 83 % was obtained here (110 mg). Considering the fact that concentrations 50-80 times higher than the ones used in biphasic synthesis were used, the microwave approach enhances the yield reported in literature by a factor of 1.4-2.2⁸⁹.

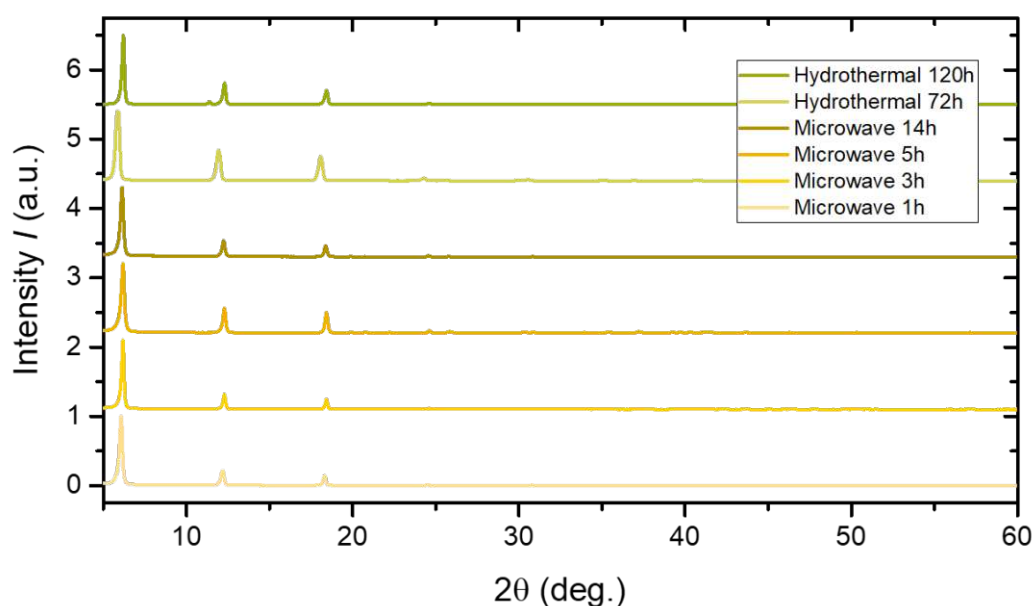


Figure 6. XRD patterns of mithrene synthesized by microwave and hydrothermal autoclave synthesis performed over a time frame of 1-120 hours.

Figure 6 shows that microwave syntheses were performed for 1, 3, 5 and 14 h. All these reactions led to the formation of MOCHAs. MOCHA as a layered material, has a very characteristic XRD pattern, with three peaks corresponding to the {002}, {004} and {006} crystallographic plane in z-direction. As the sharpest peaks in the XRD patterns and best crystallinity were obtained after 5 h, this reaction was chosen as the standard preparation approach. Upscaling the synthesis in the microwave oven was not possible as the used reactor is limited to 7 mL in order to leave enough headspace for a safe and controlled reaction. Due to this, hydrothermal synthesis in an autoclave was performed as well. In contrast to microwave synthesis, the resulting product did not show a bright, intense yellow colour but a rather greenish yellow appearance. XRD measurements (see **Figure 6**) however confirmed a successful mithrene synthesis.

9.1.2 Electrode preparation

SEM images and pictures were taken of the electrodes after successful deposition. The results are shown in **Figure 7**.

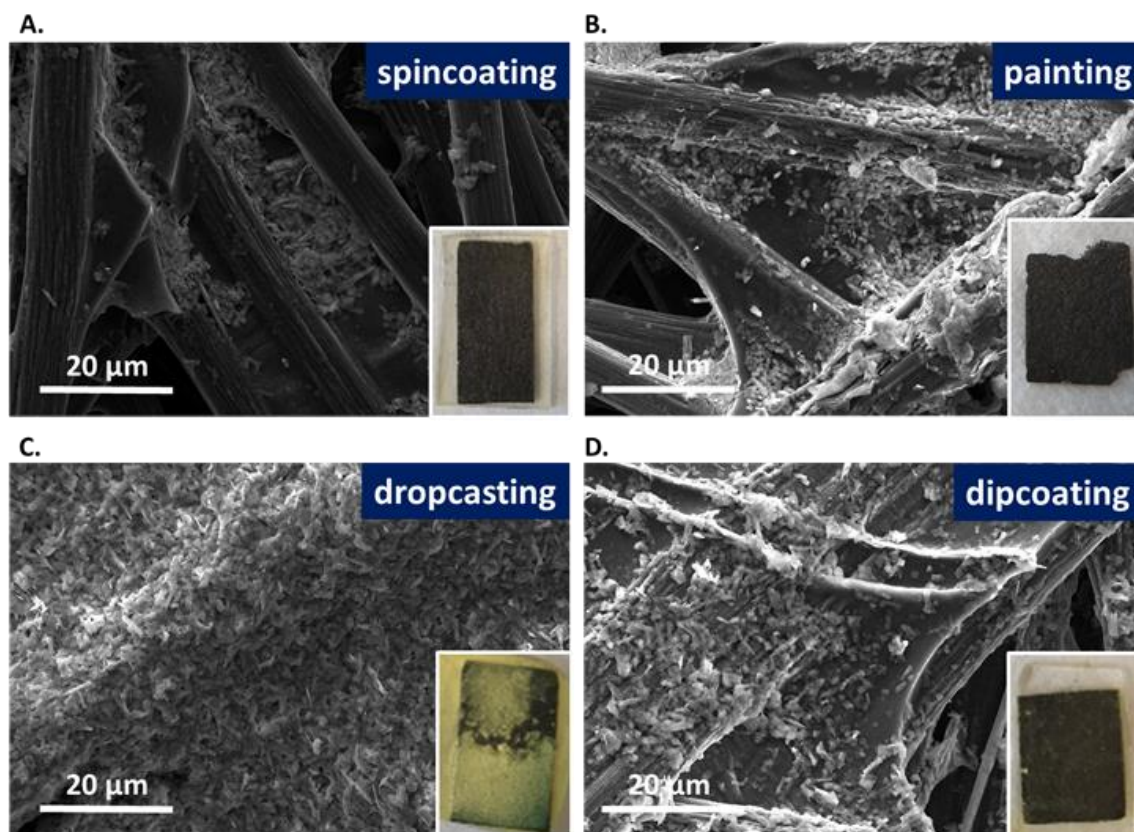


Figure 7. SEM images and pictures (lower right corner) of mithrene on CP prepared using various deposition methods including **A.** spinning, **B.** painting, **C.** dropcasting and **D.** dipcoating.

Spinning led to MOCHA deposition in the spacings between the carbon paper strands, the strands themselves remained mostly uncovered (**Figure 7 A.**). Dropcasting on the other hand, had the opposite effect: the carbon strands were fully covered by MOCHA and it could be hardly distinguished between carbon strands and interspacing areas (**Figure 7 C.**). Painting and dipcoating resulted in a well distributed coverage of MOCHA onto the carbon strands. As painting however is not well reproducible (dependence on how much ink is on the brush, places getting brushed) it was not chosen as a standard deposition method (**Figure 7 B.**). Dipcoating proved to be the best approach as an equal and most importantly reproducible coverage with MOCHA was obtained (**Figure 7 D.**). Consequently, dipcoating was chosen as a standard deposition method for electrode preparation.

9.1.3 Silver nanoparticle deposition

It was of interest to investigate MOCHAs as photosensitizers for electrochemical CO₂RR, using silver nanoparticles as electrocatalysts. As mentioned in the experimental part in section 8.3.3 photochemical silver nanoparticle deposition was performed on top of the deposited MOCHA electrodes. The success of the photochemical deposition technique was checked by means of SEM images. **Figure 8** shows a comparison of the following electrodes: bare CP (**A.**), mithrene on CP (**B.**) and mithrene+Ag-NP on CP (**C.**).

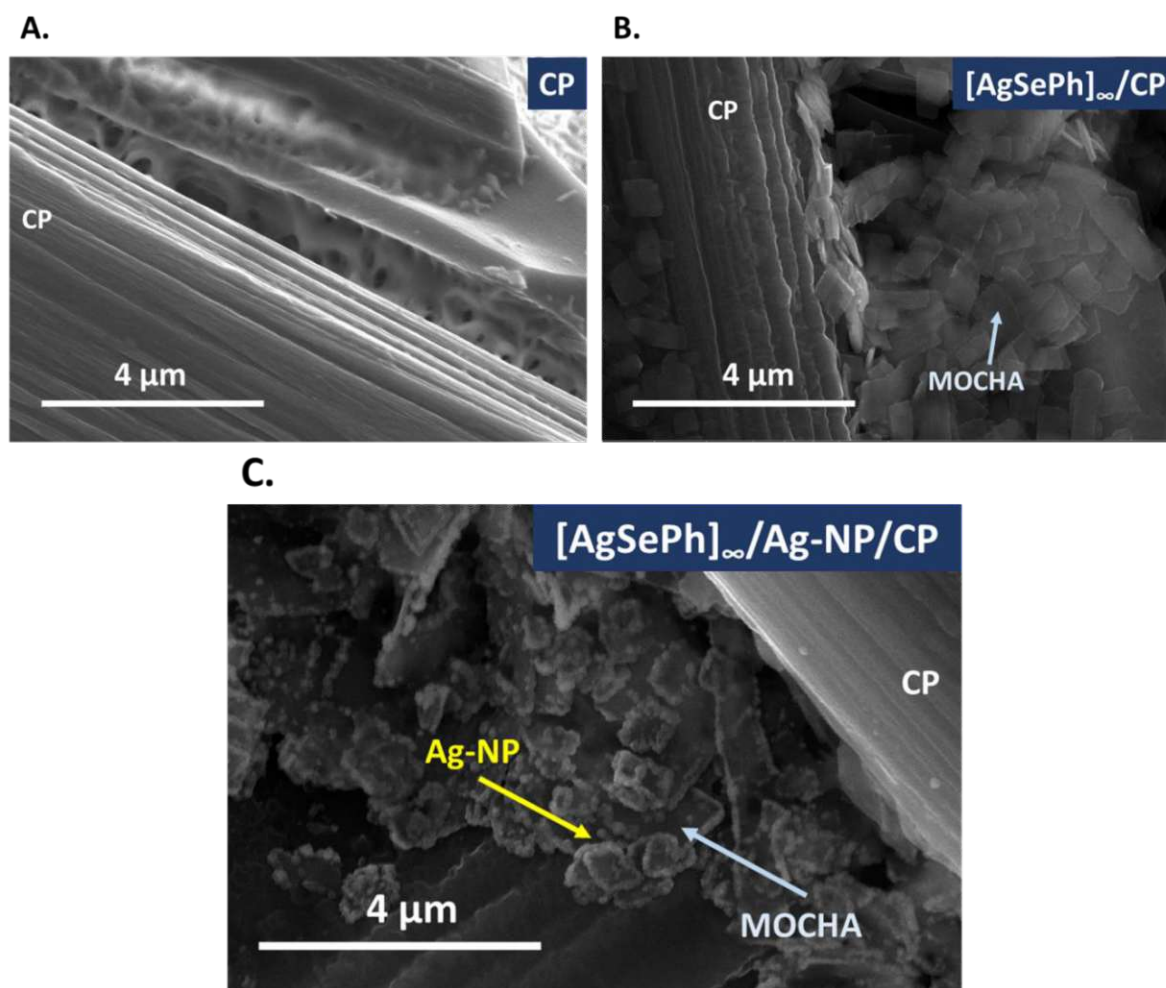


Figure 8. SEM images of **A.** a bare carbon paper electrode, **B.** an $[AgSePh]_{\infty}$ / CP electrode and **C.** an $[AgSePh]_{\infty}$ / CP electrode with photodeposited silver nanoparticles on it.

Bare CP shows a clean surface area which exhibits fibre like structure on the surface of its carbon strand (**Figure 8 A.**). After dipcoating MOCHA onto CP, the monoclinic platelet like structured mithrene is sitting onto the carbon strands (**Figure 8 B.**). Photodeposition of Ag-NP was successful as can be seen in **Figure 8 C.** The silver nanoparticles (white dots) appear along the edges of MOCHA.

9.1.4 Characterization of electrodes

Imaging-Diffraction-Spectroscopy

Mithrene ($[AgSePh]_{\infty}$) and thiorene ($[AgSPh]_{\infty}$), being both part of the materials class MOCHAs, share many similarities but also differences. Both are 2D, homoleptic, polymeric hybrid materials^{86,87,106}. Their monoclinic, platelet, layered shape is apparent in the SEM images shown in **Figure 9 A.** Their XRD pattern shows peaks corresponding to the characteristic interlayer planes {002}, {004} and {006} of their unit cells⁸⁶. These three sharp peaks were observed in the XRD pattern of the microwave and hydrothermally synthesized MOCHAs (see **Figure 6** and **Figure 9**). Mithrene has a bright yellow appearance and shows emissive behaviour⁸⁷. In contrary to mithrene, thiorene is white and does not have an emissive profile in the visible range¹⁰⁶. This difference between $[AgSePh]_{\infty}$ and $[AgSPh]_{\infty}$ can

be explained by a structural difference. While in mithrene the Ag–Ag bond is part of a trigonal network, in thiorene this bond is part of a linear chain¹⁰⁶. As a result, mithrene crystallizes in the $C2/c$ space group, whereas thiorene in the Cc space group. Schriber *et al.* describe the effect of this difference. In mithrene excitons are delocalized above and below the silver network, leading to absorption and emissive behaviour. In thiorene this 2D delocalization is not possible due to its linear network. This behaviour is reflected in the DRS spectra of mithrene and thiorene. The measurement of the mithrene sample revealed a band gap of 2.74 eV (see **Figure 9 D.**) (orange line) which is in good agreement with reports in literature. Mithrene absorption and photoluminescence emission spectra show prominent peaks around 2.73 and 2.84 eV and mithrene was reported to be a direct band gap semiconductor¹¹⁵. Thiorene on the other hand was determined to be an indirect bandgap semiconductor with no emissive behaviour^{102,106}. The DRS measurements, which can be seen in **Figure 9 C.** confirm an absorption band of thiorene at approximately 3.4 eV (red line) and are in agreement with previous reports¹⁰². ATR-FTIR measurements which were performed on mithrene (orange line) and thiorene (red line) were compared to results from literature. FTIR measurements are especially useful to see possible impurities, oxygen contaminations and unreacted silver or benzeneselenol / benzenethiol species. It can be seen that both MOCHAs exhibit the same characteristic bands. The absence of the 2305 cm^{-1} band reveals a successful reaction with no unbound or not reacted benzeneselenol or benzenethiol left¹¹⁶. The most characteristic bands of MOCHAs appear between 632 cm^{-1} and 3070 cm^{-1} . Vibrations at high wavenumbers around 3054 cm^{-1} can be seen in both MOCHA spectra and are assigned to aromatic C–H stretches. At frequencies of 1434 cm^{-1} , 1471 cm^{-1} , and 1572 cm^{-1} aromatic C–C stretches are observed. Aromatic C–H in plane vibrations appear at 995 cm^{-1} , 1018 cm^{-1} and 1067 cm^{-1} . At lower wavenumbers the aromatic C–H out of plane vibrations are notable at 615 cm^{-1} , 688 cm^{-1} , 725 cm^{-1} and 738 cm^{-1} ¹¹⁶.

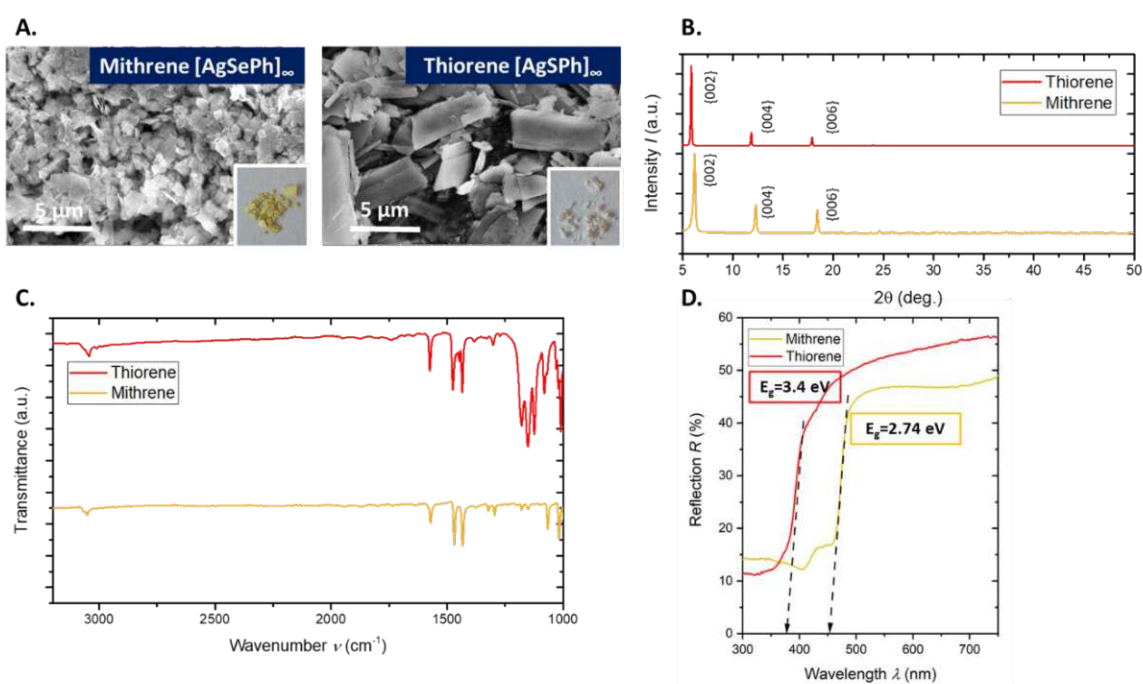


Figure 9. Characterization of the MOCHAs mithrene ($[AgSePh]_{\infty}$, orange line) and thiorene ($[AgSPh]_{\infty}$, red line) by means of **A.** SEM, **B.** XRD, **C.** ATR-FTIR and **D.** DRS measurements.

Element ratio

Information on the ratio of carbon, metal (silver) and chalcogenide (S, Se) to each other was performed to estimate the purity of present MOCHAs. Theoretical calculations were done, presuming a monomeric unit of MOCHA consisting of one silver atom, two chalcogenide atoms and two phenyl rings having each six carbon atoms and five hydrogen atoms. The repeating unit of MOCHAs is shown in **Figure 3** above in the introduction. EDX, TXRF and XPS techniques were not able to detect hydrogen, thus it was not considered in the theoretical calculations. EDX and XPS enable quantification of carbon, thus the theoretical values were calculated taking carbon into account, whereas TXRF can hardly detect carbon and so the theoretical atomic ratio was calculated excluding carbon. The values for the theoretical calculations and the obtained atomic ratios with the different techniques are summarized in **Table 4**.

Table 4. Theoretical and experimental values for metal, chalcogenide and carbon ratio obtained by EDX, XPS and TXRF techniques.

MOCHA	[AgSePh] _∞			[AgSPh] _∞		
Element	Carbon	Metal	Chalcogenide	Carbon	Metal	Chalcogenide
Theoretical values (including C) (at%)	80.0	6.7	13.3	80.0	6.7	13.3
Exp. values by EDX (at%)	92.4	2.5	5.0	91.2	4.6	4.2
Exp. values by XPS (at%)	/	/	/	80.1	10.0	10.0
Theoretical values (excluding C) (at%)	/	33	66	/	33	66
Exp. values by TXRF (at%)	/	41	59	/	48	52

For both MOCHAs, EDX measurements reveal that carbon is the most abundant element. However, in EDX a value of 90 at% was reached, while theoretical calculations only expected 80 at% carbon. The ratio of metal to chalcogenide was almost 1 in case of [AgSPh]_∞ and 0.5 in [AgSePh]_∞. Schriber *et al.* reported a metal to chalcogenide ratio of 1:1 in their EDS measurements⁸⁷. They found that the amorphous, non-crystalline MOCP side product exhibited a metal to chalcogenide ratio of 2:1. The here presented MOCHAs do not show such a ratio, thus it can be concluded that no amorphous product is present. The metal to chalcogenide ratio however for mithrene is in accordance with theoretical values, the ratio for thiorene agrees with results from literature. This could be explained by deviations from theoretical estimation and inaccuracy in EDX measurements. Interestingly, the measured at% in both MOCHAs did not reach the calculated at% values. An explanation for this deviations could be a wrongful determination of C at%. As carbon tape is used in SEM / EDX measurements to connect the sample to the sample stage an excess of carbon might have been detected. This could cause a falsification of the measured atomic ratio for carbon and thus also influence the ratio obtained for the other components of interest.

XPS measurements were energy calibrated with carbon to 284.6 eV. After calibration the elemental ratio of carbon to silver and chalcogenide was determined. Cross sections of the elements at 1486.6 eV were utilized for atom% calculations. Mithrene XPS measurements did not result in acceptable results. Thiorene showed a C at% of 80.1 % which is in very good agreement with theoretical calculations. Silver and sulphur both were present with 10 at%. Consequently, chalcogenide values were a bit lowered whereas silver values altered compared to the calculated values.

TXRF measurements show difficulties in detecting chalcogenides. TXRF thus is not considered a suitable method for exact determination of atomic ratios in MOCHAs. Errors of 7-15% cannot be excluded.

Electrochemical characterization

LSV results from measurements performed under nitrogen and carbon dioxide atmosphere in darkness and upon 456 nm illumination are shown in **Figure 10**. The measurements were performed with a bare carbon paper electrode, an $[\text{AgSePh}]_{\infty} / \text{CP}$ and an $[\text{AgSPh}]_{\infty} / \text{CP}$ electrode. Current densities were calculated considering the geometric surface area of carbon paper being 2 cm^2 .

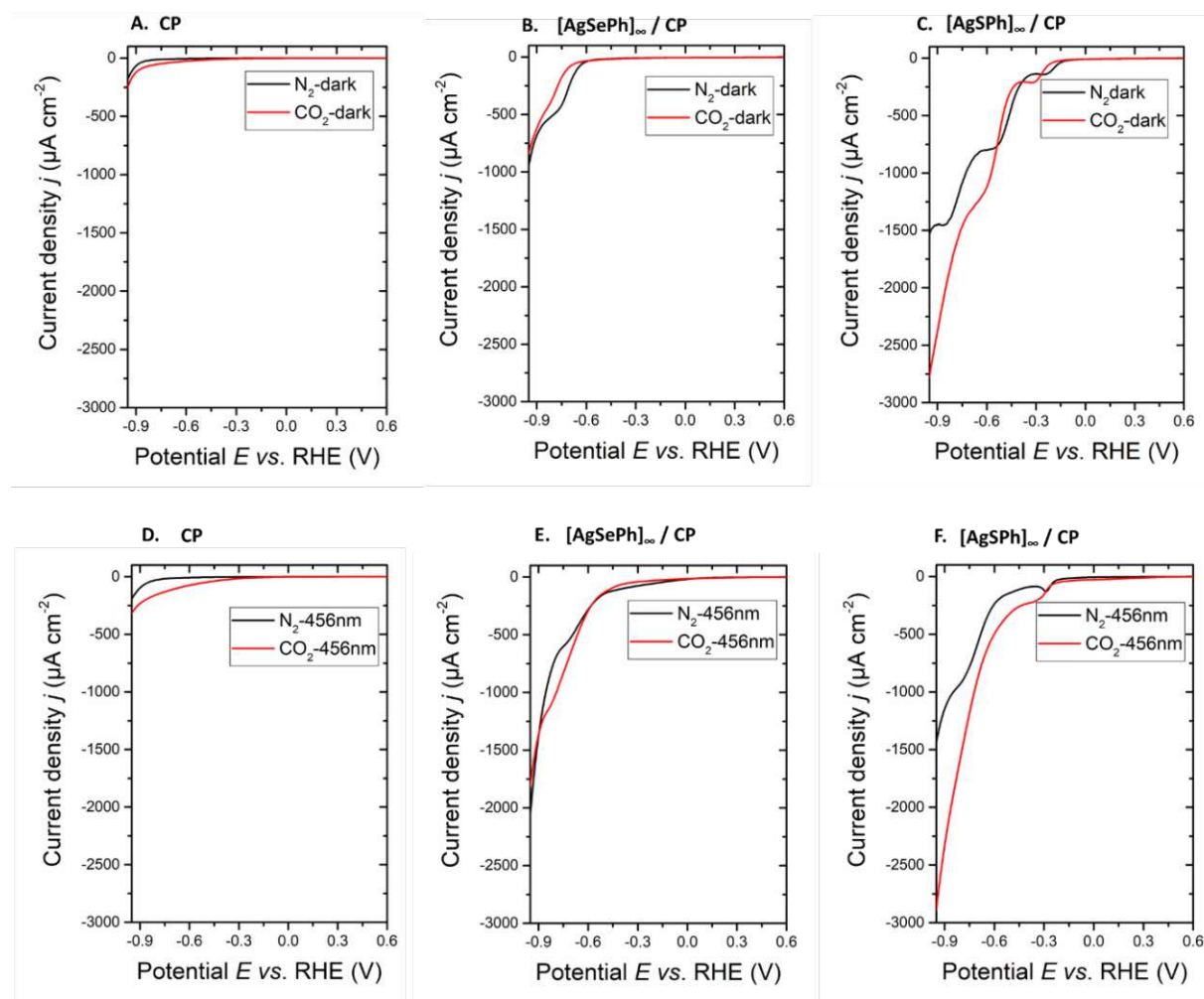


Figure 10. LSV measurements performed under nitrogen (black line) and carbon dioxide (red line) in darkness (A-C) and upon 456 nm illumination (D-F) with A,D. a bare CP electrode, B,E. a mithrene / CP electrode and C,F. a thiorene / CP electrode.

Comparison of the current densities of all three electrodes in darkness and upon light illumination reveal that with MOCHA / CP electrodes higher current densities can be reached. Mithrene lead to an enhancement of about 1 mA cm^{-2} whereas thiorene shown a current density higher about 2.5 mA cm^{-2} . The current densities under CO_2 atmosphere in darkness were higher, with the exception of the mithrene electrode, compared to current densities under nitrogen atmosphere. Also the onset potential was lowered when applying MOCHA / CP electrodes. Thiorene shown the lowest onset potential among all tested electrodes. The onset potential can be compared to an activation energy / barrier, which has to be overcome / input for a reaction to occur. Lowering the onset potential under CO_2 atmosphere consequently means a lowered activation energy toward CO_2 reduction and thus a facilitation for a reaction start.

Figure 11 presents results from photocurrent measurements at -0.3 V vs. RHE performed on mithrene deposited onto FTO. For current density calculation the geometrical surface area of FTO was determined to be 1 cm^2 .

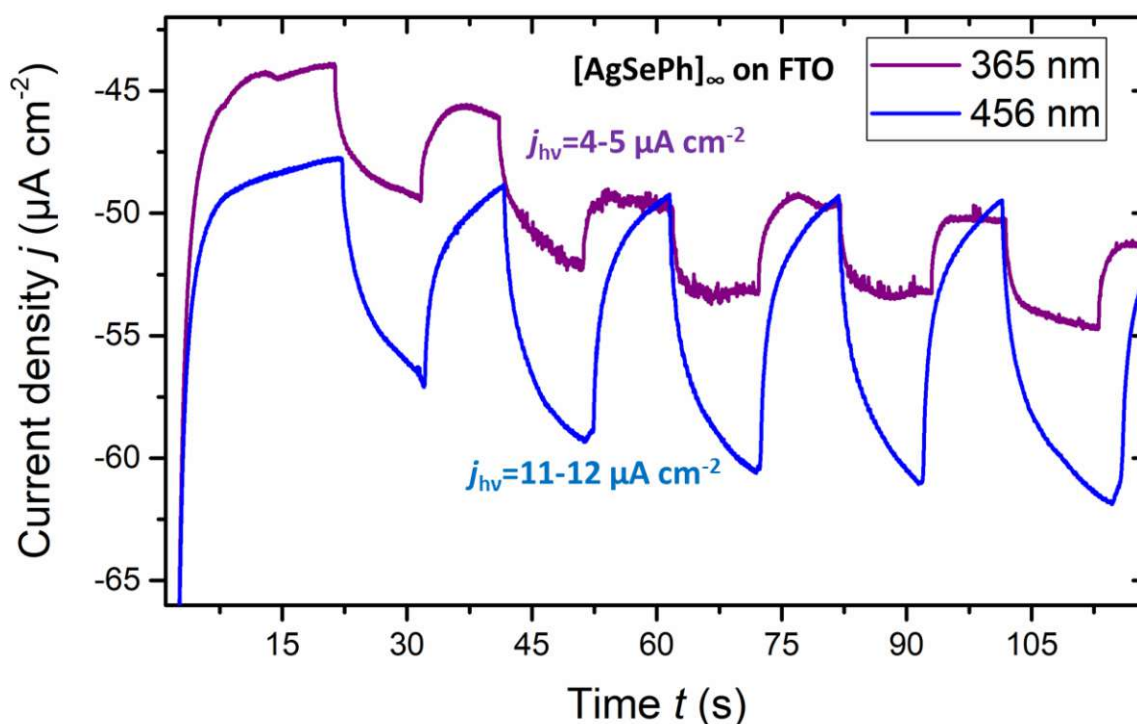


Figure 11. Photocurrent measurements performed with a mithrene / FTO electrode at 365 nm illumination (purple line) and 456 nm illumination (blue line).

Photoelectrochemical measurements of mithrene revealed, that $[\text{AgSePh}]_{\infty}$ works as a photocathode. When a barrier was placed between the light source and the cathode, a lower current was observed, than when light directly shone onto the electrode. The photoexperiment was performed at -0.3 V vs. RHE with at UV-light source (365 nm) and a visible light source, emitting blue light (456 nm). The measurements revealed that a higher photocurrent was observed when 456 nm light was used. Here a photocurrent of $11 \text{ } \mu\text{A cm}^{-2}$ was noted (at a potential of -0.3 V vs. RHE), while illumination with 365 nm UV-light only lead to a photocurrent of $4\text{-}5 \text{ } \mu\text{A cm}^{-2}$. This result lead to the decision of using 456 nm blue light for the photoelectrocatalytic CO_2RR .

9.2 (Photo)electrochemical Syngas production

The potential of the known MOCHA materials mithrene and thiorene for photoelectrocatalytic applications are assessed. Their capability of acting as (photo)electrocatalyst for CO₂ reduction to syngas is shown and discussed. First, a comparison between three different electrodes: carbon paper (CP), mithrene on CP ([AgSePh]_∞ / CP) and thiorene on CP ([AgSPh]_∞ / CP) is made. A closer look will be taken on the correlation between chosen potential and favoured H₂:CO ratio. Then, the impact of light illumination (456 nm) on electrolysis will be studied and thus the potential of MOCHAs as photoelectrocatalyst will be discussed. At the end of this chapter the relation between higher amount of silver nanoparticle on the MOCHA / CP electrode and the success towards CO₂ reduction will be shown.

*In the following sections two terms “lower” and “higher” potentials are used. These are referred to absolute values thus describing -0.6 V as low potential and -1.0 V as high potential.

9.2.1 Potential and electrode dependence

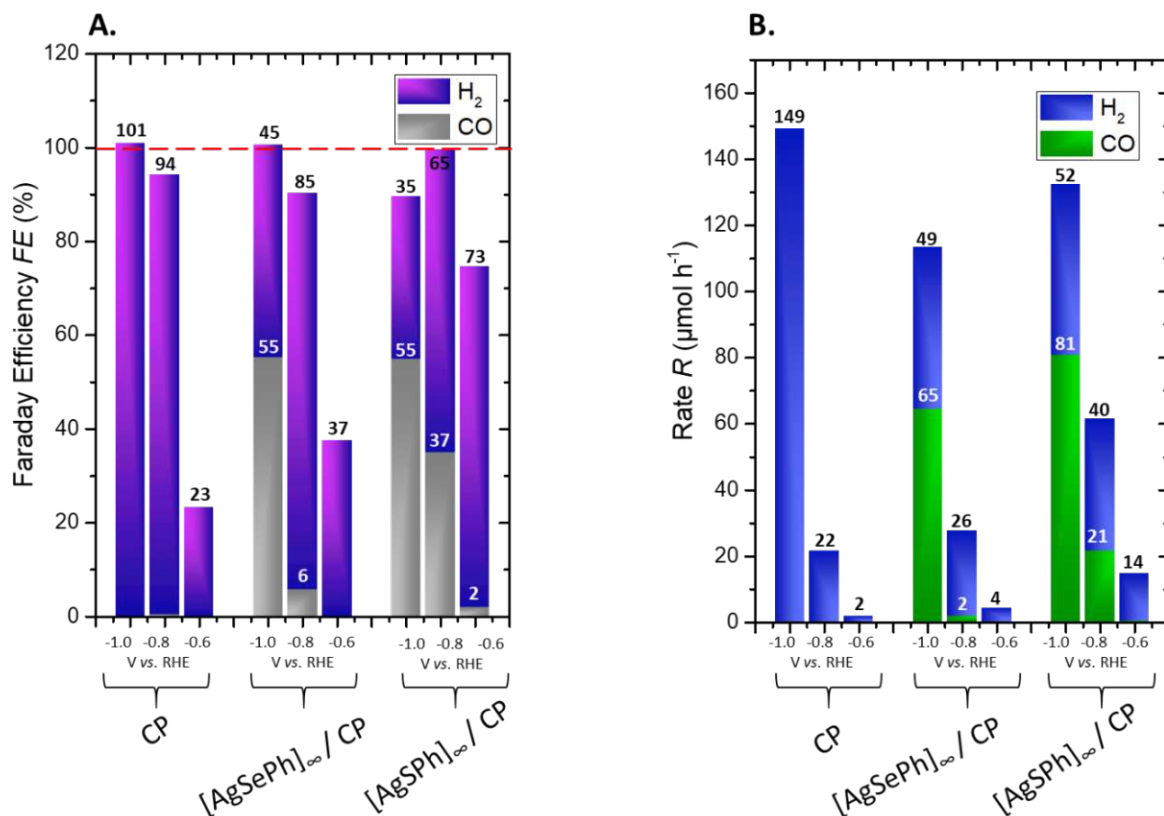


Figure 12. A. Faraday efficiencies for H₂ (purple) and CO (grey) production and their corresponding B. rates for H₂ (blue) and CO (green). Measurements were performed in darkness at three different overpotentials (-1.0, -0.8 and -0.6 V vs. RHE) with three different electrodes CP, [AgSePh]_∞ / CP and [AgSPh]_∞ / CP.

CO₂ reduction reaction to syngas was done electrochemically at a constant potential for a time period of 30 min. The chosen potentials were -1.0 V, -0.8 V and -0.6 V vs. RHE. The first important observation which can be made from the graphs in **Figure 12** is that the bare CP electrode resulted only in hydrogen as a product whereas MOCHA / CP electrodes led to syngas production. These results led to the first conclusion that silver containing MOCHAs

might serve as potential catalysts for CO₂RR. The ratio of H₂:CO however was strongly varying, depending on the applied potential and involved MOCHA. Both MOCHA / CP electrodes have a decreasing Faraday efficiency for carbon monoxide and an increasing Faraday efficiency for hydrogen with decreasing potential. The absolute rate of these products shows a distinct behaviour. The rates of CO and H₂ decrease both with decreasing potential. This seems to be expected as a lower potential (less energy help) results in less conversion of CO₂ to syngas and thus less $\mu\text{mol h}^{-1}$. The Faraday efficiency however clearly shows that high potentials (-1.0 V) favour the formation of CO compared to lower potentials (-0.8 V). At a potential of -0.6 V *vs.* RHE hardly any CO was formed and the only detected product was H₂. Taking a closer look at the Faraday efficiencies at the low potential of -0.6 V *vs.* RHE reveals that adding the FE of the products CO and H₂ up, does not lead to the necessary 100 %. A possible explanation would be the formation of other CO₂ reduction products such as methane, formic acid or methanol. This explanation is but unlikely as no methane was detected by gas chromatography and silver along with other noble metals is favouring the formation of CO⁴⁶. Further the total FE @-0.6 V *vs.* RHE obtained by bare CP, was far off from 100 %. This behaviour could be explained with the following hypothesis: although the solubility of H₂ and CO in aqueous solutions is rather low, a saturation of the electrolyte has to be reached prior to filling the gas phase. At low potentials eventually no oversaturation of the electrolyte was reached yet, thus resulting in a lower FE. At -1.0 V *vs.* RHE both MOCHA / CP electrodes shown a FE of 55 % for CO. Comparing the rates at this potential however revealed, that [AgSPh]_∞ / CP obtained a 16 $\mu\text{mol h}^{-1}$ higher rate (85 $\mu\text{mol h}^{-1}$) compared to [AgSePh]_∞ / CP (61 $\mu\text{mol h}^{-1}$). The ratio of H₂:CO was low, meaning a favoured CO production at -1.0 V *vs.* RHE for both MOCHA / CP electrodes. This observation changed drastically at lower potentials of -0.8 V *vs.* RHE. Mithrene reached a H₂:CO ratio of 20 (for FE and rate), clearly favouring the formation of hydrogen. The FE and rate ratio obtained with thiorene was lowered by a factor of 10 compared to mithrene. Consequently, a hydrogen to carbon monoxide ratio of 2 was reached, favouring still the formation of hydrogen over CO. The difference in CO rate between the mithrene and thiorene electrode at -0.8 V *vs.* RHE was 18 $\mu\text{mol h}^{-1}$. This result led to the conclusion that thiorene is a better catalyst for CO₂ reduction to CO. The improvement which can be made by choosing a thiorene over mithrene electrode is on average 17 $\mu\text{mol CO}$ per hour. The H₂ rate was comparable for mithrene and thiorene at -1.0 V *vs.* RHE but at -0.8 V *vs.* RHE a difference of 14 $\mu\text{mol h}^{-1}$ was seen. This deviation is comparable to the CO rate difference.

Comparison of the CO₂ reduction results between MOCHAs and silver chalcogenide (Ag₂S, Ag₂Se) compounds are made at this point. Chen *et al.* published a study with Ag₂S on carbonaceous electrode supports and reached FE_{CO} values up to 70% at -1.0 V *vs.* RHE⁸⁵. The competing thiorene electrode resulted only in a FE of 55 %. Ma *et al.* investigated CO₂ reduction by *monoclinic*-Ag₂Se and *orthorombic*-Ag₂Se. FE_{CO} with mithrene was higher by 15% than their reported value for *o*-Ag₂Se. However, as MOCHA crystallizes in a monoclinic space group, comparison to *m*-Ag₂Se would probably be more accurate. Their reported carbon monoxide FE reached 98 % at an overpotential of only -0.9 V *vs.* RHE⁵⁶. Mithrene on the other hand only reached a value of 55 % at -1.0 V *vs.* RHE. As it was shown by Ma *et al.* crystal phases and composition can have a great impact on product selectivity and catalytic

performance⁵⁶. Given the fact that MOCHA crystallinity and composition is clearly different from Ag₂S and Ag₂Se deviations of several percent are plausible. Although MOCHAs reached significantly lower FE_{co} values they can still be considered as a possible material for CO₂ reduction applications.

9.2.2 Effect of light

Electrocatalytic CO₂ reduction was also done upon light illumination with a 456 nm lamp. This wavelength was chosen based on the photocurrent measurements presented in section 8.4.3.2. The results of the photoelectrocatalytic measurement at the three chosen potentials (-1.0 V, -0.8 V and -0.6 V vs. RHE) with the three electrodes (bare CP, [AgSePh]_∞ / CP, [AgSPh]_∞ / CP) are presented in **Figure 13**.

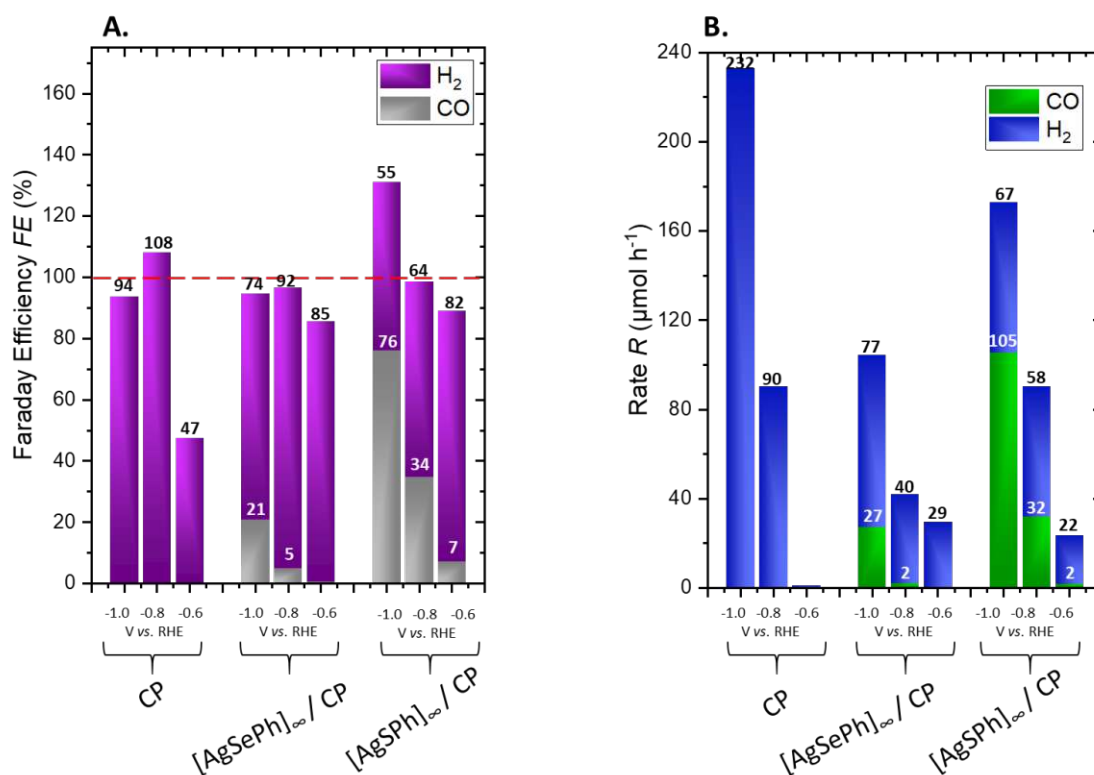


Figure 13. A. Faraday efficiencies for H₂ (purple) and CO (grey) production and their corresponding B. rates for H₂ (blue) and CO (green). Measurements were performed upon 456 nm illumination at three different overpotentials (-1.0, -0.8 and -0.6 V vs. RHE) with three different electrodes CP, [AgSePh]_∞ / CP and [AgSPh]_∞ / CP.

The bare CP electrode should not be photoactive and as also in the experiments without extra illumination no CO was produced. Interestingly, the hydrogen rate was increased by 70-80 μmol h⁻¹ compared to the electrocatalytic experiments in darkness (**Figure 12**). The Faraday efficiencies however were comparable to measurements performed in darkness. Deviations in rates might be a result of porosity and surface deviations. Here FE represent a more reliable comparison. The mthrene electrode reveals that the total Faraday efficiencies for CO and H₂ are close to 100 %. Light incidence did not cause the desired increase in CO efficiency and rate but in H₂. While the FE at -1.0 V vs. RHE for CO decreased by 23 %, the FE for H₂ was increased almost by 30 %. The difference becomes even more apparent when comparing the rates: CO rate dropped from 65 to 27 μmol h⁻¹ whereas H₂ rate increased from 49 to 77 μmol h⁻¹ upon light incidence. 456 nm blue light seems to cause a switch in H₂:CO ratio and thus changing the selectivity of MOCHA for CO₂ reduction products. A possible explanation for this behaviour could be the degradation of MOCHAs upon light and overpotential. Loss of MOCHA would correspond to less CO and more H₂ as bare CP would favour hydrogen production over CO. To rule this possibility out, stability test on MOCHAs upon light illumination and overpotential have been made. Their results

are summarized in 9.3. Finally, also the photoelectrocatalytic performance of $[AgSPh]_{\infty} / CP$ will be assessed. It can be seen clearly that the overall FE at -1.0 V vs. RHE reached a value above 100 %, namely 131 %. Although theory would predict a maximum overall FE% of 100%, deviations of a few percent are expected in experimental FE results. A deviation of 30 % however from the expected value, especially an increase are observed rarely. An increase in FE signifies that more product was produced than electrons were involved in the process. In an electrocatalytic process this is theoretically impossible. When thiorene however acts as a photocatalyst the high FE could be explained. As product would be formed not as a result of only electrons but also photons. Faraday efficiency but does only take electrons into account. According to this theory, the high overpotential was needed to provide enough energy for the reaction to happen (to come across the activation energy). The incoming photons provide then the rest of the energy needed for the reduction of CO_2 . The explanation why mithrene does not act as a photoelectrocatalyst but thiorene does could be explained by the observation made by Schriber *et al.*¹⁰⁶. It was found that thiorene is an indirect bandgap semiconductor which is known to be beneficial for photocatalysis as charge recombination is less likely to occur. In mithrene, a direct semiconductor, eventual charge recombination happens rather quick, making it not beneficial as a photocatalyst. Another hypothesis for the photoactivity of thiorene is that overpotential and illumination causes a degradation of MOCHA to Ag-NP. This would explain the high selectivity towards CO and the photoactivity of thiorene, which would be actual photoactivity of silver nanoparticles. Ag-NP are known to be photoactive materials due to a surface plasmonic resonance effect¹¹⁷. The rate increased for both products CO and H_2 . CO rate was increased by $24\ \mu\text{mol h}^{-1}$, the H_2 rate by $15\ \mu\text{mol h}^{-1}$. Even at lower potentials an increase in CO and H_2 rate was observed. Namely at -0.8 V vs. RHE an increase of $11\ \mu\text{mol h}^{-1}$ for CO and $18\ \mu\text{mol h}^{-1}$ for hydrogen was seen. A minor gain in CO/ H_2 rate was also visible at -0.6 V vs. RHE . To this date, yet no explanation for this increased rate can be given.

9.2.3 Effect of silver nanoparticles

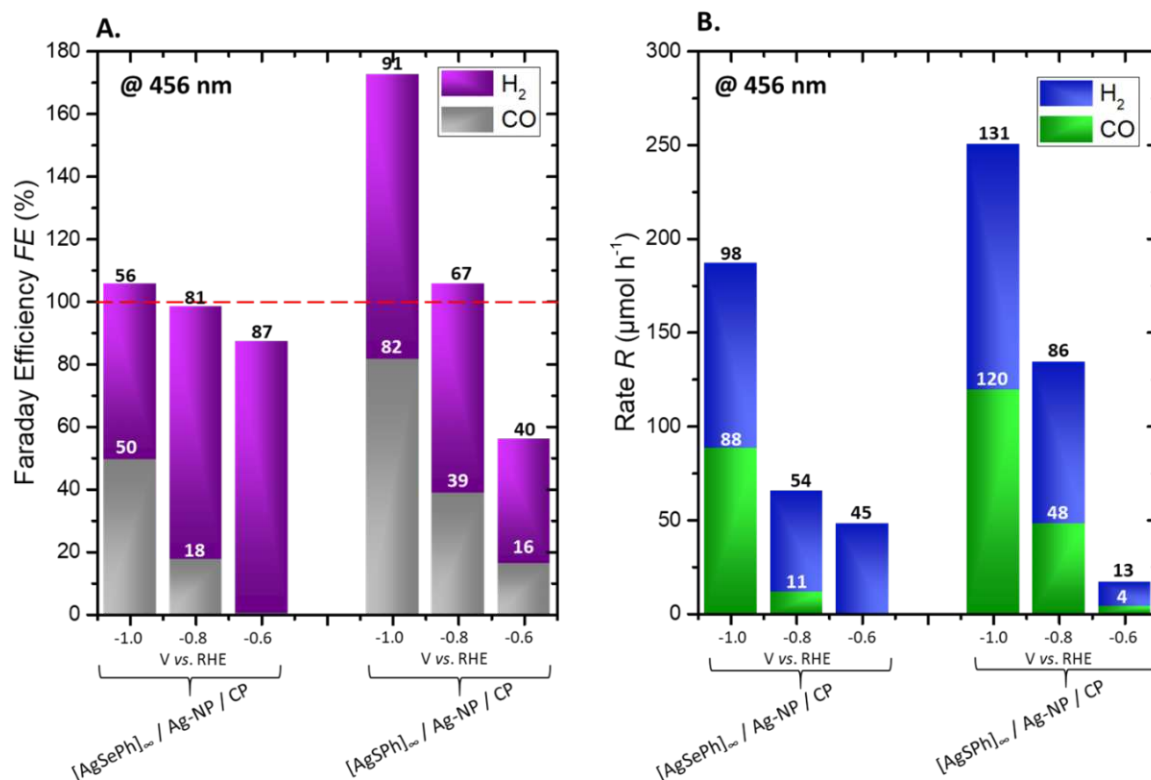


Figure 14. Effect of silver nanoparticle deposition onto MOCHA / CP electrodes is shown. **A.** Faraday efficiencies for H₂ (purple) and CO (grey) production and their corresponding **B.** rates for H₂ (blue) and CO (green). Measurements were performed upon 456 nm illumination at three different overpotentials (-1.0, -0.8 and -0.6 V vs. RHE) with two different electrodes [AgSePh]_∞ / Ag-NP / CP and [AgSPh]_∞ / Ag-NP / CP.

To test the hypothesis that MOCHAs might turn into silver nanoparticles, especially in the case of thiorene, an intentional silver nanoparticle deposition was done by photoreduction which is why Ag-NP deposition was not performed on bare CP but only on MOCHA / CP electrodes. In darkness Ag-NP deposition on mithrene did neither lead to an increase in FE nor in rate. Silver nanoparticle deposition on the thiorene electrode brought a slight increase in FE for CO and thus a decrease in the H₂:CO ratio, especially for lower potentials (-0.8 V, -0.6 V). The overall FE at those potentials however also was clearly above 100 % which cannot be explained easily. Upon light illumination Ag-NP had a positive effect towards syngas production with both, mithrene and thiorene, electrodes. With silver deposited onto mithrene electrodes, an enhancement of CO Faraday efficiency was reached. The FE_{CO} was doubled (for -1.0 V vs. RHE) and almost tripled (for -0.8 V vs. RHE) (compared to [AgSePh]_∞ / CP@456 nm), leading to a decrease in H₂:CO ratio. Also, the CO rate was the increased compared to only mithrene on CP @456 nm (+60 μmol h⁻¹) and without light illumination (+20 μmol h⁻¹). Ag-NP deposited onto thiorene / CP electrodes shown overall FE of clearly above 100 %. This could be an indication for a high photoactivity as more products were produced than electrons were used. The FE and rate for CO remained similar as with the [AgSPh]_∞ / CP electrode upon light illumination but the FE and rate for H₂ were clearly increased. Thus, the carbon monoxide to hydrogen ratio was decreased and in favour of hydrogen not only at low potentials but also at -1.0 V vs. RHE. Consequently, it can be told that Ag-NP deposition did not lead to a relevant, influential improvement of the CO₂

reduction capability. Lowering the overpotential for the CO₂ reduction to occur was not reached by Ag–NP deposition. The H₂:CO ratio was not improved in favour of CO in case of the thiorene electrode. Ag–NP on the mithrene electrode led to a slight but non-significant improvement of carbon monoxide to hydrogen ratio. Ag–NPs are reported to act as CO₂ reduction photoelectrocatalysts on their own, and show a remarkable performance of 85 % FE_{CO} for 5 nm particles on carbonaceous support¹¹⁸. The results of the experiments done in the here presented work suggest that the use of Ag–NP as co-catalysts in connection with MOCHAs for CO₂ reduction is therefore not recommended.

9.3 Stability of MOCHAs

The following chapter places its focus on the stability of MOCHAs under various conditions (pH, solvents, temperature and illumination). Further a closer look was taken at their stability upon electrolysis. MOCHA stability was confirmed by means of SEM and powder XRD measurements.

9.3.1 Organic solvent, pH and temperature

Stability of [AgSePh]_∞ deposited onto a Si single crystal in various solvents (EtAc, MeOH, IPA, DMF) for one week at room temperature is shown in **Figure 15**.

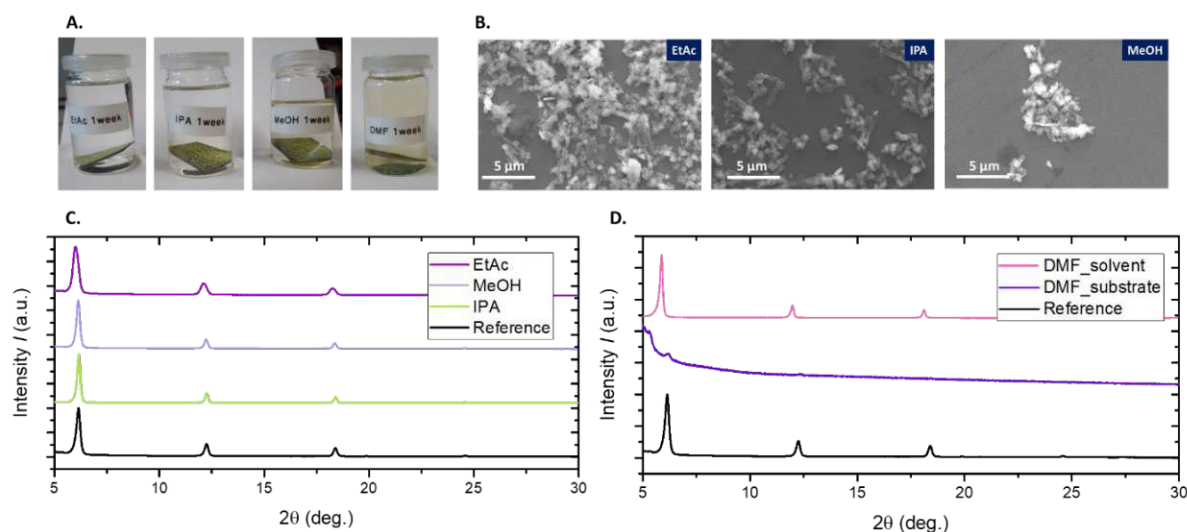


Figure 15. Stability test results performed on mithrene in various organic solvent stored at room temperature for one week. **A.** images of mithrene on a Si-substrate in (from left to right) EtAc, IPA, MeOH and DMF. **B.** SEM images of mithrene after exposure to the organic solvent EtAc, IPA and MeOH (from left to right). **C.** XRD patterns of a mithrene reference (black line) and of mithrene exposed to IPA (green line), MeOH (blue line) and EtAc (purple line). **D.** XRD patterns of a mithrene reference sample (black line), the Si-substrate after DMF exposure (purple line) and a sample taken from the DMF / mithrene suspension (pink line).

The SEM images in **Figure 15 B.** as also the XRD patterns in **Figure 15 C.** confirmed the stability of MOCHA in the solvent ethyl acetate, methanol and isopropanol. In DMF a distinct observation was made. The XRD pattern of the Si-holder did not show remaining MOCHA material (D, purple line). It was visible that the yellow powder was suspended in DMF (A- 4) and the XRD pattern of the suspension after DMF removal shown the characteristic MOCHA peaks. These results lead to the conclusion that DMF caused unlike other solvents desorption of MOCHA from the Si single crystal. [AgSePh]_∞ was suspended in DMF, however no structural changes or damages to the MOCHA were caused by DMF. Stability

measurement results in various pH media and over a wide temperature range are shown in the appendix in **Figure 20** and **Figure 21**.

The appearance of MOCHAs and their characteristic XRD patterns did not change upon pH ranging from 0 to 9 (see **Figure 20** in the appendix). From that observation the conclusion is drawn that MOCHAs are stable upon a wide pH range from acidic to alkaline pH values.

Silver benzeneselenolate MOCHA powder stored at temperatures from -25°C up to 120°C for one week neither did change appearance nor shown structural changes as can be seen in **Figure 21** in the appendix. These results are in good agreement with a previous study, confirming the stability of MOCHAs until a temperature of 200°C . Beyond 200°C a mass loss of 59.1 % was observed in TGA measurements⁸⁹. This mass loss is related to the dissociation of MOCHA releasing benzeneselenolate ligand. It was noted that the ongoing mechanism is most likely a redox mechanism and can be reversed as shown by the tarnishing approach.

9.3.2 Illumination

Illumination stability test were carried out up to 72 h under visible light, UV light (365 nm) and VIS-456 nm light. Their results are summarized in **Figure 16** (456 nm) and in the appendix in **Figure 22** (365 nm) and **Figure 23** (simulated solar light).

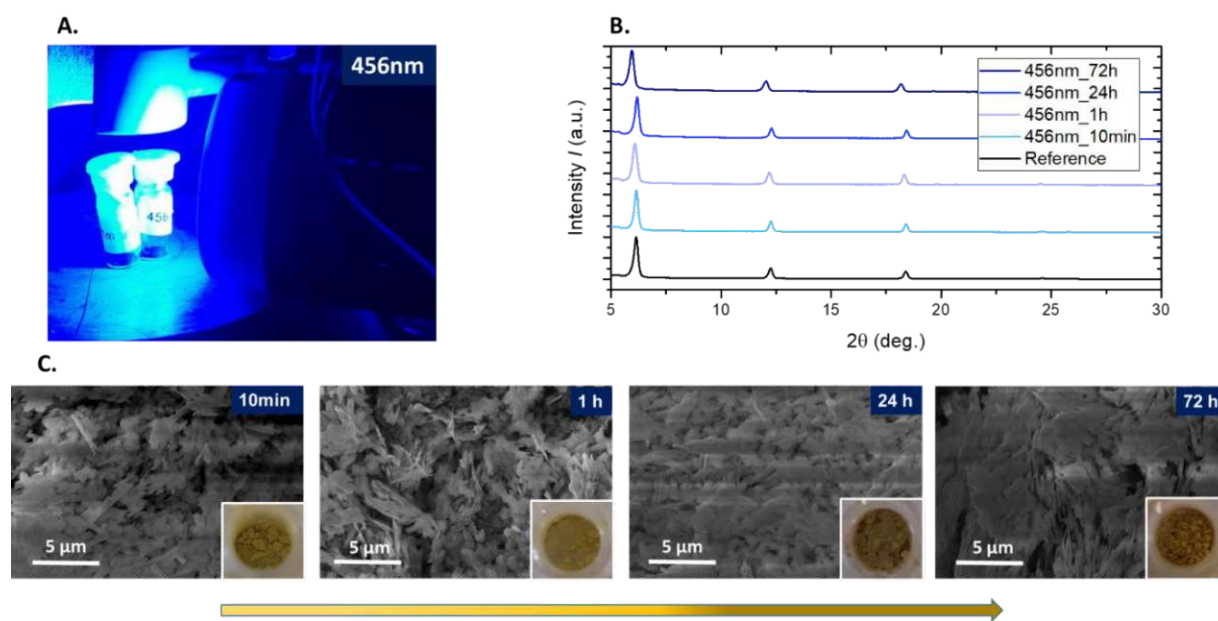


Figure 16. Results of light illumination (456 nm) stability testing. **A.** image of the testing setup. **B.** XRD patterns of a mithrene reference (black line) and mithrene samples being exposed for 10 min (blue-green line), 1h (bright blue line), 24h (blue line) and 72 (dark blue line). **C.** SEM images and pictures (lower right corner) of mithrene being exposed 10 min, 1h, 24h and 72h (from left to right) to 456 nm illumination.

Upon 456 nm illumination MOCHAs kept their characteristic SEM images (**Figure 16 C**) showing monoclinic, layered platelets. The XRD pattern (**Figure 16 B**) was equal to the reference pattern with one exception: after 24 h illumination a slight shift to higher angles was observed. This can be explained due to differences in the interlayer spacings. As XRD pattern are reflecting the reciprocal space, shifts to higher angles of the refraction along the z-axis correspond to lower distance between the layers. Especially in the graphite

community left and right shifts of the {00Z} peaks indicate a deviation in spacing between layers¹¹⁹. MOCHA as a 2D layered material can be treated similar to graphite. Eventually the MOCHA samples used for 24 h experiments display a smaller interlayer spacing. This could be due to impurities caused during synthesis. Another reason could be that after 24 h a change in structure (interlayer spacing reduced) occurs.

Upon UV illumination (365 nm) (see **Figure 22** in the appendix) a similar observation was made. No differences in the SEM images could be seen and the XRD pattern of all tested durations shown the three characteristic peaks corresponding to the {002}, {004} and {006} planes respectively. However, as also upon 456 nm illumination a shift to higher angles in the XRD pattern of the MOCHA sample after 24 h illumination time was observed. Interestingly in both samples no shift to higher angles after even longer illumination (72 h) could be seen.

Illumination with visible, simulated solar light did neither lead to changes in the SEM images nor in the XRD patterns. Even after 24 h illumination no shift in the XRD pattern was visible (see **Figure 23** in the appendix).

Under all tested illumination conditions, a colour change of the [AgSePh]_∞ MOCHA from bright yellow to dark yellow / brownish was seen with increasing illumination time. This change in colour was present still months after the performed experiments. As however no relevant differences were noted in the SEM and XRD results the colour change proved to do not have an impact on these key characteristics. It was found that visible light causes oxidation of polyconjugated structures such a polyphene sulphide at the surface. This observation is thermally irreversible and did not show an impact on other physiomechanical or electrical properties¹²⁰. It is likely that the colour change in MOCHAs which consist of a polymeric network of chalcogenides and phenyl rings similar to polyphene sulphide composites occurred due to oxidation, which caused a change in yellowness but not lightness¹²⁰. Popple *et al.* further confirmed that the characteristic blue emission of mithrene was independent from crystal aspect ratio or the lateral size of the crystals. A dependence was noted between emission intensity and the crystal thickness and number of layers. The emission was the same over all morphologies and only highly distorted, defective crystals shown a slight red shift in emissive behaviour⁸⁹.

9.3.3 After electrolysis

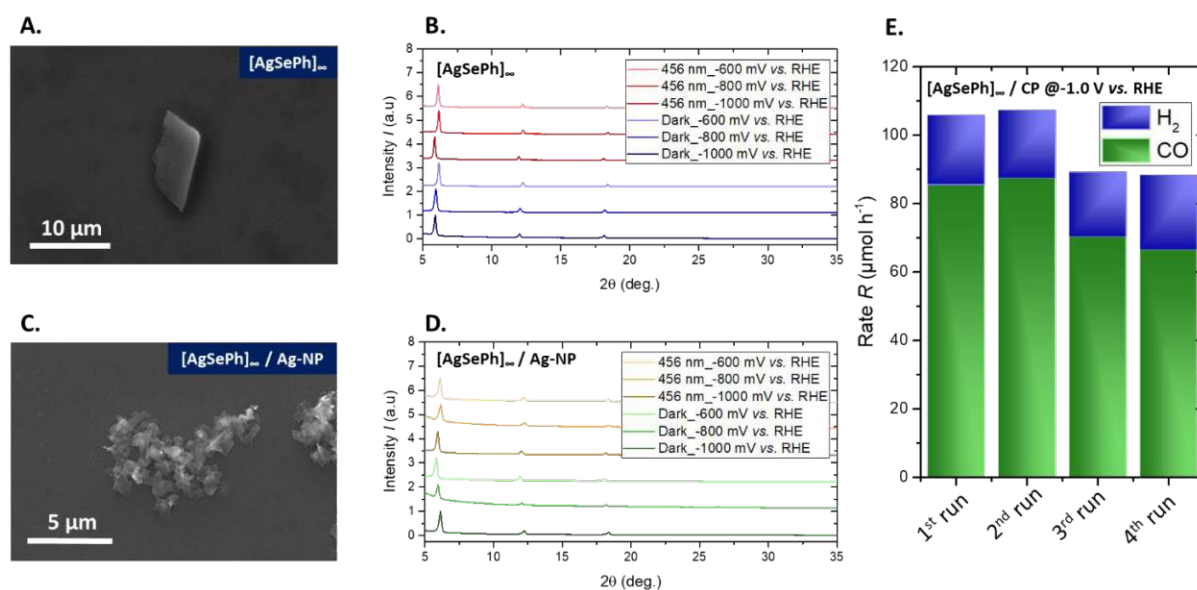


Figure 17. Stability test results upon electrolysis. **A.** SEM images of mithrene after electrolysis. **B.** XRD pattern of mithrene after electrolysis under all tested conditions. **C.** SEM images of mithrene + Ag-NP deposition after electrolysis. **D.** XRD patterns of mithrene + Ag-NP after electrolysis under all tested conditions. **E.** Rate of H₂ (blue) and CO (green) after electrolysis at -1.0 V vs. RHE in darkness after using the same [AgSePh]_∞ / CP electrode four times.

As mentioned already in chapter 9.2.1 the stability of mithrene upon electrolysis had to be checked. Therefore, the carbon paper part which was immersed into the electrolyte was cut and sonicated in 2 mL isopropanol for 15 min. In this way mithrene was sonicated off the CP substrate. The IPA with the suspended MOCHA in it was investigated by SEM and XRD measurements. SEM images in **Figure 17 A.** and **C.** reveal that [AgSePh]_∞ / CP and [AgSePh]_∞ / Ag-NP / CP were stable and present on the CP substrate after electrolysis. These results were confirmed also by XRD (see patterns in **Figure 17**). The stability upon electrolysis was tested by another experiment as well. Therefore, the same [AgSePh]_∞ / CP working electrode was used for four electrolysis consecutively. All four electrolysis were performed without light illumination and at -1.0 V vs. RHE in a CO₂ saturated environment. As it can be seen in **Figure 17 E.** above the CO rate remained between 85-68 μmol h⁻¹. If mithrene had been destroyed or desorbed from the electrode substrate a sudden drop in the CO rate would be expected. The H₂:CO ratio remained constant. Absence of mithrene would most likely have caused an increase in the H₂:CO ratio, as the rate of produced hydrogen would have increased drastically. From this observation it can be concluded that mithrene is stable upon potentials up to -1.0 V vs. RHE.

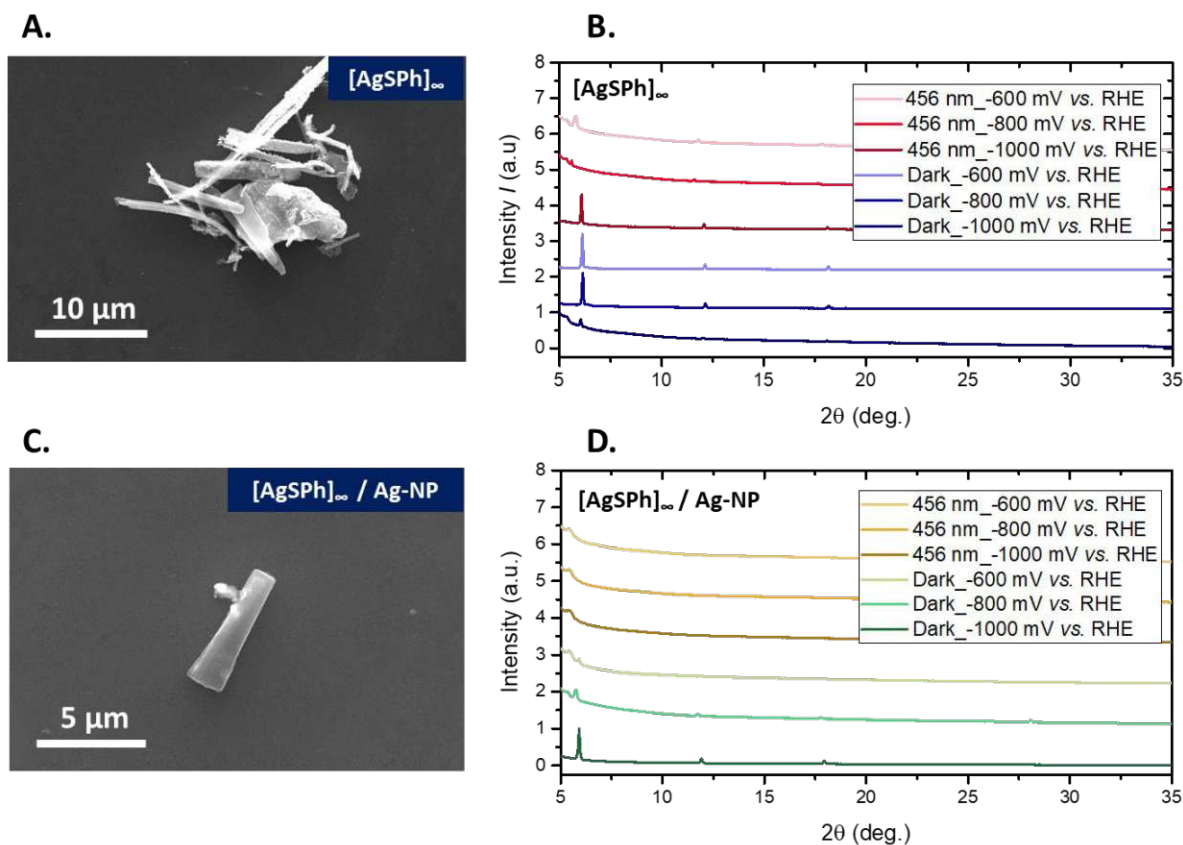


Figure 18. Stability test results upon electrolysis. **A.** SEM images of thiorene after electrolysis. **B.** XRD patterns of thiorene after electrolysis under all tested conditions. **C.** SEM images of thiorene + Ag-NP deposition after electrolysis. **D.** XRD pattern of thiorene + Ag-NP deposit after electrolysis under all tested conditions.

The stability of thiorene was investigated in the same way as with mithrene. SEM images do show remain of thiorene on the CP electrode (**Figure 18 A.**). The structure and shape of the thiorene crystals however, does not appear that perfect anymore. XRD pattern of thiorene after electrolysis shown the characteristic peaks, however with a strongly decreased intensity (**Figure 18 B.**). XRD pattern of the $[AgSPh]_{\infty}/Ag-NP$ / CP electrode upon light illumination do not show the expected peaks (**Figure 18 D.**). Thiorene upon electrolysis might be less stable than mithrene. The impact of light illumination onto the thiorene electrode was definitely stronger than on mithrene and eventually caused Ag-NP deposition, an unwanted side reaction which lead to the destruction of thiorene upon electrolysis.

9.4 New MOCHAs

The microwave synthesis was used to prepare new MOCHA combinations. The metals copper, nickel and iron were combined with the chalcogenides sulphur and selenium. The detailed synthesis conditions are reported in **Table 6** in the appendix. The synthesis using $Ni(NO_3)_2 \cdot 6H_2O$ and DPDS did not give a satisfactory yield. The other five combinations of $FeNO_3 \cdot 9H_2O$ and DPDS, $NiNO_3 \cdot 6H_2O$ and DPDS, $CuNO_3 \cdot 3H_2O$ and DPDS, $FeNO_3 \cdot 9H_2O$ and DPDS and $CuNO_3 \cdot 3H_2O$ and DPDS, aiming for the production of desired $[FeSePh]_{\infty}$, $[NiSePh]_{\infty}$, $[CuSePh]_{\infty}$, $[FeSPh]_{\infty}$ and $[CuSPh]_{\infty}$ led to colourful powders. The SEM images and pictures of the powders can be seen in **Figure 19 A.** Further the powders were characterized by means of ATR-FTIR measurements (**Figure 19 B.**) and XRD (**Figure 19 C.**).

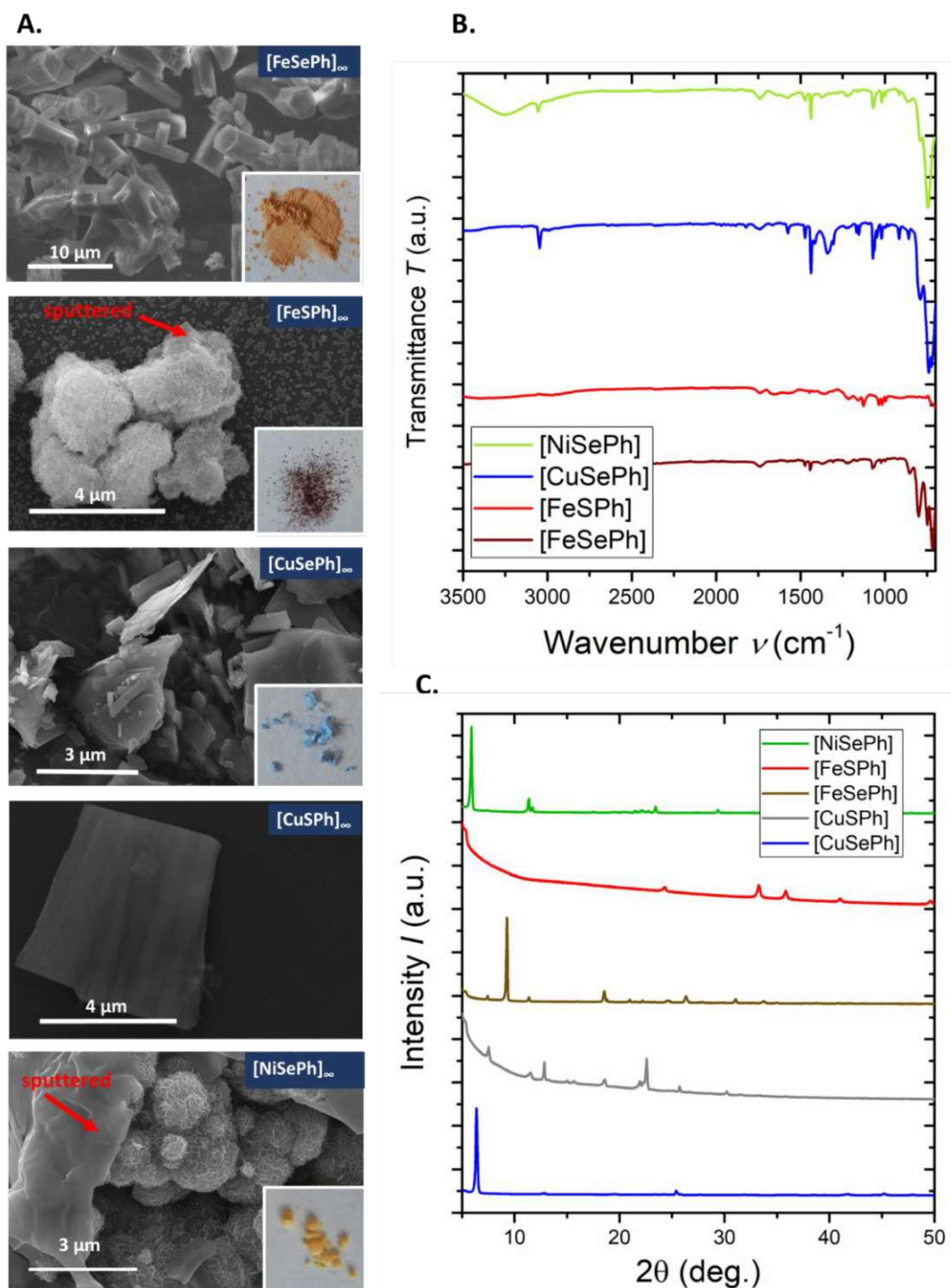


Figure 19 A. SEM images and images of the new prepared “MOCHAs”. B. ATR-FTIR spectra and C. XRD pattern of the “MOCHAs” [NiSePh]_∞ (green line), [CuSePh]_∞ (blue line), [CuSPh]_∞ (grey line), [FeSPh]_∞ (red line) and [FeSePh]_∞ (brown line).

The SEM image of [FeSePh]_∞ shows hexagonal structured cylinders. [FeSPh]_∞ and [NiSePh]_∞ resulted in flunky coral like structure. Both samples required additional sputtering to provide enough electrons for a well-resolved image. The sputtered components are indicated with red arrows. The two copper MOCHA ([CuSePh]_∞ and [CuSPh]_∞) showed a platelet structure similar to mithrene and thiorene. From the SEM images especially the [FeSePh]_∞ and copper-MOCHA looked promising to turn out as actual MOCHA structure.

XRD patterns of the prepared MOCHAs should display the characteristic peaks coming from interlayered spacings. It can be seen in **Figure 19** above that $[\text{CuSPh}]_{\infty}$ (grey line) and $[\text{FeSPh}]_{\infty}$ (red line) appeared to be rather inorganic in nature. In this case, most likely no MOCHA formation took place. Also the ATR-FTIR spectrum of $[\text{FeSPh}]_{\infty}$ (red line) confirmed this assumption, as none of the characteristic bands attributed to the phenyl ring was observed. ATR-FTIR measurements of $[\text{CuSPh}]_{\infty}$ were not possible as too little yield was achieved. $[\text{NiSePh}]_{\infty}$ and $[\text{CuSePh}]_{\infty}$ exhibited both the prominent {002} diffraction peak and also their ATR-FTIR spectra present the typical bands observed in MOCHA structures (see chapter 9.1.4). $[\text{FeSePh}]_{\infty}$ (orange line) showed interlayer diffraction peaks ({004}) and displayed the prominent MOCHA bands in its FTIR spectrum as well. Taking SEM, XRD and ATR-FTIR measurements into account it was concluded that $[\text{FeSePh}]_{\infty}$, $[\text{NiSePh}]_{\infty}$ and $[\text{CuSePh}]_{\infty}$ are indeed present as MOCHAs thus further characterization was done on these samples. **Table 5** shows the results of TXRF and XPS measurements performed with these compounds.

Table 5. Theoretical and experimental element ratio obtained by XPS and TXRF measurements.

MOCHA	$[\text{FeSePh}]_{\infty}$			$[\text{NiSePh}]_{\infty}$			$[\text{CuSePh}]_{\infty}$		
Element	C	Metal	Chal.	C	Metal	Chal.	C	Metal	Chal.
Theoretical values (including C) (at%)	80.0	6.7	13.3	80.0	6.7	13.3	80.0	6.7	13.3
Exp. values by XPS (at%)	78	4	17	60	Not detectable	40	81	2	17
Theoretical values (excluding C) (at%)	/	33	66	/	33	66	/	33	66
Exp. values by TXRF (at%)	/	28	72	/	40	60	/	40	60

XPS measurements did not show distinct peaks for nickel thus the elemental ratio of $[\text{NiSePh}]_{\infty}$ is in good agreement with theoretical calculations. Further both $[\text{FeSePh}]_{\infty}$ and $[\text{CuSePh}]_{\infty}$ showed 17 at% selenide. This value is approximately 4 at% above the theoretical value. Consequently, the atomic percentage of the metals is lowered in both samples.

TXRF measurements achieve values close to those predicted by theoretical calculations. $[\text{NiSePh}]_{\infty}$ and $[\text{CuSePh}]_{\infty}$ both show a 7% too high metal content whereas their chalcogenide content was reduced by 6at%. In $[\text{FeSePh}]_{\infty}$ the reversed behaviour was observed, here the metal content was reduced by 5at% and the chalcogenide content increased by 6%. Deviations in this range however can be accepted and can be assigned to measurement uncertainties.

As all the presented methods above did still not lead to a clarification on the structural composition of the prepared samples, single crystal diffraction measurements are necessary. Unfortunately, the obtained crystals were too small to be used for SCXRD measurements. Yeung *et al.* reported the structure of $[\text{CuSePh}]_{\infty}$ ¹⁰¹. According to the SEM image, $[\text{NiSePh}]_{\infty}$ was not stable enough to withstand a XFEL pulse thus only $[\text{FeSePh}]_{\infty}$ was sent to DESY (german electron synchrotron) for structural clarification. To this date the results have not yet arrived which is why the structure clarification of $[\text{FeSePh}]_{\infty}$ cannot be presented here.

10 Conclusion and Outlook

In this work, a simple and new method for the preparation of MOCHAs was designed and presented. The microwave synthesis route has the great advantage of being in bulk thus not having the limitation of an interface and consequently enabling higher yields. Its simplicity makes possible the development of new MOCHAs. Here, however the challenge of structure determination arises. It is rather costly and tedious to get a synchrotron assignment so a simpler way for getting single crystals by different crystallisation techniques is needed. Eventually a combination of microwave synthesis with the approach used by Tisdale *et al.* could lead to larger crystals, suitable for SCXRD, in future⁹¹. In this way unambiguous structure determination could be done by single crystal X-ray diffraction analysis, which is routine and thus an easier accessible method. This would open the path to explore and enlarge the variety of different MOCHA materials. Due to their inorganic-organic hybrid character an infinite number of combinations could be thought of, changing the involved metal, chalcogenide and organic ligand.

The potential application of mithrene and thiorene as CO₂ reduction (photo)electrocatalysts was tested for the first time. Both MOCHAs enable CO₂ reduction at potentials of -0.8 V *vs.* RHE and -1.0 V *vs.* RHE. Pure electrocatalysis shown a higher selectivity for CO₂ reduction than for the competing process HER. Thus, a H₂:CO ratio in favour of carbon monoxide was received. Thiorene shown a higher selectivity towards CO compared to mithrene under all tested conditions. Upon light illumination the H₂:CO ratio was improved in case of thiorene for CO and increased in case of mithrene. An explanation for this behaviour is hard to give at current state. Mithrene was reported to have delocalized electrons due to its trigonal silver bonds. Thiorene on the other hand is not expected to have delocalized electrons above and below the argentophilic network due to its linear arrangement^{102,106}. However, photocurrent measurements performed also in this work confirmed a higher photoactivity for thiorene compared to mithrene. Ag-NP photodeposition did not lead to a significant improvement in any case. Future experiments could focus on the reproducibility of the CO₂ reduction performance of MOCHAs. The experiments in this work have each been done by a minimum of two to three times but still repetition in another laboratory or by another person would be needed for scientific accuracy. Further the mechanism of both the electrocatalytic and the photoelectrocatalytic CO₂ reduction remains unclear to this date. In situ ATR-FTIR and XPS measurements could be of great help to get insight into the occurring mechanism and its rate limiting steps. Another point of interest is the investigation of photocatalytic HER performance of MOCHAs. Their optoelectronic properties and the results obtained in this thesis at low reduction potentials would suggest photocatalytic hydrogen evolution to be achievable with these materials.

The great stability of MOCHAs makes them a promising and trustworthy material for “real life” applications. Their temperature stability up to 200 °C enable their application in most electronic devices. For metallurgical, industrial processes MOCHAs are most likely not the material of choice as temperatures in these processes often lie above 200 °C. Their stability over a wide pH range, make them possible candidates for applications in aqueous environment and it was shown in this work, that they are also stable in various organic solvents for a prolonged time. The impact of light illumination on their optoelectronic

properties cannot be determined with certainty. Ivanov *et al.* suggest no change in properties (for a similar materials class), whereas this work did demonstrate a potential damage in the CO₂ reduction performance of thiorene upon light illumination and in darkness and a change in appearance¹²⁰. However, mithrene shown a high stability upon electrolysis in darkness and upon illumination over all tested potentials.

Prior to suggesting MOCHAs in medical and environmental applications a toxicity assessment of MOCHAs should be made. The risk and hazard of MOCHAs depend on the interaction of the involved metal, chalcogenide and organic ligand and is therefore a very complex system and hard is to predict. Nonetheless, the fact that they exhibit a polymeric network, do not smell and are neither hydrophilic nor lipophilic minimalizes the risk for hazardous properties. Still problems similar to microplastics might appear in future when using MOCHAs in excess and not taking care of proper disposal.

11 Acknowledgement

First and foremost I would like to express my gratitude to Prof. Dominik Eder. Giving me the chance to work, learn, research and experiment in his group has been a great pleasure and honour to me. His many ideas and fruitful discussions have been a great inspiration for this work. I will always remember his concern for every group member and interest in our research topics.

Special thanks I want to give to Dr. Doğukan Hazar Apaydin who introduced me to the exciting field of MOCHAs and CO₂ reduction. Thanks for always having an open ear for my questions, concerns and suggestions. Letting me freedom in my research but also guiding me through all the thesis was a balance act which you managed great. I am very lucky to have you as a supervisor!

Thanks to the Eder Research group for the great working environment and also the really welcoming and open atmosphere within the group. I am very grateful to all of you, for solving problems together as a team, helping and supporting me, whenever I approached you with a problem and of course also the fun and good times we had in and outside the lab. Especially I would like to thank Pablo Ayala, Jakob Blaschke, Bernhard Fickl, Stephen Myakala and Jakob Rath for your assistance in conducting SEM, TXRF and XPS measurements for me. Thanks also to Werner Artner for introduction and help with XRD measurements whenever needed and Thomas Wicht for explaining me the magic of XPS analysis.

Finally it's the time to give my family a big thank you especially my parents Silke and Hans. Thanks for always believing in me and supporting me in my dreams to become true. I am aware that it has not been always easy for you to understand and accept my choices but I am very grateful that you let me experience life, including all the stupid mistakes I might had to make and love me for who I am. Thanks to my grandparents. I really appreciate talking and spending time with you. It always feels like "coming home" being close to you. My two "little" brothers Philipp and Dominik. I am so lucky to have you. You were and are a big inspiration and motivation to me.

Dziękuję to my caring and loving Mariusz. You filled the last years with joy and made them the most amazing time of my life. Thanks for always reminding me of the important things in life whenever I needed it the most.

12 References

- (1) Raju, E.; Boyd, E.; Otto, F. Stop Blaming the Climate for Disasters. *Commun. Earth Environ.* **2022**, 3 (1), 1. <https://doi.org/10.1038/s43247-021-00332-2>.
- (2) Tuckett, R. *Greenhouse Gases*; Elsevier Inc., 2019. <https://doi.org/10.1016/B978-0-12-409547-2.14031-4>.
- (3) IPCC. Climate Change 2021: The Physical Science Basis. Contribution of Working Group I to the Sixth Assessment Report of the Intergovernmental Panel on Climate Change [Masson-Delmotte, V., P. Zhai, A. Pirani, S. L. Connors, C. Péan, S. Berger, N. Caud, Y. Chen, . *Camb. Univ. Press* **2021**, No. In Press, 3949.
- (4) Friedlingstein, P.; O'Sullivan, M.; Jones, M. W.; Andrew, R. M.; Hauck, J.; Olsen, A.; Peters, G. P.; Peters, W.; Pongratz, J.; Sitch, S.; Le Quéré, C.; Canadell, J. G.; Ciais, P.; Jackson, R. B.; Alin, S.; Aragão, L. E. O. C.; Arneeth, A.; Arora, V.; Bates, N. R.; Becker, M.; Benoit-Cattin, A.; Bittig, H. C.; Bopp, L.; Bultan, S.; Chandra, N.; Chevallier, F.; Chini, L. P.; Evans, W.; Florentie, L.; Forster, P. M.; Gasser, T.; Gehlen, M.; Gilfillan, D.; Gkritzalis, T.; Gregor, L.; Gruber, N.; Harris, I.; Hartung, K.; Haverd, V.; Houghton, R. A.; Ilyina, T.; Jain, A. K.; Joetzjer, E.; Kadono, K.; Kato, E.; Kitidis, V.; Korsbakken, J. I.; Landschützer, P.; Lefèvre, N.; Lenton, A.; Lienert, S.; Liu, Z.; Lombardozzi, D.; Marland, G.; Metzl, N.; Munro, D. R.; Nabel, J. E. M. S.; Nakaoka, S.-I.; Niwa, Y.; O'Brien, K.; Ono, T.; Palmer, P. I.; Pierrot, D.; Poulter, B.; Resplandy, L.; Robertson, E.; Rödenbeck, C.; Schwinger, J.; Séférian, R.; Skjelvan, I.; Smith, A. J. P.; Sutton, A. J.; Tanhua, T.; Tans, P. P.; Tian, H.; Tilbrook, B.; van der Werf, G.; Vuichard, N.; Walker, A. P.; Wanninkhof, R.; Watson, A. J.; Willis, D.; Wiltshire, A. J.; Yuan, W.; Yue, X.; Zaehle, S. Global Carbon Budget 2020. *Earth Syst. Sci. Data* **2020**, 12 (4), 3269–3340. <https://doi.org/10.5194/essd-12-3269-2020>.
- (5) Petrescu, A. M. R.; Peters, G. P.; Janssens-Maenhout, G.; Ciais, P.; Tubiello, F. N.; Grassi, G.; Nabuurs, G.-J.; Leip, A.; Carmona-Garcia, G.; Winiwarter, W.; Höglund-Isaksson, L.; Günther, D.; Solazzo, E.; Kiesow, A.; Bastos, A.; Pongratz, J.; Nabel, J. E. M. S.; Conchedda, G.; Pilli, R.; Andrew, R. M.; Schelhaas, M.-J.; Dolman, A. J. European Anthropogenic AFOLU Greenhouse Gas Emissions: A Review and Benchmark Data. *Earth Syst. Sci. Data* **2020**, 12 (2), 961–1001. <https://doi.org/10.5194/essd-12-961-2020>.
- (6) Directive 2008/50/EC of the European Parliament and of the Council on Ambient Air Quality and Cleaner Air for Europe, 2008.
- (7) Winkler Roland. Mögliche Wege Aus Dem Gasdilemma. 2022.
- (8) Halser, C.; Paraschiv, F. Pathways to Overcoming Natural Gas Dependency on Russia—The German Case. *Energies* **2022**, 15 (14), 4939. <https://doi.org/10.3390/en15144939>.
- (9) IOGP. The Potential for CCS and CCU in Europe. *Report* **2019**, 47.
- (10) Butnar, I.; Cronin, J.; Pye, S. Review of Carbon Capture Utilisation and Carbon Capture and Storage in Future EU Decarbonisation Scenarios. *Final Rep.* 57.
- (11) Roseno, K. T. de C.; Alves, R. M. de B.; Giudici, R.; Schmal, M. Syngas Production Using Natural Gas from the Environmental Point of View. In *Biofuels - State of Development*; Biernat, K., Ed.; InTech, 2018. <https://doi.org/10.5772/intechopen.74605>.
- (12) Lu, S.; Shi, Y.; Meng, N.; Lu, S.; Yu, Y.; Zhang, B. Electrosynthesis of Syngas via the Co-Reduction of CO₂ and H₂O. *Cell Rep. Phys. Sci.* **2020**, 1 (11), 100237. <https://doi.org/10.1016/j.xcrp.2020.100237>.
- (13) Martín, M. M. Syngas. In *Industrial Chemical Process Analysis and Design*; Elsevier, 2016; pp 199–297. <https://doi.org/10.1016/B978-0-08-101093-8.00005-7>.

- (14) Usman, M.; Wan Daud, W. M. A.; Abbas, H. F. Dry Reforming of Methane: Influence of Process Parameters—A Review. *Renew. Sustain. Energy Rev.* **2015**, *45*, 710–744. <https://doi.org/10.1016/j.rser.2015.02.026>.
- (15) Fan, L.; Tu, Z.; Chan, S. H. Recent Development of Hydrogen and Fuel Cell Technologies: A Review. *Energy Rep.* **2021**, *7*, 8421–8446. <https://doi.org/10.1016/j.egy.2021.08.003>.
- (16) Paykani, A.; Chehrmonavari, H.; Tsolakis, A.; Alger, T.; Northrop, W. F.; Reitz, R. D. Synthesis Gas as a Fuel for Internal Combustion Engines in Transportation. *Prog. Energy Combust. Sci.* **2022**, *90*, 100995. <https://doi.org/10.1016/j.pecs.2022.100995>.
- (17) Dalena, F.; Senatore, A.; Marino, A.; Gordano, A.; Basile, M.; Basile, A. Methanol Production and Applications: An Overview. In *Methanol*; Elsevier, 2018; pp 3–28. <https://doi.org/10.1016/B978-0-444-63903-5.00001-7>.
- (18) Pattabathula, V.; Richardson, J. Introduction to Ammonia Production. *Back Basics* **2016**, *7*.
- (19) Bozzano, G.; Manenti, F. Efficient Methanol Synthesis: Perspectives, Technologies and Optimization Strategies. *Prog. Energy Combust. Sci.* **2016**, *56*, 71–105. <https://doi.org/10.1016/j.pecs.2016.06.001>.
- (20) Ott, J.; Gronemann, V.; Pontzen, F.; Fiedler, E.; Grossmann, G.; Kersebohm, D. B.; Weiss, G.; Witte, C. Methanol. In *Ullmann's Encyclopedia of Industrial Chemistry*; Wiley-VCH Verlag GmbH & Co. KGaA, Ed.; Wiley-VCH Verlag GmbH & Co. KGaA: Weinheim, Germany, 2012; p a16_465.pub3. https://doi.org/10.1002/14356007.a16_465.pub3.
- (21) Boehman, A. L.; Corre, O. L. Combustion of Syngas in Internal Combustion Engines. *Combust. Sci. Technol.* **2008**, *180* (6), 1193–1206. <https://doi.org/10.1080/00102200801963417>.
- (22) Hagos, F. Y.; Aziz, A. R. A.; Sulaiman, S. A. Trends of Syngas as a Fuel in Internal Combustion Engines. *Adv. Mech. Eng.* **2014**, *6*, 401587. <https://doi.org/10.1155/2014/401587>.
- (23) da Rosa, A. V.; Ordóñez, J. C. Hydrogen Production. In *Fundamentals of Renewable Energy Processes*; Elsevier, 2022; pp 419–470. <https://doi.org/10.1016/B978-0-12-816036-7.00021-X>.
- (24) Sajjadi, S. M.; Haghighi, M.; Rahmani, F. Sol–Gel Synthesis of Ni–Co/Al₂O₃–MgO–ZrO₂ Nanocatalyst Used in Hydrogen Production via Reforming of CH₄/CO₂ Greenhouse Gases. *J. Nat. Gas Sci. Eng.* **2015**, *22*, 9–21. <https://doi.org/10.1016/j.jngse.2014.11.014>.
- (25) Sharifi, M.; Haghighi, M.; Abdollahifar, M. Hydrogen Production via Reforming of Biogas over Nanostructured Ni/Y Catalyst: Effect of Ultrasound Irradiation and Ni-Content on Catalyst Properties and Performance. *Mater. Res. Bull.* **2014**, *60*, 328–340. <https://doi.org/10.1016/j.materresbull.2014.07.027>.
- (26) Assessment, U. E. N. C. for E. *Dry reforming of greenhouse gases CH₄/CO₂ over MgO-promoted Ni-Co/Al₂O₃-ZrO₂ nanocatalyst: effect of MgO addition via sol-gel method on catalytic properties and hydrogen yield.* https://hero.epa.gov/hero/index.cfm/reference/details/reference_id/2661892 (accessed 2022-07-22).
- (27) Xu, L.; Song, H.; Chou, L. J. Ordered Mesoporous MgO–Al₂O₃ Composite Oxides Supported Ni Based Catalysts for CO₂ Reforming of CH₄: Effects of Basic Modifier

and Mesopore Structure. *Int. J. Hydrog. Energy* **2013**, *38*, 7307–7325. <https://doi.org/10.1016/j.ijhydene.2013.04.034>.

- (28) Rezaei, M.; Alavi, S.; Sahebdehfar, S.; Yan, Z. Syngas Production by Methane Reforming with Carbon Dioxide on Noble Metal Catalysts. **2006**. [https://doi.org/10.1016/S1003-9953\(07\)60014-0](https://doi.org/10.1016/S1003-9953(07)60014-0).
- (29) Nguyen, V. N.; Blum, L. Syngas and Synfuels from H₂O and CO₂: Current Status. *Chem. Ing. Tech.* **2015**, *87* (4), 354–375. <https://doi.org/10.1002/cite.201400090>.
- (30) Göransson, K.; Söderlind, U.; He, J.; Zhang, W. Review of Syngas Production via Biomass DFBGs. *Renew. Sustain. Energy Rev.* **2011**, *15* (1), 482–492. <https://doi.org/10.1016/j.rser.2010.09.032>.
- (31) Ren, J.; Liu, Y.-L.; Zhao, X.-Y.; Cao, J.-P. Methanation of Syngas from Biomass Gasification: An Overview. *Int. J. Hydrog. Energy* **2020**, *45* (7), 4223–4243. <https://doi.org/10.1016/j.ijhydene.2019.12.023>.
- (32) Niu, M.; Huang, Y.; Jin, B.; Liang, S.; Dong, Q.; Gu, H.; Sun, R. A Novel Two-Stage Enriched Air Biomass Gasification for Producing Low-Tar High Heating Value Fuel Gas: Pilot Verification and Performance Analysis. *Energy* **2019**, *173*, 511–522. <https://doi.org/10.1016/j.energy.2019.02.068>.
- (33) Aziz, M. A. A.; Jalil, A. A.; Triwahyono, S.; Ahmad, A. CO₂ Methanation over Heterogeneous Catalysts: Recent Progress and Future Prospects. *Green Chem.* **2015**, *17* (5), 2647–2663. <https://doi.org/10.1039/C5GC00119F>.
- (34) Steinfeld, A. Solar Hydrogen Production via a Two-Step Water-Splitting Thermochemical Cycle Based on Zn/ZnO Redox Reactions. *Int. J. Hydrog. Energy* **2002**, *27* (6), 611–619. [https://doi.org/10.1016/S0360-3199\(01\)00177-X](https://doi.org/10.1016/S0360-3199(01)00177-X).
- (35) Roeb, M.; Neises, M.; Monnerie, N.; Call, F.; Simon, H.; Sattler, C.; Schmücker, M.; Pitz-Paal, R. Materials-Related Aspects of Thermochemical Water and Carbon Dioxide Splitting: A Review. *Materials* **2012**, *5* (11), 2015–2054. <https://doi.org/10.3390/ma5112015>.
- (36) Serpone, N.; Lawless, D.; Terzian, R. Solar Fuels: Status and Perspectives. *Sol. Energy* **1992**, *49* (4), 221–234. [https://doi.org/10.1016/0038-092X\(92\)90001-Q](https://doi.org/10.1016/0038-092X(92)90001-Q).
- (37) E. Funk, J. Thermochemical Hydrogen Production: Past and Present. *Int. J. Hydrog. Energy* **2001**, *26* (3), 185–190. [https://doi.org/10.1016/S0360-3199\(00\)00062-8](https://doi.org/10.1016/S0360-3199(00)00062-8).
- (38) Smestad, G. P.; Steinfeld, A. Review: Photochemical and Thermochemical Production of Solar Fuels from H₂O and CO₂ Using Metal Oxide Catalysts. *Ind. Eng. Chem. Res.* **2012**, *51* (37), 11828–11840. <https://doi.org/10.1021/ie3007962>.
- (39) Fujishima, A.; Honda, K. Electrochemical Photolysis of Water at a Semiconductor Electrode. *Nature* **1972**, *238* (5358), 37–38. <https://doi.org/10.1038/238037a0>.
- (40) Lin, F.; Boettcher, S. W. Adaptive Semiconductor/Electrocatalyst Junctions in Water-Splitting Photoanodes. *Nat. Mater.* **2014**, *13* (1), 81–86. <https://doi.org/10.1038/nmat3811>.
- (41) Mergel, J. Current Status and Future Trends. *Electrochem. Process Eng.* 35.
- (42) Ivy, J. Summary of Electrolytic Hydrogen Production: Milestone Completion Report. 27.
- (43) Bodner, M.; Hofer, A.; Hacker, V. H₂ Generation from Alkaline Electrolyzer. *Wiley Interdiscip. Rev. Energy Environ.* **2015**, *4* (4), 365–381.
- (44) Ursúa, A.; Gandía, L. M.; Sanchis, P. Hydrogen Production From Water Electrolysis: Current Status and Future Trends. *Proc. IEEE* **2012**. <https://doi.org/10.1109/JPROC.2011.2156750>.

- (45) Graves, C.; Ebbesen, S. D.; Mogensen, M.; Lackner, K. S. Sustainable Hydrocarbon Fuels by Recycling CO₂ and H₂O with Renewable or Nuclear Energy. *Renew. Sustain. Energy Rev.* **2011**, *15* (1), 1–23. <https://doi.org/10.1016/j.rser.2010.07.014>.
- (46) Sun, Z.; Ma, T.; Tao, H.; Fan, Q.; Han, B. Fundamentals and Challenges of Electrochemical CO₂ Reduction Using Two-Dimensional Materials. *Chem* **2017**, *3* (4), 560–587. <https://doi.org/10.1016/j.chempr.2017.09.009>.
- (47) Mistry, H.; Varela, A. S.; Bonifacio, C. S.; Zegkinoglou, I.; Sinev, I.; Choi, Y.-W.; Kisslinger, K.; Stach, E. A.; Yang, J. C.; Strasser, P.; Cuenya, B. R. Highly Selective Plasma-Activated Copper Catalysts for Carbon Dioxide Reduction to Ethylene. *Nat. Commun.* **2016**, *7*, 12123. <https://doi.org/10.1038/ncomms12123>.
- (48) Lee, S.; Kim, D.; Lee, J. Electrocatalytic Production of C₃-C₄ Compounds by Conversion of CO₂ on a Chloride-Induced Bi-Phase Cu₂O-Cu Catalyst. *Angew. Chem. Int. Ed.* **2015**, *54* (49), 14701–14705.
- (49) Geioushy, R.; Khaled, M.; Alhooshani, K.; Hakeem, A.; Rinaldi, A. Graphene/ZnO/Cu₂O Electrocatalyst for Selective Conversion of CO₂ into n-Propanol. **2017**. <https://doi.org/10.1016/J.ELECTACTA.2017.05.185>.
- (50) Thorson, M. R.; Siil, K. I.; Kenis, P. J. A. Effect of Cations on the Electrochemical Conversion of CO₂ to CO. *J. Electrochem. Soc.* **2012**, *160* (1), F69. <https://doi.org/10.1149/2.052301jes>.
- (51) Hori, Y.; Murata, A.; Takahashi, R. Formation of Hydrocarbons in the Electrochemical Reduction of Carbon Dioxide at a Copper Electrode in Aqueous Solution. *J. Chem. Soc. Faraday Trans. 1 Phys. Chem. Condens. Phases* **1989**, *85* (8), 2309–2326. <https://doi.org/10.1039/F19898502309>.
- (52) Kortlever, R.; Shen, J.; Schouten, K. J. P.; Calle-Vallejo, F.; Koper, M. T. M. Catalysts and Reaction Pathways for the Electrochemical Reduction of Carbon Dioxide. *J. Phys. Chem. Lett.* **2015**, *6* (20), 4073–4082. <https://doi.org/10.1021/acs.jpcllett.5b01559>.
- (53) Nie, X.; Esopi, M. R.; Janik, M. J.; Asthagiri, A. Selectivity of CO₂ Reduction on Copper Electrodes: The Role of the Kinetics of Elementary Steps. *Angew. Chem. Int. Ed.* **2013**, *52* (9), 2459–2462.
- (54) Hansen, H. A.; Varley, J. B.; Peterson, A. A.; Nørskov, J. K. Understanding Trends in the Electrocatalytic Activity of Metals and Enzymes for CO₂ Reduction to CO. *J. Phys. Chem. Lett.* **2013**, *4* (3), 388–392. <https://doi.org/10.1021/jz3021155>.
- (55) Shen, F.; Shi, J.; Shi, F.; Chen, T.; Li, Y.; Li, Q.; Dai, Y.; Yang, B.; Qu, T. Fabrication of Ag₂S Electrode for CO₂ Reduction in Organic Media. *Ionics* **2019**, *25* (4), 1921–1927. <https://doi.org/10.1007/s11581-018-2728-7>.
- (56) Ma, D.; Ying, Y.; Zhang, K.; Gao, Y.; Zhou, L.; Song, A.; Zhu, Y.; Xie, K.; Jin, T.; Huang, H. Greatly Enhanced CO₂ Electrocatalytic Reduction Performance of Ag₂Se Nanocatalyst via Phase-Engineering. *Appl. Catal. B Environ.* **2022**, *316*, 121658. <https://doi.org/10.1016/j.apcatb.2022.121658>.
- (57) Hori, Y.; Kikuchi, K.; Suzuki, S. PRODUCTION OF CO AND CH₄ IN ELECTROCHEMICAL REDUCTION OF CO₂ AT METAL ELECTRODES IN AQUEOUS HYDROGENCARBONATE SOLUTION. *Chem. Lett.* **1985**, *14* (11), 1695–1698. <https://doi.org/10.1246/cl.1985.1695>.
- (58) Zhang, Z.; Yates, J. T. Band Bending in Semiconductors: Chemical and Physical Consequences at Surfaces and Interfaces. *Chem. Rev.* **2012**, *112* (10), 5520–5551. <https://doi.org/10.1021/cr3000626>.

- (59) Kumar, B.; Llorente, M.; Froehlich, J.; Dang, T.; Sathrum, A.; Kubiak, C. P. Photochemical and Photoelectrochemical Reduction of CO₂. *Annu. Rev. Phys. Chem.* **2012**, *63* (1), 541–569. <https://doi.org/10.1146/annurev-physchem-032511-143759>.
- (60) Gerischer, H. Photodecomposition of Semiconductors Thermodynamics, Kinetics and Application to Solar Cells. *Faraday Discuss. Chem. Soc.* **1980**, *70*, 137. <https://doi.org/10.1039/dc9807000137>.
- (61) White, J. L.; Baruch, M. F.; Pander, J. E.; Hu, Y.; Fortmeyer, I. C.; Park, J. E.; Zhang, T.; Liao, K.; Gu, J.; Yan, Y.; Shaw, T. W.; Abelev, E.; Bocarsly, A. B. Light-Driven Heterogeneous Reduction of Carbon Dioxide: Photocatalysts and Photoelectrodes. *Chem. Rev.* **2015**, *115* (23), 12888–12935. <https://doi.org/10.1021/acs.chemrev.5b00370>.
- (62) Zhu, W.; Michalsky, R.; Metin, Ö.; Lv, H.; Guo, S.; Wright, C. J.; Sun, X.; Peterson, A. A.; Sun, S. Monodisperse Au Nanoparticles for Selective Electrocatalytic Reduction of CO₂ to CO. *J. Am. Chem. Soc.* **2013**, *135* (45), 16833–16836. <https://doi.org/10.1021/ja409445p>.
- (63) Zhu, W.; Zhang, Y.-J.; Zhang, H.; Lv, H.; Li, Q.; Michalsky, R.; Peterson, A. A.; Sun, S. Active and Selective Conversion of CO₂ to CO on Ultrathin Au Nanowires. *J. Am. Chem. Soc.* **2014**, *136* (46), 16132–16135. <https://doi.org/10.1021/ja5095099>.
- (64) Feng, X.; Jiang, K.; Fan, S.; Kanan, M. W. Grain-Boundary-Dependent CO₂ Electroreduction Activity. *J. Am. Chem. Soc.* **2015**, *137* (14), 4606–4609. <https://doi.org/10.1021/ja5130513>.
- (65) Liu, S.; Tao, H.; Zeng, L.; Liu, Q.; Xu, Z.; Liu, Q.; Luo, J.-L. Shape-Dependent Electrocatalytic Reduction of CO₂ to CO on Triangular Silver Nanoplates. *J. Am. Chem. Soc.* **2017**, *139* (6), 2160–2163. <https://doi.org/10.1021/jacs.6b12103>.
- (66) Sheng, W.; Kattel, S.; Yao, S.; Yan, B.; Liang, Z.; Hawxhurst, C. J.; Wu, Q.; Chen, J. G. Electrochemical Reduction of CO₂ to Synthesis Gas with Controlled CO/H₂ Ratios. *Energy Environ. Sci.* **2017**, *10* (5), 1180–1185. <https://doi.org/10.1039/c7ee00071e>.
- (67) Zhu, Y.; Yu, J.; Fan, Z.; Zhang, Z. 2D Materials for Electrochemical Carbon Dioxide Reduction. In *Nanomaterials for CO₂ Capture, Storage, Conversion and Utilization*; Elsevier, 2021; pp 183–196. <https://doi.org/10.1016/B978-0-12-822894-4.00006-X>.
- (68) Yang, S.-C.; Su, W.-N.; Rick, J.; Lin, S. D.; Liu, J.-Y.; Pan, C.-J.; Lee, J.-F.; Hwang, B.-J. Oxygen Vacancy Engineering of Cerium Oxides for Carbon Dioxide Capture and Reduction. *ChemSusChem* **2013**, *6* (8), 1326–1329.
- (69) Geng, Z.; Kong, X.; Chen, W.; Su, H.; Liu, Y.; Cai, F.; Wang, G.; Zeng, J. Oxygen Vacancies in ZnO Nanosheets Enhance CO₂ Electrochemical Reduction to CO. *Angew. Chem. Int. Ed.* **2018**, *57* (21), 6054–6059.
- (70) Xie, H.; Chen, S.; Ma, F.; Liang, J.; Miao, Z.; Wang, T.; Wang, H.-L.; Huang, Y.; Li, Q. Boosting Tunable Syngas Formation via Electrochemical CO₂ Reduction on Cu/In₂O₃ Core/Shell Nanoparticles. *ACS Appl. Mater. Interfaces* **2018**, *10* (43), 36996–37004. <https://doi.org/10.1021/acsami.8b12747>.
- (71) Li, Q.; Fu, J.; Zhu, W.; Chen, Z.; Shen, B.; Wu, L.; Xi, Z.; Wang, T.; Lu, G.; Zhu, J.; Sun, S. Tuning Sn-Catalysis for Electrochemical Reduction of CO₂ to CO via the Core/Shell Cu/SnO₂ Structure. *J. Am. Chem. Soc.* **2017**, *139* (12), 4290–4293. <https://doi.org/10.1021/jacs.7b00261>.
- (72) Bi, W.; Wu, C.; Xie, Y. Atomically Thin Two-Dimensional Solids: An Emerging Platform for CO₂ Electroreduction. *ACS Energy Lett.* **2018**, *3* (3), 624–633. <https://doi.org/10.1021/acsenergylett.7b01343>.

- (73) Gao, S.; Lin, Y.; Jiao, X.; Sun, Y.; Luo, Q.; Zhang, W.; Li, D.; Yang, J.; Xie, Y. Partially Oxidized Atomic Cobalt Layers for Carbon Dioxide Electroreduction to Liquid Fuel. *Nature* **2016**, 529 (7584), 68–71. <https://doi.org/10.1038/nature16455>.
- (74) Zhang, S.; Kang, P.; Meyer, T. J. Nanostructured Tin Catalysts for Selective Electrochemical Reduction of Carbon Dioxide to Formate. *J. Am. Chem. Soc.* **2014**, 136 (5), 1734–1737. <https://doi.org/10.1021/ja4113885>.
- (75) Peng, X.; Chen, Y.; Mi, Y.; Zhuo, L.; Qi, G.; Ren, J.; Qiu, Y.; Liu, X.; Luo, J. Efficient Electroreduction CO₂ to CO over MnO₂ Nanosheets. *Inorg. Chem.* **2019**, 58 (14), 8910–8914. <https://doi.org/10.1021/acs.inorgchem.9b01018>.
- (76) Wang, L.; Sasaki, T. Titanium Oxide Nanosheets: Graphene Analogues with Versatile Functionalities. *Chem. Rev.* **2014**, 114 (19), 9455–9486. <https://doi.org/10.1021/cr400627u>.
- (77) Li, J.; Jiao, J.; Zhang, H.; Zhu, P.; Ma, H.; Chen, C.; Xiao, H.; Lu, Q. Two-Dimensional SnO₂ Nanosheets for Efficient Carbon Dioxide Electroreduction to Formate. *ACS Sustain. Chem. Eng.* **2020**, 8 (12), 4975–4982. <https://doi.org/10.1021/acssuschemeng.0c01070>.
- (78) Asadi, M.; Kumar, B.; Behranginia, A.; Rosen, B. A.; Baskin, A.; Reprin, N.; Pisasale, D.; Phillips, P.; Zhu, W.; Haasch, R.; Klie, R. F.; Král, P.; Abiade, J.; Salehi-Khojin, A. Robust Carbon Dioxide Reduction on Molybdenum Disulphide Edges. *Nat. Commun.* **2014**, 5 (1), 4470. <https://doi.org/10.1038/ncomms5470>.
- (79) Lü, F.; Qi, G.; Liu, X.; Zhang, C.; Guo, R.; Peng, X.; He, J.; Luo, J. Selective Electrolysis of CO₂ to CO on Ultrathin In₂Se₃ Nanosheets. *Electrochem. Commun.* **2019**, 103, 127–132. <https://doi.org/10.1016/j.elecom.2019.05.020>.
- (80) Xu, J.; Li, X.; Liu, W.; Sun, Y.; Ju, Z.; Yao, T.; Wang, C.; Ju, H.; Zhu, J.; Wei, S.; Xie, Y. Carbon Dioxide Electroreduction into Syngas Boosted by a Partially Delocalized Charge in Molybdenum Sulfide Selenide Alloy Monolayers. *Angew. Chem. Int. Ed.* **2017**, 56 (31), 9121–9125. <https://doi.org/10.1002/anie.201704928>.
- (81) O’Sullivan, C.; Gunning, R. D.; Sanyal, A.; Barrett, C. A.; Geaney, H.; Laffir, F. R.; Ahmed, S.; Ryan, K. M. Spontaneous Room Temperature Elongation of CdS and Ag₂S Nanorods via Oriented Attachment. *J. Am. Chem. Soc.* **2009**, 131 (34), 12250–12257. <https://doi.org/10.1021/ja902860t>.
- (82) Fan, W.; Jewell, S.; She, Y.; Leung, M. K. H. In Situ Deposition of Ag–Ag₂S Hybrid Nanoparticles onto TiO₂ Nanotube Arrays towards Fabrication of Photoelectrodes with High Visible Light Photoelectrochemical Properties. *Phys. Chem. Chem. Phys.* **2013**, 16 (2), 676–680. <https://doi.org/10.1039/C3CP54098G>.
- (83) Basu, M.; Nazir, R.; Mahala, C.; Fageria, P.; Chaudhary, S.; Gangopadhyay, S.; Pande, S. Ag₂S/Ag Heterostructure: A Promising Electrocatalyst for the Hydrogen Evolution Reaction. *Langmuir* **2017**, 33 (13), 3178–3186. <https://doi.org/10.1021/acs.langmuir.7b00029>.
- (84) Ye, K.; Liu, T.; Song, Y.; Wang, Q.; Wang, G. Tailoring the Interactions of Heterogeneous Ag₂S/Ag Interface for Efficient CO₂ Electroreduction. *Appl. Catal. B Environ.* **2021**, 296, 120342. <https://doi.org/10.1016/j.apcatb.2021.120342>.
- (85) Chen, Q. S.; Cui, P. L.; Yang, J.; Chen, D.; Liu, H.; Feng, H.; Tsiakaras, P.; Shen, P. K. Efficient Carbon Dioxide Electroreduction over Rationally Designed Heterogeneous Ag₂S–Au Nanocomposites. *J. Colloid Interface Sci.* **2022**, 623, 1172–1180. <https://doi.org/10.1016/j.jcis.2022.04.163>.

- (86) Cuthbert, H. L.; Wallbank, A. I.; Taylor, N. J.; Corrigan, J. F. Synthese Und Strukturelle Charakterisierung von [Cu 20 Se 4 (μ 3 -SePh) 12 (PPh 3) 6] Und. *Z Anorg Allg Chem* **2002**, 628, 2483–2488.
- (87) Schriber, E. A.; Popple, D. C.; Yeung, M.; Brady, M. A.; Corlett, S. A.; Hohman, J. N. Mithrene Is a Self-Assembling Robustly Blue Luminescent Metal-Organic Chalcogenolate Assembly for 2d Optoelectronic Applications. *ACS Appl. Nano Mater.* **2018**, 1 (7), 3498–3508. <https://doi.org/10.1021/acsanm.8b00662>.
- (88) Yan, H.; Hohman, J. N.; Li, F. H.; Jia, C.; Solis-Ibarra, D.; Wu, B.; Dahl, J. E. P.; Carlson, R. M. K.; Tkachenko, B. A.; Fokin, A. A.; Schreiner, P. R.; Vailionis, A.; Kim, T. R.; Devereaux, T. P.; Shen, Z. X.; Melosh, N. A. Hybrid Metal-Organic Chalcogenide Nanowires with Electrically Conductive Inorganic Core through Diamondoid-Directed Assembly. *Nat. Mater.* **2017**, 16 (3), 349–355. <https://doi.org/10.1038/nmat4823>.
- (89) Popple, D. C.; Schriber, E. A.; Yeung, M.; Hohman, J. N. Competing Roles of Crystallization and Degradation of a Metal-Organic Chalcogenolate Assembly under Biphasic Solvothermal Conditions. *Langmuir* **2018**, 34 (47), 14265–14273. <https://doi.org/10.1021/acs.langmuir.8b03282>.
- (90) Schriber, E. A.; Rosenberg, D. J.; Kelly, R. P.; Ghodsi, A.; Hohman, J. N. Investigation of Nucleation and Growth at a Liquid–Liquid Interface by Solvent Exchange and Synchrotron Small-Angle X-Ray Scattering. *Front. Chem.* **2021**, 9 (July), 1–9. <https://doi.org/10.3389/fchem.2021.593637>.
- (91) Paritmongkol, W.; Sakurada, T.; Lee, W. S.; Wan, R.; Müller, P.; Tisdale, W. A. Size and Quality Enhancement of 2D Semiconducting Metal–Organic Chalcogenolates by Amine Addition. *J Am Chem Soc* **2021**, 8.
- (92) Trang, B.; Yeung, M.; Popple, D. C.; Schriber, E. A.; Brady, M. A.; Kuykendall, T. R.; Hohman, J. N. Tarnishing Silver Metal into Mithrene. *J. Am. Chem. Soc.* **2018**, 140 (42), 13892–13903. <https://doi.org/10.1021/jacs.8b08878>.
- (93) Hohman, J. N.; Thomas, J. C.; Zhao, Y.; Auluck, H.; Kim, M.; Vijselaar, W.; Kommeren, S.; Terfort, A.; Weiss, P. S. Exchange Reactions between Alkanethiolates and Alkaneselenols on Au{111}. *J. Am. Chem. Soc.* **2014**, 136 (22), 8110–8121. <https://doi.org/10.1021/ja503432f>.
- (94) de la Llave, E.; Scherlis, D. A. Selenium-Based Self-Assembled Monolayers: The Nature of Adsorbate–Surface Interactions. *Langmuir* **2010**, 26 (1), 173–178. <https://doi.org/10.1021/la903660y>.
- (95) Fonder, G.; Delhalle, J.; Mekhalif, Z. Exchange versus Intercalation of N-Dodecanethiol Monolayers on Copper in the Presence of n-Dodecaneselenol and Vice Versa. *Appl. Surf. Sci.* **2010**, 256 (9), 2968–2973. <https://doi.org/10.1016/j.apsusc.2009.11.059>.
- (96) Hohman, J. N.; Kim, M.; Schüpbach, B.; Kind, M.; Thomas, J. C.; Terfort, A.; Weiss, P. S. Dynamic Double Lattice of 1-Adamantaneselenolate Self-Assembled Monolayers on Au{111}. *J. Am. Chem. Soc.* **2011**, 133 (48), 19422–19431. <https://doi.org/10.1021/ja2063988>.
- (97) Ossowski, J.; Wächter, T.; Silies, L.; Kind, M.; Noworolska, A.; Blobner, F.; Gnatek, D.; Rysz, J.; Bolte, M.; Feulner, P.; Terfort, A.; Cyganik, P.; Zharnikov, M. Thiolate versus Selenolate: Structure, Stability, and Charge Transfer Properties. *ACS Nano* **2015**, 9 (4), 4508–4526. <https://doi.org/10.1021/acsnano.5b01109>.
- (98) Reimers, J. R.; Ford, M. J.; Marcuccio, S. M.; Ulstrup, J.; Hush, N. S. Competition of van Der Waals and Chemical Forces on Gold–Sulfur Surfaces and Nanoparticles. *Nat. Rev. Chem.* **2017**, 1 (2), 0017. <https://doi.org/10.1038/s41570-017-0017>.

- (99) Monnell, J. D.; Stapleton, J. J.; Jackiw, J. J.; Dunbar, T.; Reinerth, W. A.; Dirk, S. M.; Tour, J. M.; Allara, D. L.; Weiss, P. S. Ordered Local Domain Structures of Decaneselenolate and Dodecane-selenolate Monolayers on Au{111}. *J. Phys. Chem. B* **2004**, *108* (28), 9834–9841. <https://doi.org/10.1021/jp037728x>.
- (100) Szelągowska-Kunstman, K.; Cyganik, P.; Schüpbach, B.; Terfort, A. Relative Stability of Thiol and Selenol Based SAMs on Au(111) — Exchange Experiments. *Phys. Chem. Chem. Phys.* **2010**, *12* (17), 4400–4406. <https://doi.org/10.1039/B923274P>.
- (101) Yeung, M.; Popple, D. C.; Schriber, E. A.; Teat, S. J.; Beavers, C. M.; Demessence, A.; Kuykendall, T. R.; Hohman, J. N. Corrosion of Late- and Post-Transition Metals into Metal-Organic Chalcogenolates and Implications for Nanodevice Architectures. *ACS Appl. Nano Mater.* **2020**, *3* (4), 3568–3577. <https://doi.org/10.1021/acsnm.0c00057>.
- (102) Maserati, L.; Refaely-Abramson, S.; Kastl, C.; Chen, C. T.; Borys, N. J.; Eisler, C. N.; Collins, M. S.; Smidt, T. E.; Barnard, E. S.; Strasbourg, M.; Schriber, E. A.; Shevitski, B.; Yao, K.; Hohman, J. N.; Schuck, P. J.; Aloni, S.; Neaton, J. B.; Schwartzberg, A. M. Anisotropic 2D Excitons Unveiled in Organic–Inorganic Quantum Wells. *Mater. Horiz.* **2021**, *8* (1), 197–208. <https://doi.org/10.1039/C9MH01917K>.
- (103) Stupp, S. I.; Palmer, L. C. Supramolecular Chemistry and Self-Assembly in Organic Materials Design. *Chem. Mater.* **2014**, *26* (1), 507–518. <https://doi.org/10.1021/cm403028b>.
- (104) Amabilino, D. B.; Smith, D. K.; Steed, J. W. Supramolecular Materials. *Chem. Soc. Rev.* **2017**, *46* (9), 2404–2420. <https://doi.org/10.1039/C7CS00163K>.
- (105) Mills, H.; Jones, C.; Anderson, K.; Ready, A.; Djurovich, P.; Khan, S.; Hohman, J. N.; Nelson, H.; Spokoyny, A. *Sterically Invariant Carborane-Based Ligands for the Morphological and Electronic Control of Metal–Organic Chalcogenolate Assemblies*; preprint; Chemistry, 2022. <https://doi.org/10.26434/chemrxiv-2022-twzjw>.
- (106) Schriber, E. A.; Paley, D. W.; Bolotovskiy, R.; Rosenberg, D. J.; Sierra, R. G.; Aquila, A.; Mendez, D.; Poitevin, F.; Blaschke, J. P.; Bhowmick, A.; Kelly, R. P.; Hunter, M.; Hayes, B.; Popple, D. C.; Yeung, M.; Pareja-Rivera, C.; Lisova, S.; Tono, K.; Sugahara, M.; Owada, S.; Kuykendall, T.; Yao, K.; Schuck, P. J.; Solis-Ibarra, D.; Sauter, N. K.; Brewster, A. S.; Hohman, J. N. Chemical Crystallography by Serial Femtosecond X-Ray Diffraction. *Nature* **2022**, *601* (7893), 360–365. <https://doi.org/10.1038/s41586-021-04218-3>.
- (107) Song, J. G.; Park, J.; Lee, W.; Choi, T.; Jung, H.; Lee, C. W.; Hwang, S. H.; Myoung, J. M.; Jung, J. H.; Kim, S. H.; Lansalot-Matras, C.; Kim, H. Layer-Controlled, Wafer-Scale, and Conformal Synthesis of Tungsten Disulfide Nanosheets Using Atomic Layer Deposition. *ACS Nano* **2013**, *7* (12), 11333–11340. <https://doi.org/10.1021/nn405194e>.
- (108) Tan, L. K.; Liu, B.; Teng, J. H.; Guo, S.; Low, H. Y.; Loh, K. P. Atomic Layer Deposition of a MoS₂ Film. *Nanoscale* **2014**, *6* (18), 10584–10588. <https://doi.org/10.1039/C4NR02451F>.
- (109) Schwartzberg, A. M.; Olynick, D. Complex Materials by Atomic Layer Deposition. *Adv. Mater.* **2015**, *27* (38), 5778–5784.
- (110) Orofeo, C. M.; Suzuki, S.; Sekine, Y.; Hibino, H. Scalable Synthesis of Layer-Controlled WS₂ and MoS₂ Sheets by Sulfurization of Thin Metal Films. *Appl. Phys. Lett.* **2014**, *105* (8), 083112. <https://doi.org/10.1063/1.4893978>.
- (111) Sinclair, J. Tarnishing of Silver by Organic Sulfur Vapors: Rates and Film Characteristics. **1982**. <https://doi.org/10.1149/1.2123787>.

- (112) Kastl, C.; Schwartzberg, A. M.; Maserati, L. Picoseconds-Limited Exciton Recombination in Metal–Organic Chalcogenides Hybrid Quantum Wells. *ACS Nano* **2022**, *16* (3), 3715–3722. <https://doi.org/10.1021/acsnano.1c07281>.
- (113) Loyalka, S. K.; Riggs, C. A. Inverse Problem in Diffuse Reflectance Spectroscopy: Accuracy of the Kubelka-Munk Equations. *Appl Spectrosc* **1995**, *49* (8), 1107–1110.
- (114) Bard, A. J.; Parson, R.; Jordan, J. *Standard Potentials in Aqueous Solutions*; CRC Press, 1985.
- (115) Yao, K.; Collins, M. S.; Nell, K. M.; Barnard, E. S.; Borys, N. J.; Kuykendall, T.; Hohman, J. N.; Schuck, P. J. Strongly Quantum-Confined Blue-Emitting Excitons in Chemically Configurable Multiquantum Wells. *ACS Nano* **2021**, *15* (3), 4085–4092. <https://doi.org/10.1021/acsnano.0c08096>.
- (116) Maserati, L. Understanding the Synthetic Pathway to Large Area, High Quality [AgSePh] ∞ Nanocrystal Films. 9.
- (117) Kodom, T.; Rusen, E.; Călinescu, I.; Mocanu, A.; Șomoghi, R.; Dinescu, A.; Diacon, A.; Boscornea, C. Silver Nanoparticles Influence on Photocatalytic Activity of Hybrid Materials Based on TiO₂ P25. *J. Nanomater.* **2015**, *2015*, 1–8. <https://doi.org/10.1155/2015/210734>.
- (118) Kim, C.; Jeon, H. S.; Eom, T.; Jee, M. S.; Kim, H.; Friend, C. M.; Min, B. K.; Hwang, Y. J. Achieving Selective and Efficient Electrocatalytic Activity for CO₂ Reduction Using Immobilized Silver Nanoparticles. *J. Am. Chem. Soc.* **2015**, *137* (43), 13844–13850. <https://doi.org/10.1021/jacs.5b06568>.
- (119) Li, Z. Q.; Lu, C. J.; Xia, Z. P.; Zhou, Y.; Luo, Z. X-Ray Diffraction Patterns of Graphite and Turbostratic Carbon. *Carbon* **2007**, *45* (8), 1686–1695. <https://doi.org/10.1016/j.carbon.2007.03.038>.
- (120) Ivanov, V. B.; Bitt, V. V.; Solina, E. V.; Samoryadov, A. V. Reversible and Irreversible Color Change during Photo and Thermal Degradation of PolyphenyleneSulfide Composite. *Polymers* **2019**, *11* (10), 1579. <https://doi.org/10.3390/polym11101579>.

13 Appendix

13.1 List of Abbreviations

ΔH	Gibbs free enthalpy
ATR-FTIR	Attenuated total reflection Fourier transformed infrared spectroscopy
Ag-NP	Silver nanoparticles
CB	Conduction band
CE	Counter electrode
CP	Carbon paper
CV	Cyclic voltammetry
CCS	Carbon capture storage
CCU	Carbon capture utilization
D	Dimension
DRS	Diffuse reflectance spectroscopy
EDX	Energy dispersive X-ray
E_g	Band gap
EIS	Electrochemical impedance spectroscopy
EU	European Union
FE	Faraday Efficiency
GC	Gas chromatography
HER	Hydrogen evolution reaction
HT	High temperature
IPCC	Intergovernmental panel on climate change
LED	Light emitting diodes
LSV	Liner sweep voltammetry
MOCHA	Metal organic chalcogenolate assembly
MOCP	Metal organic chalcogenolate polymer
PAHs	Polycyclic aromatic hydrocarbons
PEM	Proton exchange membrane
PM	Particulate matter
R	Rate in $\mu\text{mol h}^{-1}$
RE	Reference electrode
RHE	Reversible hydrogen electrode
SAM	Self assembled monolayers
SEM	Scanning electron microscopy
SHE	Standard hydrogen electrode
SOEC	Solid oxide electrolysis cell
TXRF	Total X-ray fluorescence spectroscopy
UV	Ultra violet
VB	Valence band
WE	Working electrode
XPS	X-ray photoelectron spectroscopy
XRD	X-ray diffraction

13.2 List of Figures

Figure 1. Reaction pathway of CO ₂ reduction to carbon monoxide via coupled proton / electron *COOH formation (up) and decoupled *COOH formation (down) Reproduced with permission from ^{46,52} . Copyright 2017 Elsevier Inc.	14
Figure 2. Schematic of energy band behaviour of an a. intrinsic semiconductor, b. n-type extrinsic semiconductor and d. p-type extrinsic semiconductor in disequilibrium and c and e. in equilibrium due to band bending. Reproduced with permission from ⁵⁸ Copyright 2012 American Chemical Society.	15
Figure 3. Structures of the A. silver benzeneselenolate MOCHA mithrene and the B. silver benzenesulphonolate MOCHA thiorene.	18
Figure 4. A. Microwave oven and B. temperature, pressure and power behaviour during 5h MOCHA synthesis.	28
Figure 5. Schematic of the steps performed for electrocatalytic CO ₂ RR. Electrochemical cell, connected to a potentiostat displaying current and charge over electrolysis time (up), taking of sample from the headspace of the cell (down middle) and injecting to the GC for product determination and quantification (down left corner) by means of Faraday efficiency (equation upper right corner).	32
Figure 6. XRD patterns of mithrene synthesized by microwave and hydrothermal autoclave synthesis performed over a time frame of 1-120 hours.	35
Figure 7. SEM images and pictures (lower right corner) of mithrene on CP prepared using various deposition methods including A. spincoating, B. painting, C. dropcasting and D. dipcoating.	36
Figure 8. SEM images of A. a bare carbon paper electrode, B. an [AgSePh] _∞ / CP electrode and C. an [AgSePh] _∞ / CP electrode with photodeposited silver nanoparticles on it.	37
Figure 9. Characterization of the MOCHAs mithrene ([AgSePh] _∞ , orange line) and thiorene ([AgSPh] _∞ , red line) by means of A. SEM, B. XRD, C. ATR-FTIR and D. DRS measurements.	38
Figure 10. LSV measurements performed under nitrogen (black line) and carbon dioxide (red line) in darkness (A-C) and upon 456 nm illumination (D-F) with A,D. a bare CP electrode, B,E. a mithrene / CP electrode and C,F. a thiorene / CP electrode.	40
Figure 11. Photocurrent measurements performed with a mithrene / FTO electrode at 365 nm illumination (purple line) and 456 nm illumination (blue line).	41
Figure 12. A. Faraday efficiencies for H ₂ (purple) and CO (grey) production and their corresponding B. rates for H ₂ (blue) and CO (green). Measurements were performed in darkness at three different overpotentials (-1.0, -0.8 and -0.6 V vs. RHE) with three different electrodes CP, [AgSePh] _∞ / CP and [AgSPh] _∞ / CP.	42
Figure 13. A. Faraday efficiencies for H ₂ (purple) and CO (grey) production and their corresponding B. rates for H ₂ (blue) and CO (green). Measurements were performed upon 456 nm illumination at three different overpotentials (-1.0, -0.8 and -0.6 V vs. RHE) with three different electrodes CP, [AgSePh] _∞ / CP and [AgSPh] _∞ / CP.	45
Figure 14. Effect of silver nanoparticle deposition onto MOCHA / CP electrodes is shown. A. Faraday efficiencies for H ₂ (purple) and CO (grey) production and their corresponding B. rates for H ₂ (blue) and CO (green). Measurements were performed upon 456 nm illumination at three different overpotentials (-1.0, -0.8 and -0.6 V vs. RHE) with two different electrodes [AgSePh] _∞ / Ag-NP/ CP and [AgSPh] _∞ / Ag-NP/ CP.	47
Figure 15. Stability test results performed on mithrene in various organic solvent stored at room temperature for one week. A. images of mithrene on a Si-substrate in (from left to right) EtAc, IPA, MeOH and DMF. B. SEM images of mithrene after exposure to the organic solvent EtAc, IPA and MeOH (from left to right). C. XRD patterns of a mithrene reference (black line) and of mithrene exposed to IPA (green line), MeOH (blue line) and EtAc (purple line). D. XRD patterns of a mithrene	

reference sample (black line), the Si-substrate after DMF exposure (purple line) and a sample taken from the DMF / mithrene suspension (pink line)..... 48

Figure 16. Results of light illumination (456 nm) stability testing. **A.** image of the testing setup. **B.** XRD patterns of a mithrene reference (black line) and mithrene samples being exposed for 10 min (blue-green line), 1h (bright blue line), 24h (blue line) and 72 (dark blue line). **C.** SEM images and pictures (lower right corner) of mithrene being exposed 10 min, 1h, 24h and 72h (from left to right) to 456 nm illumination. 49

Figure 17. Stability test results upon electrolysis. **A.** SEM images of mithrene after electrolysis. **B.** XRD pattern of mithrene after electrolysis under all tested conditions. **C.** SEM images of mithrene + Ag-NP deposition after electrolysis. **D.** XRD patterns of mithrene + Ag-NP after electrolysis under all tested conditions. **E.** Rate of H₂ (blue) and CO (green) after electrolysis at -1.0 V vs. RHE in darkness after using the same [AgSePh]_∞ / CP electrode four times. 51

Figure 18. Stability test results upon electrolysis. **A.** SEM images of thiorene after electrolysis. **B.** XRD patterns of thiorene after electrolysis under all tested conditions. **C.** SEM images of thiorene + Ag-NP deposition after electrolysis. **D.** XRD pattern of thiorene + Ag-NP depositions after electrolysis under all tested conditions. 52

Figure 19 A. SEM images and images of the new prepared “MOCHAs2. **B.** ATR-FTIR spectra and **C.** XRD pattern of the “MOCHAs” [NiSePh]_∞ (green line), [CuSePh]_∞ (blue line), [CuSPh]_∞ (grey line), [FeSPh]_∞ (red line) and [FeSePh]_∞ (brown line). 53

Figure 20. Stability results for mithrene at various pH values. **A.** SEM images at pH 0 (upper left corner), pH 3 (upper right corner), pH 7 (down left corner), and pH 9 (down right corner) and **B.** XRD pattern of a mithrene reference (black line), mithrene powder at pH 0 (dark red line), pH 3 (red line), pH 7 (orange line) and pH 9 (green line). 73

Figure 21. Stability test results of mithrene at various temperatures. **A.** SEM images of mithrene after one week being exposed to -25 °C (upper left corner), 60 °C (upper right corner), 80 °C (down left corner), and 120 °C (down right corner). **B.** XRD pattern of a mithrene reference (black line) and mithrene stored at -25 °C (blue line), 60 °C (orange line), 80 °C (red line) and 120 °C (purple line).73

Figure 22. Results of light illumination (365 nm) stability testing. **A.** image of the testing setup. **B.** XRD patterns of a mithrene reference (black line) and mithrene samples being exposed for 10 min (weak purple line), 1h (bright purple line), 24h (purple line) and 72 (dark purple line). **C.** SEM images and pictures (lower right corner) of mithrene being exposed 10 min, 1h, 24h and 72h (from left to right) to 365 nm illumination. 74

Figure 23. Results of light illumination (VIS light, solar simulator) stability testing. **A.** image of the testing setup. **B.** XRD patterns of a mithrene reference (black line) and mithrene samples being exposed for 10 min (green line), 1h (brown line), 24h (orange line) and 72 (red line). **C.** SEM images and pictures (lower right corner) of mithrene being exposed 10 min, 1h, 24h and 72h (from left to right) to solar simulator illumination. 74

Figure 24. TXRF spectra of synthesized MOCHAs. Mithrene (orange line), thiorene (grey line), thiorene with thiophenol as precursor (light grey line), [FeSePh]_∞ (brown line), [FeSPh]_∞ (red line), [CuSePh]_∞ (blue line) and [NiSePh]_∞ (green line). 75

Figure 25. EDX spectra and atomic- and weight% ratio results for mithrene. 76

Figure 26. EDX spectra and atomic- and weight% ratio results for thiorene..... 76

13.3 List of Tables

Table 1. Possible reaction products of electrochemical CO ₂ RR and HER (last line) and their corresponding formal redox potential vs. SHE.....	13
Table 2. Names and abbreviations of used chemicals, their CAS-number, supplier and purities.	24
Table 3. Instruments and devices used to perform the here presented work.....	26
Table 4. Theoretical and experimental values for metal, chalcogenide and carbon ratio obtained by EDX, XPS and TXRF techniques.....	39
Table 5. Theoretical and experimental element ratio obtained by XPS and TXRF measurements. .	54
Table 6. Reaction conditions for the microwave synthesis.	72
Table 7. All performed electrolyses with their used electrodes, potentials, durations, atmospheres, illumination, FE's and Rates.	77

13.4 List of all tested microwave synthesis conditions

Table 6. Reaction conditions for the microwave synthesis.

Name	Metal nitrate	Amount	DPDX (X=S, Se, Te)	Amount	Temperature	Duration	Success
MW01	AgNO ₃	85 mg	DPDSe	-	110 °C	14 h	No
MW02	AgNO ₃	85 mg	DPDSe	250 mg	100 °C	12 h	No
MW03	AgNO ₃	85 mg	DPDSe	234 mg	110 °C	14 h	Yes
MW04	AgNO ₃	85 mg	DPDSe	234 mg	110 °C	5 h	Yes
MW05	AgNO ₃	250 mg	DPDSe	321 mg	75 °C	2.75 h	No
MW06	AgNO ₃	250 mg	DPDSe	321 mg	70 °C	2 h	No
MW07	AgNO ₃	85 mg	DPDS	72.83 mg	110 °C	14 h	No
MW08	AgNO ₃	85 mg	DPDS	164 mg	110 °C	14 h	Yes
MW09	AgNO ₃	85 mg	DPDTe	307 mg	110 °C	14 h	No
MW10	AgNO ₃	85 mg	DPDS	164 mg	110 °C	0.5 h	Yes
MW11	AgNO ₃	85 mg	DPDS	164 mg	150 °C	35 min	No
MW12	AgNO ₃	85 mg	DPDSe	234 mg	110 °C	1 h	Yes
MW13	AgNO ₃	85 mg	DPDSe	234 mg	110 °C	3 h	Yes
MW14	AgNO ₃	42 mg	DPDTe	153 mg	110 °C	16 h	No
MW15	AgNO ₃	85 mg	DPDSe	234 mg	150 °C-180 °C	3 min, 1 h	No/Yes
MW16	Fe(NO ₃) ₃ 9H ₂ O	202 mg	DPDSe	234 mg	110 °C	1 h	No
MW17	Cu(NO ₃) ₂ 3H ₂ O	121 mg	DPDSe	250 mg	110 °C	1 h	No
MW18	Ni(NO ₃) ₂ 6H ₂ O	145.5 mg	DPDSe	234 mg	110 °C	1 h	No
MW19	Cu(NO ₃) ₂ 3H ₂ O	121 mg	DPDSe	234 mg	110 °C	14 h	No
MW20	Cu(NO ₃) ₂ 3H ₂ O	121 mg	DPDSe	234 mg	180 °C	1 h	No
MW21	Ni(NO ₃) ₂ 6H ₂ O	145.5 mg	DPDSe	234 mg	180 °C	1 h	No
MW22	Cu(NO ₃) ₂ 3H ₂ O	121 mg	DPDSe	234 mg	110 °C	5 h	Yes
MW23	Fe(NO ₃) ₃ 9H ₂ O	202 mg	DPDSe	234 mg	110 °C	5 h	Yes
MW24	Ni(NO ₃) ₂ 6H ₂ O	145.5 mg	DPDSe	234 mg	110 °C	5 h	Yes
MW25	AgNO ₃	42.5 mg	DPDTe	153 mg	110 °C	5 h	No
MW26	AgNO ₃	27 mg	DPDTe	80 mg	80 °C	1 h	No
MW27	AgNO ₃	42.5 mg	DPDTe	153 mg	180 °C	1 h	No
MW28	AgNO ₃	42.5 mg	DPDTe	153 mg	150 °C	4 h	No

13.5 pH, temperature and illumination stability, TXRF and EDX spectra

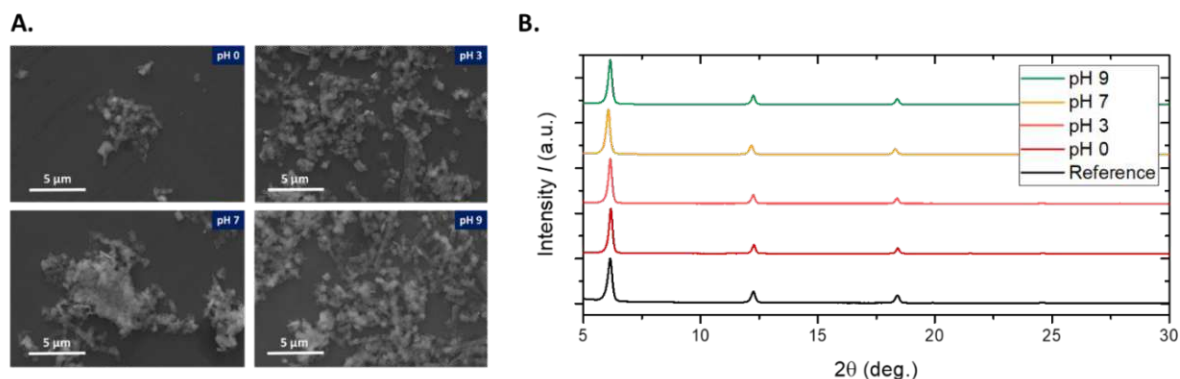


Figure 20. Stability results for mithrene at various pH values. **A.** SEM images at pH 0 (upper left corner), pH 3 (upper right corner), pH 7 (down left corner), and pH 9 (down right corner) and **B.** XRD pattern of a mithrene reference (black line), mithrene powder at pH 0 (dark red line), pH 3 (red line), pH 7 (orange line) and pH 9 (green line).

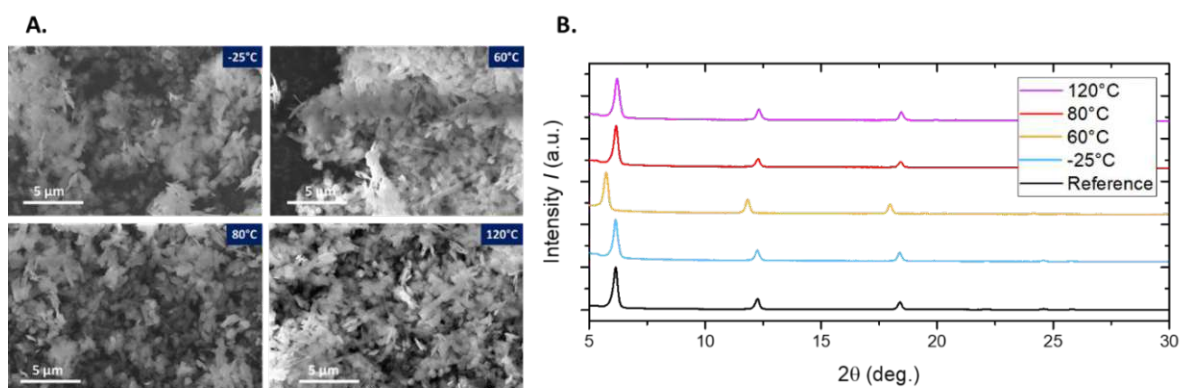


Figure 21. Stability test results of mithrene at various temperatures. **A.** SEM images of mithrene after one week being exposed to -25 °C (upper left corner), 60 °C (upper right corner), 80 °C (down left corner), and 120 °C (down right corner). **B.** XRD pattern of a mithrene reference (black line) and mithrene stored at -25 °C (blue line), 60 °C (orange line), 80 °C (red line) and 120 °C (purple line).

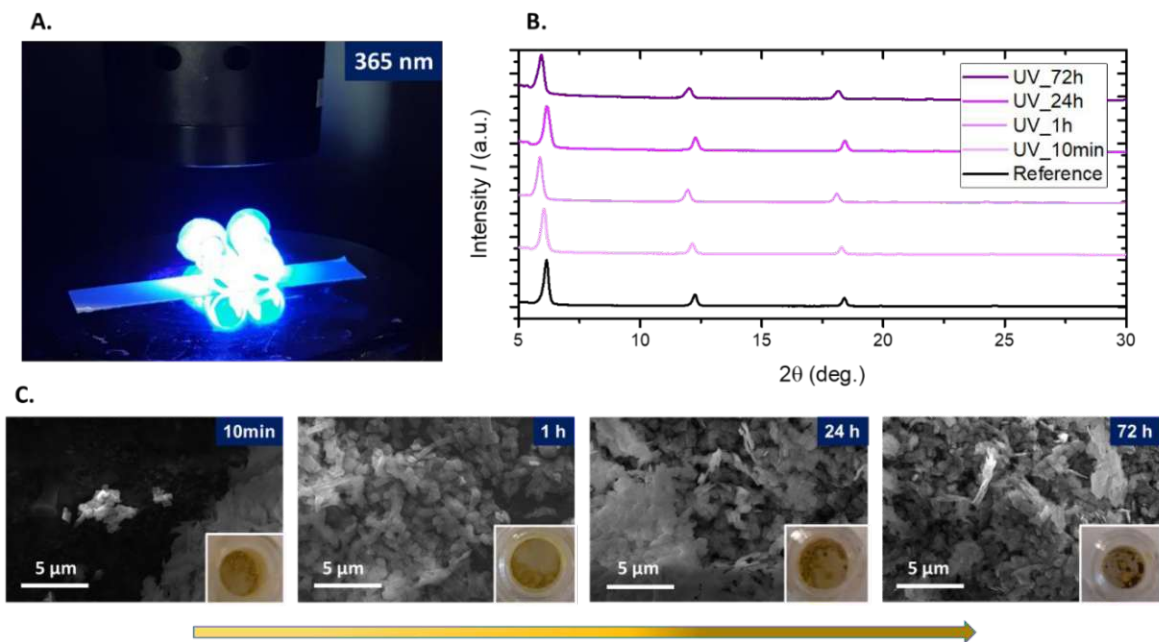


Figure 22. Results of light illumination (365 nm) stability testing. **A.** image of the testing setup. **B.** XRD patterns of a mithrene reference (black line) and mithrene samples being exposed for 10 min (weak purple line), 1h (bright purple line), 24h (purple line) and 72 (dark purple line). **C.** SEM images and pictures (lower right corner) of mithrene being exposed 10 min, 1h, 24h and 72h (from left to right) to 365 nm illumination.

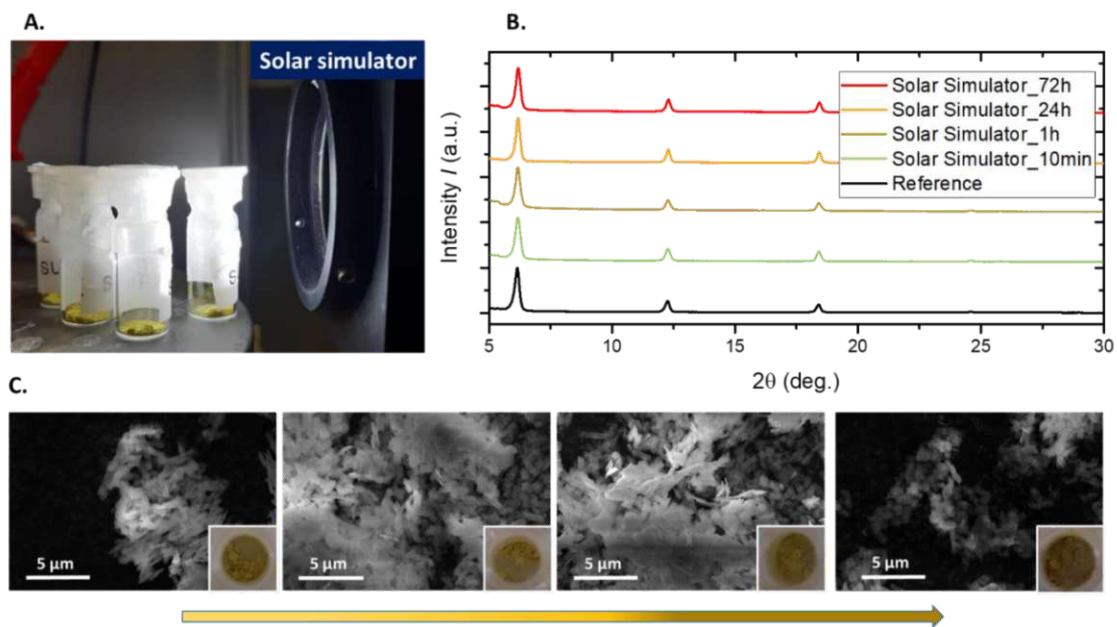


Figure 23. Results of light illumination (VIS light, solar simulator) stability testing. **A.** image of the testing setup. **B.** XRD patterns of a mithrene reference (black line) and mithrene samples being exposed for 10 min (green line), 1h (brown line), 24h (orange line) and 72 (red line). **C.** SEM images and pictures (lower right corner) of mithrene being exposed 10 min, 1h, 24h and 72h (from left to right) to solar simulator illumination.

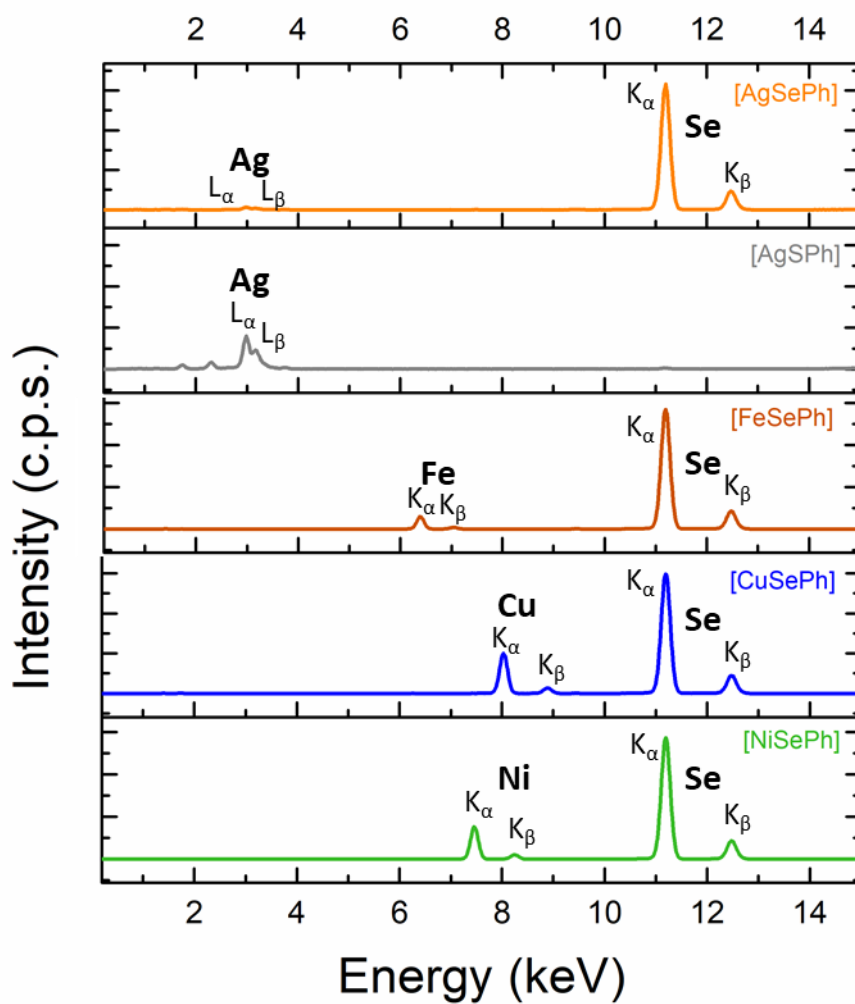
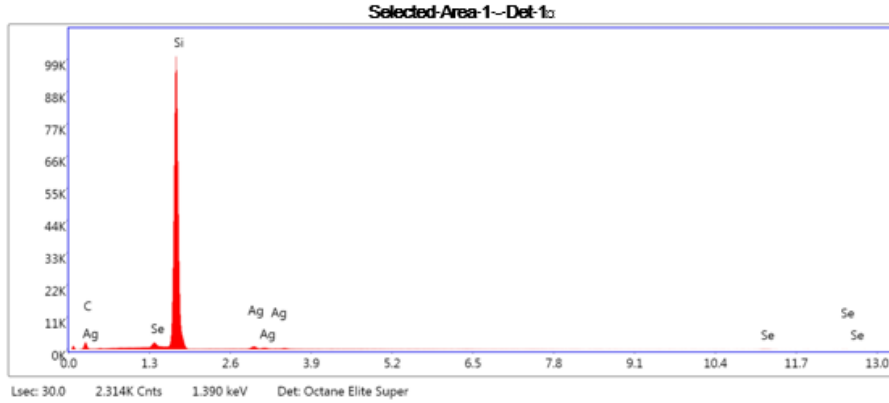


Figure 24. TXRF spectra of synthesized MOCHAs. Mithrene (orange line), thiorene (grey line), thiorene with thiophenol as precursor (light grey line), $[\text{FeSePh}]_\infty$ (brown line), $[\text{FeSPh}]_\infty$ (red line), $[\text{CuSePh}]_\infty$ (blue line) and $[\text{NiSePh}]_\infty$ (green line).

Selected Area 1

kV: 20 Mag: 39992 Takeoff: 31.7 Live-Time(s): 30 Amp-Time(μs): 3.84 Resolution:(eV) 125.2



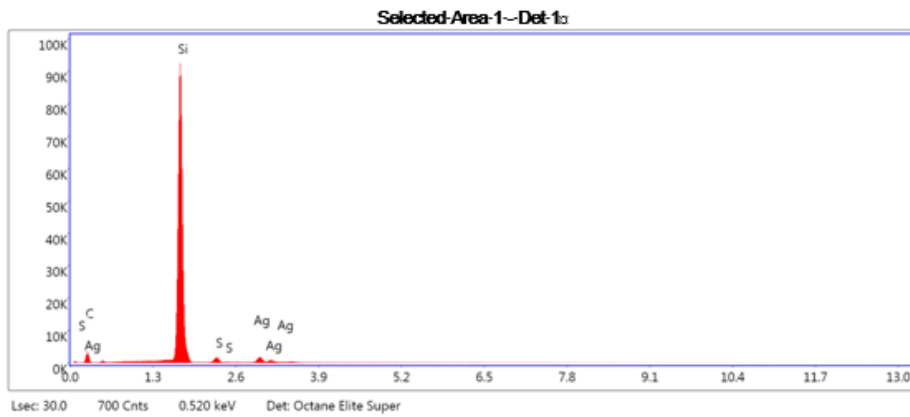
eZAF-Smart-Quant-Results

Element	Weight-%	Atomic-%	Net-Int.	Error-%	Kratio	Z	A	F
C-K	62.3	92.4	299.1	10.0	0.0173	1.1235	0.2930	1.0000
Ag-L	15.3	2.5	202.0	5.6	0.0104	0.7440	1.0791	1.0006
Se-K	22.4	5.0	45.8	17.3	0.0147	0.7261	1.0061	1.0651

Figure 25. EDX spectra and atomic- and weight% ratio results for mitrene.

Selected Area 1

kV: 20 Mag: 19996 Takeoff: 31.6 Live-Time(s): 30 Amp-Time(μs): 3.84 Resolution:(eV) 125.2



eZAF-Smart-Quant-Results

Element	Weight-%	Atomic-%	Net-Int.	Error-%	Kratio	Z	A	F
C-K	63.4	91.2	463.2	8.1	0.0328	1.1056	0.4057	1.0000
S-K	7.9	4.2	290.4	4.4	0.0081	0.9536	0.9098	1.0260
Ag-L	28.7	4.6	432.8	4.8	0.0271	0.7314	1.1191	0.9897

Figure 26. EDX spectra and atomic- and weight% ratio results for thiorene.

13.6 List of all tested microwave synthesis conditions

Table 7. All performed electrolyses with their used electrodes, potentials, durations, atmospheres, illumination, FE's and Rates.

No°	Electrode	Potential E (V vs. RHE)	Time (h)	Atmosphere	Dark / Light	FE CO (%)	FE H ₂ (%)	Rate CO ($\mu\text{mol h}^{-1}$)	Rate H ₂ ($\mu\text{mol h}^{-1}$)
Electrode001	[AgSePh] _∞ / FTO	-1.0	0.5	CO ₂	darkness	-	-	-	-
Electrode002	[AgSPh] _∞ / FTO	-1.0	0.5	CO ₂	darkness	9.5	24.5	-	-
Electrode003	[CuSePh] _∞ / Cu	-1.0	0.5	CO ₂	darkness	6.8	44.3	-	-
Electrode004	[CuSPh] _∞ / Cu	-1.0	0.5	CO ₂	darkness	0.5	54.8	-	-
Electrode005	[CuSePh] _∞ / Cu	-0.8	0.5	CO ₂	darkness	1.8	56.0	-	-
Electrode006	[CuSPh] _∞ / Cu	-0.8	0.5	CO ₂	darkness	0.4	68.7	-	-
Electrode007	[CuSePh] _∞ / Cu	-0.6	0.5	CO ₂	darkness	1.6	67.6	-	-
Electrode008	Cu	-1.0	0.5	CO ₂	darkness	1.5	60.4	-	-
Electrode009	Cu	-0.8	0.5	CO ₂	darkness	0.9	67.7	-	-
Electrode010	Cu	-0.6	0.5	CO ₂	darkness	0.7	68.2	-	-
Electrode011	[CuSePh] _∞ / Cu	-1.0	0.5	CO ₂	darkness	2.1	69.2	-	-
Electrode012	[AgSePh] _∞ / Ag _(displaced) / Cu	-1.0	0.5	CO ₂	darkness	23.9	49.9	-	-
Electrode013	[AgSePh] _∞ / FTO	-1.0	0.5	CO ₂	darkness	12.0	35.9	-	-
Electrode014	[CuSPh] _∞ / Cu	-0.6	0.5	CO ₂	darkness	0.5	88.0	-	-
Electrode015	[CuTePh] _∞ / Cu	-1.0	0.5	CO ₂	darkness	1.6	39.7	-	-
Electrode016	[CuSPh] _∞ / Cu	-0.8	0.5	CO ₂	darkness	0.4	77.2	-	-
Electrode017	FTO	-1.0	0.5	CO ₂	darkness	10.5	44.5	-	-
Electrode018	[AgSePh] _∞ / FTO	-1.0	0.5	CO ₂	darkness	11.4	35.0	-	-
Electrode019	[AgSePh] _∞ / Ag _(displaced) / Cu	-0.8	0.5	CO ₂	darkness	7.6	69.9	-	-
Electrode020	Ag _(displaced) / Cu	-1.0	0.5	CO ₂	darkness	23.1	49.1	-	-
Electrode021	[AgTePh] _∞ / Ag / Cu	-0.6	0.5	CO ₂	darkness	1.8	81.2	-	-
Electrode022	[AgSPh] _∞ / Ag / Cu	-0.6	0.5	CO ₂	darkness	4.3	87.5	-	-
Electrode023	FTO	-0.8	0.5	CO ₂	darkness	12.0	31.7	-	-
Electrode024	FTO	-0.6	0.5	CO ₂	darkness	12.5	53.5	-	-
Electrode025	[AgSePh] _∞ / FTO	-0.8	0.5	CO ₂	darkness	12.2	27.3	-	-

No°	Electrode	Potential E (V vs. RHE)	Time (h)	Atmosphere	Dark / Light	FE CO (%)	FE H ₂ (%)	Rate CO ($\mu\text{mol h}^{-1}$)	Rate H ₂ ($\mu\text{mol h}^{-1}$)
Electrode026	[AgSePh] _∞ / FTO	-0.6	0.5	CO ₂	darkness	14.5	54.2	-	-
Electrode027	[AgSPh] _∞ / FTO	-0.8	0.5	CO ₂	darkness	12.9	30.2	-	-
Electrode028	[AgSPh] _∞ / FTO	-0.6	0.5	CO ₂	darkness	12.2	61.5	-	-
Electrode029	Ag / Cu	-0.6	0.5	CO ₂	darkness	14.8	67.5	-	-
Electrode030	Ag / Cu	-0.8	0.5	CO ₂	darkness	21.3	54.3	-	-
Electrode031	[CuTePh] _∞ / Cu	-0.8	0.5	CO ₂	darkness	1.6	70.4	-	-
Electrode032	Ag wire	-1.0	0.5	CO ₂	darkness	5.2	71.0	-	-
Electrode033	Ag wire (HCl activated)	-1.0	0.5	CO ₂	darkness	2.9	26.4	-	-
Electrode034	Ag wire	-0.8	0.5	CO ₂	darkness	3.2	53.6	-	-
Electrode035	Ag wire (KCN activated)	-1.0	0.5	CO ₂	darkness	15.4	5.4	-	-
Electrode036	[CuTePh] _∞ / Cu	-0.6	0.5	CO ₂	darkness	1.2	116.5	-	-
Electrode037	[AgSePh] _∞ / Ag / Cu	-0.6	0.5	CO ₂	darkness	0.4	9.0	-	-
Electrode038	Ag wire	-1.0	0.5	CO ₂	darkness	14.2	97.1	-	-
Electrode039	[AgTePh] _∞ / Ag / Cu	-0.8	0.5	CO ₂	darkness	11.2	94.9	-	-
Electrode040	Cu	-1.0	0.5	CO ₂	darkness	0.7	103.3	-	-
Electrode041	Ag foam	-1.0	0.5	CO ₂	darkness	55.3	56.8	-	-
Electrode042	[AgTePh] _∞ / Ag wire	-0.8	0.5	CO ₂	darkness	0.4	94.9	-	-
Electrode043	Ag foam	-1.0	0.5	CO ₂	darkness	60.0	48.8	-	-
Electrode044	Ag foam	-0.8	0.5	CO ₂	darkness	72.9	34.6	-	-
Electrode045	Ag foam	-0.8	0.5	CO ₂	darkness	73.6	31.7	-	-
Electrode046	Ag foam	-0.6	0.5	CO ₂	darkness	22.1	59.7	-	-
Electrode047	Ag foam	-0.9	0.5	CO ₂	darkness	75.9	30.3	-	-
Electrode048	Ag foam	-0.9	0.5	CO ₂	darkness	59.8	31.7	-	-
Electrode049	Ag foam	-0.6	0.5	CO ₂	darkness	32.2	62.0	-	-
Electrode050	Ag foam	-1.0	0.5	CO ₂	darkness	59.6	36.4	-	-
Electrode051	Ag foam	-0.9	0.5	CO ₂	darkness	57.7	37.1	-	-
Electrode052	Ag foam	-0.8	0.5	CO ₂	darkness	65.6	36.0	-	-

No°	Electrode	Potential E (V vs. RHE)	Time (h)	Atmosphere	Dark / Light	FE CO (%)	FE H ₂ (%)	Rate CO ($\mu\text{mol h}^{-1}$)	Rate H ₂ ($\mu\text{mol h}^{-1}$)
Electrode053	Ag foam	-0.6	0.5	CO ₂	darkness	48.2	53.8	-	-
Electrode055	Ag foam (@80°C,+water)	-0.8	0.5	CO ₂	darkness	3.7	91.2	-	-
Electrode058	Ag foam (@80°C,+water)	-0.8	0.5	CO ₂	darkness	3.4	118.1	-	-
Electrode059	Ag foam (@80°C)	-0.8	0.5	CO ₂	darkness	15.3	88.3	-	-
Electrode060	Ag foam	-0.4	14	CO ₂	darkness	8.7	76.7	-	-
Electrode061	Ag foam	-0.4	14	CO ₂	365 nm	3.5	90.0	-	-
Electrode062	Ag foam+Coronene	-0.4	14	CO ₂	365 nm	1.2	102.4	-	-
Electrode063	Ag foam+Quinacridone	-0.4	14	CO ₂	456 nm	0.1	64.7	-	-
Electrode064	Ag foam (@40°C oven, 24h, DPDS)	-0.4	14	CO ₂	456 nm	0.1	79.6	-	-
Electrode065	Ag foam	-0.4	14	CO ₂	456 nm	1.9	87.5	-	-
Electrode066	Ag foam (toluene @40°C, 24h)	-0.4	14	CO ₂	456 nm	2.1	89.8	-	-
Electrode067	Ag foam (toluene @40°C, 24h)	-0.8	0.5	CO ₂	darkness	21.5	86.8	-	-
Electrode068	Ag foam	-0.4	14	CO ₂	456 nm	-	-	-	-
Electrode069	[AgSPh] _∞ /Ag foam	-0.4	14	CO ₂	456 nm	0	70.5	-	-
Electrode070	[AgSPh] _∞ /Ag foam	-0.4	14	CO ₂	456 nm	0.4	100.0	-	-
Electrode071	Ag foam	-0.4	14	CO ₂	456 nm	3.0	74.8	-	-
Electrode072	[AgSPh] _∞ /Ag foam	-0.4	14	CO ₂	456 nm	0	0	-	-
Electrode073	GC	-0.4	14	CO ₂	darkness	-	-	-	-
Electrode074	[AgSPh] _∞ / GC	-0.4	14	CO ₂	456 nm	1.5	97.1	-	-
Electrode075	[AgSePh] _∞ / GC	-0.4	14	CO ₂	456 nm	0	0	-	-
Electrode076	[AgTePh] _∞ / GC	-0.4	14	CO ₂	456 nm	0	0	-	-
Electrode077	[AgSePh] _∞ / GC	-1.0	0.5	CO ₂	darkness	6.7	100.8	-	-
Electrode078	[AgSPh] _∞ / GC	-1.0	0.5	CO ₂	darkness	29.3	77.3	-	-
Electrode079	GC	-1.0	0.5	CO ₂	darkness	0	153.1	-	-

No°	Electrode	Potential E (V vs. RHE)	Time (h)	Atmosphere	Dark / Light	FE CO (%)	FE H ₂ (%)	Rate CO ($\mu\text{mol h}^{-1}$)	Rate H ₂ ($\mu\text{mol h}^{-1}$)
Electrode080	GC	-1.0	0.5	CO ₂	darkness	0	138.8	-	-
Electrode081	[AgSePh] _∞ / GC	-1.0	0.5	CO ₂	darkness	23.5	101.1	-	-
Electrode082	[AgSePh] _∞ / GC	-1.0	0.5	CO ₂	darkness			-	-
Electrode083	[AgSePh] _∞ / GC	-1.0	0.5	CO ₂	darkness			-	-
Electrode084	[AgSePh] _∞ / GC	-1.0	0.5	CO ₂	darkness			-	-
Electrode085	[AgSePh] _∞ / Ag-NP / GC	-1.0	0.5	CO ₂	darkness	42.1	79.9	-	-
Electrode086	[AgSePh] _∞ / Ag-NP / GC	-1.0	0.5	CO ₂	456 nm	51.9	156.8	-	-
Electrode087	[AgSePh] _∞ / Ag-NP / FTO	-1.0	0.5	CO ₂	darkness	9.9	55.9	-	-
Electrode088	[AgSePh] _∞ / Ag-NP / FTO	-1.0	0.5	CO ₂	456 nm	27.2	130.1	-	-
Electrode089	CP	-1.0	0.5	CO ₂	darkness	0	105.9	-	-
Electrode090	CP	-1.0	0.5	CO ₂	456 nm	0.3	157.6	-	-
Electrode091	[AgSePh] _∞ / CP	-1.0	0.5	CO ₂	darkness	0	67.3	-	-
Electrode092	[AgSePh] _∞ / CP	-1.0	0.5	CO ₂	456 nm	3.8	90.9	-	-
Electrode093	[AgSePh] _∞ / Ag-NP / CP	-1.0	0.5	CO ₂	darkness	23.7	73.9	-	-
Electrode094	[AgSePh] _∞ / Ag-NP / CP	-1.0	0.5	CO ₂	456 nm	30.5	112.8	-	-
Electrode095	[AgSePh] _∞ / CP	-1.0	0.5	CO ₂	darkness	40.2	61.8	-	-
Electrode096	[AgSePh] _∞ / CP	-1.0	0.5	CO ₂	456 nm	7.9	0	-	-
Electrode097	[AgSePh] _∞ / Ag-NP / CP	-1.0	0.5	CO ₂	darkness	35.0	0	-	-
Electrode098	[AgSePh] _∞ / Ag-NP / CP	-1.0	0.5	CO ₂	456 nm	-	-	-	-
Electrode099	CP	-1.0	0.5	CO ₂	456 nm	0.1	104.1	-	-
Electrode100	[AgSePh] _∞ / CP	-1.0	0.5	CO ₂	456 nm	3.1	86.7	-	-
Electrode101	[AgSePh] _∞ / CP	-1.0	0.5	CO ₂	456 nm	-	144.5	-	-
Electrode102	[AgSePh] _∞ / CP	-1.0	0.5	CO ₂	456 nm	-	-	-	-
Electrode103	[AgSePh] _∞ / CP	-1.0	0.5	CO ₂	darkness	-	-	-	-
Electrode104	[AgSePh] _∞ / CP	-1.0	0.5	CO ₂	darkness	-	-	-	-
Electrode105	[AgSePh] _∞ / Ag-NP / CP	-1.0	0.5	CO ₂	456 nm	34.7	60.2	52.6	91.4
Electrode106	[AgSePh] _∞ / Ag-NP / CP	-0.8	0.5	CO ₂	456 nm	9.3	84.1	7.4	67.1

No°	Electrode	Potential E (V vs. RHE)	Time (h)	Atmosphere	Dark / Light	FE CO (%)	FE H ₂ (%)	Rate CO ($\mu\text{mol h}^{-1}$)	Rate H ₂ ($\mu\text{mol h}^{-1}$)
Electrode107	[AgSePh] _∞ / Ag-NP / CP	-0.4	14	CO ₂	darkness	-	-	0.04	0.8
Electrode108	[AgSePh] _∞ / Ag-NP / CP	-0.6	0.5	CO ₂	456 nm	0.5	84.7	0.2	38.7
Electrode109	CP	-0.8	0.5	CO ₂	456 nm	0.2	106.5	0.3	100.9
Electrode110	CP	-0.6	0.5	CO ₂	456 nm	0	36.3	0	0.5
Electrode111	[AgSePh] _∞ / Ag-NP / CP	-1.0	0.5	CO ₂	darkness	51.0	43.9	65.0	55.9
Electrode112	[AgSePh] _∞ / Ag-NP / CP	-0.8	0.5	CO ₂	darkness	13.7	74.2	7.7	41.4
Electrode113	[AgSePh] _∞ / Ag-NP / CP	-0.6	0.5	CO ₂	darkness	0.5	92.6	0.2	33.4
Electrode114	[AgSePh] _∞ / Ag-NP / CP	-0.4	14	CO ₂	456 nm	0.8	49.7	0.1	3.4
Electrode115	[AgSePh] _∞ / CP	-1.0	0.5	CO ₂	456 nm	34.8	61.2	41.1	72.3
Electrode116	[AgSePh] _∞ / CP	-0.8	0.5	CO ₂	456 nm	6.3	91.7	2.3	33.4
Electrode117	[AgSePh] _∞ / CP	-0.6	0.5	CO ₂	456 nm	0.7	83.3	0.2	20.3
Electrode118	[AgSePh] _∞ / CP	-1.0	0.5	CO ₂	darkness	36.7	70.6	40.2	77.3
Electrode119	[AgSePh] _∞ / CP	-0.8	0.5	CO ₂	darkness	6.8	94.7	2.0	28.0
Electrode120	[AgSePh] _∞ / CP	-0.4	14	CO ₂	darkness	0.1	8.3	0.01	0.5
Electrode121	[AgSePh] _∞ / CP	-0.6	0.5	CO ₂	darkness	0	44.5	0	1.8
Electrode122	CP	-0.8	0.5	CO ₂	darkness	0.7	102.3	0.1	20.8
Electrode123	CP	-0.6	0.5	CO ₂	darkness	0	3.3	0	0.1
Electrode124	CP	-1.0	0.5	CO ₂	456 nm	0.1	95.2	0.1	181.9
Electrode125	CP	-1.0	0.5	CO ₂	darkness	0	98.9	0	170.5
Electrode126	CP	-1.0	0.5	CO ₂	darkness	0.1	102.8	0.1	127.4
Electrode127	CP	-0.8	0.5	CO ₂	darkness	0	85.6	0	22.3
Electrode128	CP	-0.6	0.5	CO ₂	darkness	0	49.6	0	3.5
Electrode129	CP	-1.0	0.5	CO ₂	456 nm	0.05	92.2	0.2	283.4
Electrode130	CP	-0.8	0.5	CO ₂	456 nm	0	109.4	0	79.5
Electrode131	CP	-0.6	0.5	CO ₂	456 nm	0	58.4	0	1.2
Electrode132	[AgSePh] _∞ / CP	-1.0	0.5	CO ₂	darkness	29.7	74.4	31.2	78.1
Electrode133	[AgSePh] _∞ / CP	-0.8	0.5	CO ₂	darkness	4.4	74.6	1.4	23.7

No°	Electrode	Potential E (V vs. RHE)	Time (h)	Atmosphere	Dark / Light	FE CO (%)	FE H ₂ (%)	Rate CO ($\mu\text{mol h}^{-1}$)	Rate H ₂ ($\mu\text{mol h}^{-1}$)
Electrode134	[AgSePh] _∞ / CP	-0.6	0.5	CO ₂	darkness	0	30.3	0	6.5
Electrode135	[AgSePh] _∞ / CP	-0.4	14	CO ₂	456 nm	0.4	31.9	0.02	1.7
Electrode136	[AgSePh] _∞ / CP	-1.0	0.5	CO ₂	456 nm	3.7	89.6	1.9	48.0
Electrode137	[AgSePh] _∞ / CP	-0.8	0.5	CO ₂	456 nm	3.7	91.3	1.9	46.4
Electrode138	[AgSePh] _∞ / CP	-0.6	0.5	CO ₂	456 nm	0.4	86.8	0.2	28.5
Electrode139	[AgSePh] _∞ / Ag-NP / CP	-1.0	0.5	CO ₂	darkness	36.4	62.2	50.2	85.8
Electrode140	[AgSePh] _∞ / Ag-NP / CP	-0.8	0.5	CO ₂	darkness	10.3	65.9	4.9	31.5
Electrode141	[AgSePh] _∞ / Ag-NP / CP	-0.6	0.5	CO ₂	darkness	0.5	76.0	0.1	24.2
Electrode142	[AgSePh] _∞ / Ag-NP / CP	-1.0	0.5	CO ₂	456 nm	18.8	65.9	34.6	121.8
Electrode143	[AgSePh] _∞ / Ag-NP / CP	-0.8	0.5	CO ₂	456 nm	7.6	86.3	4.6	52.3
Electrode144	[AgSePh] _∞ / CP	-1.0	0.5	CO ₂	456 nm	24.4	70.1	38.8	111.3
Electrode145	[FeSePh] _∞ / CP	-1.0	0.5	CO ₂	darkness	0	94.6	0	154.8
Electrode146	[FeSePh] _∞ / CP	-0.8	0.5	CO ₂	darkness	0.4	60.3	0.1	23.8
Electrode147	[FeSePh] _∞ / CP	-0.6	0.5	CO ₂	darkness	2.3	2726.6	0.2	0
Electrode148	[FeSePh] _∞ / CP	-1.0	0.5	CO ₂	456 nm	0	1.6	0	0
Electrode149	CP	-1.0	14	CO ₂	darkness	0	0	0	0
Electrode150	[FeSePh] _∞ / CP	-0.8	0.5	CO ₂	456 nm	0	77.6	0	30.5
Electrode151	[AgSePh] _∞ / Ag-NP / CP	-0.6	0.5	CO ₂	456 nm	0.4	93.4	0.2	48.2
Electrode152	Ag-NP / CP	-1.0	0.5	CO ₂	456 nm	37.3	60.2	79.6	128.5
Electrode153	Ag-NP / CP	-0.8	0.5	CO ₂	456 nm	12.6	81.04	7.5	48.6
Electrode154	Ag-NP / CP	-0.6	0.5	CO ₂	456 nm	10.6	72.6	2.1	14.2
Electrode155	Ag-NP / CP	-1.0	0.5	CO ₂	darkness	76.3	22.0	158.9	45.9
Electrode156	Ag-NP / CP	-0.8	0.5	CO ₂	darkness	4.2	0.4	7.6	0.7
Electrode157	Ag-NP / CP	-0.6	0.5	CO ₂	darkness	2.8	77.8	0.3	7.3
Electrode158	Ag-NP / CP	-1.0	0.5	CO ₂	456 nm	2.3	66.7	0.3	7.6
Electrode159	Ag-NP / CP	-0.8	0.5	CO ₂	456 nm	3.9	97.3	2.3	57.4
Electrode160	Ag-NP / CP	-0.6	0.5	CO ₂	456 nm	1.1	98.6	0.3	24.8

No°	Electrode	Potential E (V vs. RHE)	Time (h)	Atmosphere	Dark / Light	FE CO (%)	FE H ₂ (%)	Rate CO (μmol h ⁻¹)	Rate H ₂ (μmol h ⁻¹)
Electrode161	Ag-NP / CP	-1.0	0.5	CO ₂	darkness	1.7	104.3	2.7	161.6
Electrode162	Ag-NP / CP	-0.8	0.5	CO ₂	darkness	3.5	1096	1.6	49.8
Electrode163	Ag-NP / CP	-0.6	0.5	CO ₂	darkness	3.2	72.8	0.5	11.0
Electrode164	CP	-0.4	0.5	CO ₂	456 nm	0.3	1.0	0.02	0.1
Electrode165	[AgSePh] _∞ / Ag-NP / CP	-0.4	14	CO ₂	darkness	0.03	6.5	0.01	1.5
Electrode166	[AgSPh] _∞ / CP	-1.0	14	CO ₂	darkness	59.1	30.4	90.4	46.5
Electrode167	[AgSPh] _∞ / CP	-1.0	0.5	CO ₂	darkness	40.7	44.7	61.9	68.0
Electrode168	[AgSPh] _∞ / CP	-0.8	0.5	CO ₂	darkness	34.6	61.1	22.7	40.1
Electrode169	[AgSPh] _∞ / CP	-0.8	0.5	CO ₂	darkness	35.4	68.1	20.5	39.5
Electrode170	[AgSPh] _∞ / CP	-0.6	0.5	CO ₂	darkness	1.9	73.7	0.4	15.4
Electrode171	[AgSPh] _∞ / CP	-0.6	0.5	CO ₂	darkness	1.9	71.8	0.4	13.2
Electrode172	[AgSPh] _∞ / CP	-1.0	0.5	CO ₂	456 nm	76	55	105	68
Electrode173	[AgSPh] _∞ / CP	-1.0	0.5	CO ₂	456 nm	69.4	25.1	120.6	43.5
Electrode174	[AgSPh] _∞ / CP	-0.8	0.5	CO ₂	456 nm	26.7	65.4	23.6	57.9
Electrode175	[AgSPh] _∞ / CP	-1.0	0.5	CO ₂	darkness	64.9	28.8	90.0	39.9
Electrode176	[AgSePh] _∞ / CP	-1.0	0.5	CO ₂	darkness	52.7	-	78.3	-
Electrode177	[AgSPh] _∞ / CP	-0.8	0.5	CO ₂	456 nm	42.6	62.1	40.2	58.7
Electrode178	[AgSPh] _∞ / CP	-0.6	0.5	CO ₂	456 nm	4.4	81.0	1.3	23.5
Electrode179	[AgSPh] _∞ / CP	-0.6	0.5	CO ₂	456 nm	10.1	82.4	2.44	20.0
Electrode180	[AgSePh] _∞ / CP	-1.0	0.5	CO ₂	darkness	78.4	18.7	85.4	20.3
Electrode181	[AgSePh] _∞ / CP	-1.0	0.5	CO ₂	darkness	78.8	17.9	87.4	19.8
Electrode182	[AgSePh] _∞ / CP	-1.0	0.5	CO ₂	darkness	-	-	45.2	22.7
Electrode183	[AgSePh] _∞ / CP	-1.0	0.5	CO ₂	darkness	65.6	17.6	70.3	18.8
Electrode184	[AgSePh] _∞ / CP	-1.0	0.5	CO ₂	darkness	67.4	22.1	66.5	21.8
Electrode185	[AgSePh] _∞ / Ag-NP / CP	-1.0	0.5	CO ₂	darkness	35.1	45.5	61.4	79.8
Electrode186	[AgSePh] _∞ / Ag-NP / CP	-1.0	0.5	CO ₂	darkness	56.6	46.6	69.1	56.9
Electrode187	[AgSePh] _∞ / Ag-NP / CP	-0.8	0.5	CO ₂	darkness	18.2	59.3	11.6	37.7

No°	Electrode	Potential E (V vs. RHE)	Time (h)	Atmosphere	Dark / Light	FE CO (%)	FE H ₂ (%)	Rate CO (μmol h ⁻¹)	Rate H ₂ (μmol h ⁻¹)
Electrode188	[AgSePh] _∞ / Ag-NP / CP	-0.8	0.5	CO ₂	darkness	17.6	67.0	8.4	31.8
Electrode189	[AgSePh] _∞ / Ag-NP / CP	-0.6	0.5	CO ₂	darkness	0	60.9	0	19.7
Electrode190	[AgSePh] _∞ / Ag-NP / CP	-0.6	0.5	CO ₂	darkness	0	55.7	0	13.3
Electrode191	[AgSePh] _∞ / Ag-NP / CP	-1.0	0.5	CO ₂	456 nm	81.6	53.4	143.1	93.5
Electrode192	[AgSePh] _∞ / Ag-NP / CP	-1.0	0.5	CO ₂	456 nm	62.8	45.0	122.8	88.1
Electrode193	[AgSePh] _∞ / Ag-NP / CP	-0.8	0.5	CO ₂	456 nm	27.7	70.7	15.2	38.9
Electrode194	[AgSePh] _∞ / Ag-NP / CP	-0.8	0.5	CO ₂	456 nm	25.4	82.4	17.9	58.4
Electrode195	[AgSePh] _∞ / Ag-NP / CP	-0.6	0.5	CO ₂	456 nm	0	86.6	0	39.2
Electrode196	[AgSePh] _∞ / Ag-NP / CP	-0.6	0.5	CO ₂	456 nm	0	83.9	0	65.9
Electrode197	[AgSPh] _∞ / Ag-NP / CP	-1.0	0.5	CO ₂	darkness	63.6	37.0	99.2	57.6
Electrode198	[AgSPh] _∞ / Ag-NP / CP	-1.0	0.5	CO ₂	darkness	237.5	0	331.7	0
Electrode199	[AgSPh] _∞ / Ag-NP / CP	-0.8	0.5	CO ₂	darkness	71.9	77.8	33.7	36.5
Electrode200	[AgSPh] _∞ / Ag-NP / CP	-0.8	0.5	CO ₂	darkness	36.8	53.9	22.4	32.8
Electrode201	[AgSPh] _∞ / Ag-NP / CP	-0.6	0.5	CO ₂	darkness	31.6	1526	4.0	19.2
Electrode202	[AgSPh] _∞ / Ag-NP / CP	-0.6	0.5	CO ₂	darkness	0	90.5	0	25.1
Electrode203	[AgSPh] _∞ / Ag-NP / CP	-1.0	0.5	CO ₂	456 nm	58.3	55.6	106.3	101.5
Electrode204	[AgSPh] _∞ / Ag-NP / CP	-1.0	0.5	CO ₂	456 nm	1047	126.5	132.7	1602
Electrode205	[AgSPh] _∞ / Ag-NP / CP	-0.8	0.5	CO ₂	456 nm	51.7	75.3	54.6	79.6
Electrode206	[AgSPh] _∞ / Ag-NP / CP	-0.8	0.5	CO ₂	456 nm	25.7	58.5	41.0	93.3
Electrode207	[AgSPh] _∞ / Ag-NP / CP	-0.6	0.5	CO ₂	456 nm	16.4	79.7	5.2	25.5
Electrode208	[AgSPh] _∞ / Ag-NP / CP	-0.6	0.5	CO ₂	456 nm	15.9	0	2.5	0
Electrode209	[AgSePh] _∞ / CP	-1.0	0.5	N ₂	456 nm	0	0	0	0